Effects of Surface and Interface in Confined Semiconductors: Studies of Structural, Electronic and Optical Properties

Ph.D. Thesis

By

ARPAN GHOSH

DISCIPLINE OF PHYSICS

INDIAN INSTITUTE OF TECHNOLOGY INDORE

December 2024

Effects of Surface and Interface in Confined Semiconductors: Studies of Structural, Electronic and Optical Properties

A THESIS

Submitted in partial fulfillment of the requirements for the award of the degree

of

DOCTOR OF PHILOSOPHY

by

ARPAN GHOSH

DEPARTMENT OF PHYSICS

INDIAN INSTITUTE OF TECHNOLOGY INDORE

December, 2024

INDIAN INSTITUTE OF TECHNOLOGY INDORE

CANDIDATE'S DECLARATION

I hereby certify that the work which is being presented in the thesis entitled **Effects of surface and interfaces in confined semiconductor and their composites: study of structural, electronic and optical properties** in the partial fulfillment of the requirements for the award of the degree of **DOCTOR OF PHILOSOPHY** and submitted in the **DEPARTMENT OF PHYSICS, Indian Institute of Technology Indore**, is an authentic record of my own work carried out during the time period from July 2019 to under the supervision of Dr. Sudeshna Chattopadhyay, Professor, IIT Indore.

The matter presented in this thesis has not been submitted by me for the award of any other degree of this or any other institute. Arpan Ghosh 27/06/2025

Signature of the student with date
(ARPAN GHOSH)

This is to certify that the above statement made by the candidate is correct to the best of my/our knowledge.

June 27, 2025

Signature of Thesis Supervisor with date

(Prof. Sudeshna Chattopadhyay)

ARPAN GHOSH has successfully given his/her Ph.D. Oral Examination held on **Date of PhD Oral Examination**

June 27, 2025

Signature of Thesis Supervisor with date

(Prof. Sudeshna Chattopadhyay)

Dedicated to my family & my country, India

Acknowledgements

First, I would like to express my sincere gratitude to my respected PhD supervisor Professor Sudeshna Chattopadhyay for her exemplary guidance, monitoring and constant encouragement throughout my PhD journey. The blessing, help and guidance given by her from time to time shall carry me long way in the journey of life on which I am about to embark. Hereby I conclude the confidence that she has bestowed upon me by including me in her research group for which I feel very much privileged in working under such an esteemed, eminent and masterly guide without whom compilation of this present form would not be possible. I am very much thankful for her devoted contribution in reviewing my progress, writing, making corrections to improve and finalize the research papers. Particularly I am very thankful to her for creating a profound interest in this field. Overall, it has been a nice learning experience for me throughout my study at IIT Indore.

I would like to express my sincere gratitude to Prof. Suhas Joshi, Director, IIT Indore. His positive energy and enthusiasm towards research always motivated me.

I would like to express my sincere gratitude to my parents and my extended family. My father and mother have always been a source of encouragement and inspiration to me throughout my life. This these would not have been possible without their support and help.

I would like to acknowledge MHRD, Govt. of India for providing me the fellowship of teaching assistant (TA).

I would like to acknowledge IIT Indore for providing me all kinds of support to my PhD thesis work. I want to thank Department of Physics, IIT Indore for providing all resources and facilities for the completion of my PhD thesis. I also want to thank Sophisticated Instrument Centre (SIC), IIT Indore for providing experimental facilities. I also want to thank IISER Pune for providing FESEM facility.

I am extremely grateful to my PSPC members Prof. Srimanta Pakhira, Department of Physics, IIT Indore and Prof. Shanmugam

Dhinakaran, Department of Mechanical Engineering, IIT Indore for their encouragement, helpful advice, insightful comments, questions and valuable suggestions which helped me a lot in improving my research work.

I would like to thank user facility at IIT Delhi for PL measurement. Also, I would like to thank IISER Pune for providing FESEM facility.

I sincerely thank my supervisor, Prof. Sudeshna Chattopadhyay and my lab mates, Vikas Munya, Ravinder Kumar, Banadeep Dutta, Adi Pratap Singh, Prateeksha Rajpoot, Yukta Sharma & Shailendra Singh for helping me in experiments, data analysis and writing PhD thesis. Moreover, I also want to thank M.Sc. Project student, Kumar Naman for helping me in experiments.

I am also thankful to some of best buddies, Subhasanket Dutta, Rahul Chowhan for always staying in my good as well as bad times.

I would like to thank Mr. Nitin Upadhyay for helping me in the technical works at SIC, IIT Indore.

I would also like to thankfully mention that the project was supported by Department of Science and Technology (DST), Government of India-SERB [Project No: CRG/2020/005595].

I would like to acknowledge DST, Government of India for providing us the fund.

I am also thankful to Department of Science and Technology (DST), FIST program [Project No. SR/FST/PSI/225/2016] for providing us Raman facility.

Arpan Ghosh

List of Publications

(A) Peer-reviewed journals (from thesis work)

1. “Self-Healing of Defect-Mediated Disorder in ZnO Thin Films Grown by Atomic Layer Deposition.” Don P. Benny, Vikas Munya, **Arpan Ghosh**, Ravinder Kumar, Dipayan Pal, Herbert Pfnür, Sudeshna Chattopadhyay. *Journal of Electronic Materials* 52, no.12 (2023):8293-8302.

2. "Epitaxial growth of excitonic single crystals and heterostructures: Oxides and nitrides", Prateeksha Rajpoot, **Arpan Ghosh**, Amandeep Kaur, Simran Arora, Mohamed Henini, Subhabrata Dhar, Sudeshna Chattopadhyay. *MRS Bulletin* 49, no. 9 (2024): 885-898.

3. “Correlation of Structure and Electronic properties in Ni-doped ZnO”, (Work is in progress -Manuscript under preparation)

(B) Peer-reviewed journals (other than thesis work)

1. "F4-TCNQ on Epitaxial Bi-Layer Graphene: Concentration-and Orientation-Dependent Charge Transfer at the Interface", Sudeshna Chattopadhyay, Vikas Munya, Ravinder Kumar, Dipayan Pal, Sucheta Bandyopadhyay, **Arpan Ghosh**, Priyanka Yogi, Julian Koch, Herbert Pfnür. *Langmuir* 38, no. 51 (2022): 16067-16072.

Table of Contents

List of Figures

equation (2.18) of chapter 2 in manuscript, where the value of n is 1/2 for allowed direct transition; (b) Plots of the Urbach energy (E_u) (red filled circle) and optical bandgap ($E_{g,e}$) (purple open square) of the ZnO_a as a function of film thickness; The dotted straight line is the eye guided line.

Figure 3.6: Plots of the exciton energy ($E_{g,f}$) (blue open circles) and the optical band gap ($E_{g,e}$) (red filled circles) versus the Urbach energy (E_u). The dotted straight lines are guides to the eye.

Figure 3.7: Room temperature PL spectra of ZnO thin films (ZnO_a) for thicknesses of (i) 9 nm (ii) 19 nm (iii) 38 nm (iv) 52 nm and (v) 69 nm. The spectra are normalized with respect to the UV peak. The PL spectra show near band (NBE) and defect level emissions (DLE). Insets show the corresponding PL spectra in log scale to display the weak DLE components clearly. The contributions from FX and FX-2LO to NBE and the contribution of green (DLE1) and red emissions (DLE2) to DLE were extracted by Gaussian fits of the PL spectra. The combined effects of the four Gaussians are indicated by the pink solid curves. Circles: experimental data.

Figure 3.8: Plot of (a) Urbach energy (filled circles) and I_{FX-2LO}/I_{FX} (open circles) versus thickness. (b) Urbach energy (filled circles) and I_{DLE2}/I_{NBE} (open squares) versus thickness. (c) Urbach energy (filled circles) and I_{DLE1}/I_{NBE} (open stars) versus thickness. Urbach energy was estimated from UV-Vis spectroscopy, whereas I_{FX}, $I_{FX\text{-}2LO}$, I_{NBE}, I_{DLE1} and I_{DLE2} were estimated from photoluminescence (PL) study.

Figure 3.9: Confinement effect in ZnO_a films. Bandgap energy ($E_{g,PL}$) versus $1/d^2$ plot, where d is the film thickness: circles and lines represent experimental data and theoretical fit, respectively.

Figure 4.1: Top-view SEM images of ZnO thin films on fused quartz (ZnO_a/qz) of characteristic film thicknesses: (a) 9 nm, (b) 19 nm, (c) 38 nm, and (d) 69 nm. The average in-plane grain sizes (major and minor axes) for 38 nm and 69 nm thick samples are shown within the dotted circles.

respect to pure ZnO. (b) Peak shift of E_2(high) vibrational mode of 3.6% NZO and 8 % NZO with respect to pure ZnO.

Figure 5.10: Variation of (a) E_2 (low) and (b) E_2 (high) peak position in Ni doped ZnO, with variation of doping concentration (mol %).

Figure 5.11: Representation of variation in d-spacing (%) corresponding to the plane (101) and E_2(high) peak position as a function of Ni-doping percentage.

Figure 5.12: Absorption spectra of RhB after different photodegradation durations upon UV irradiation in presence of: (a) pure ZnO (b) 3.6% Ni doped ZnO (c) 5.1 % Ni doped ZnO.

Figure 5.13: Change in normalized concentration (C/C_0) of RhB dye vs. irradiation time in the presence of ZnO (black square), 3.6% Ni-doped ZnO (red circle), and 5.1% Ni-doped ZnO (blue triangle). Inset shows photodegradation reaction rate constant (k) in min^{-1} with different Ni doping percentage.

List of Tables:

Acronyms

Zinc oxide	ZnO
Atomic layer deposition	ALD
Physical vapor deposition	PVD
Chemical vapor deposition	CVD
Quartz	qz
X-ray reflectivity	XRR
X-ray diffraction	XRD
Photoluminescence	PL
Near band-edge emission	NBE
Deep level emission	DLE
Conduction band	CB
Valence band	VB
Field Emission Scanning Electron Microscopy	FESEM
ZnO thin film grown by ALD	ZnO_a
ALD grown ZnO on fused quartz	ZnO_a/qz

Chapter 1
Introduction

Nanomaterials, defined by their nanoscale dimensions (1–100 nanometres), have undergone remarkable advancements, transforming diverse fields like electronics, healthcare, energy, and environmental science. The significance of nanomaterials lies in their ability to revolutionize existing technologies and address critical challenges. Their properties, distinct from bulk materials due to size effects and high surface-area-to-volume ratios, have been harnessed for innovative solutions [1]. Cutting-edge synthesis techniques such as chemical vapor deposition, sol-gel processes, and green chemistry approaches have enabled precise control over nanomaterial properties.

1.1 Role of confinement effect

The confinement effect emerges prominently when the size of a material is reduced to the nanoscale, causing a restriction in the motion of particles such as electrons, holes, and phonons. This spatial restriction alters the fundamental physical and chemical properties of the material, distinguishing it from its bulk counterpart. A key feature of the confinement effect is the significant influence of quantum mechanics, where the wave-like nature of particles becomes evident [2]. So, change in the fundamental properties of the material due to the change in the size is known as confinement effect. Based on the number to dimensions restricted in a material confinement has following types: 0-D confinement, 1-D confinement, 2-D confinement and 3-D confinement [3].

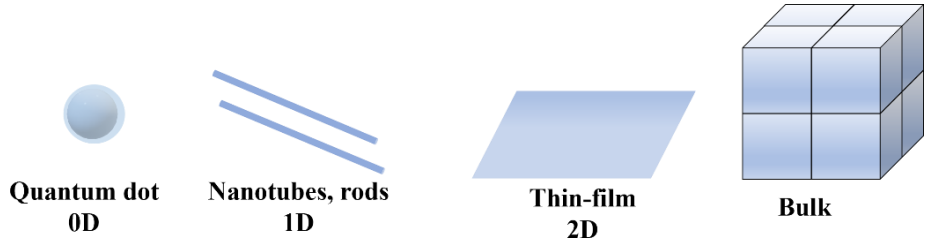

Figure 1.1: Nanomaterials classification based on dimensionality**.**

When the dimensions of a nanostructure approach or fall below the de Broglie wavelength of electrons or the exciton Bohr radius, the energy levels of the material become quantized rather than continuous [4]. This quantization results in unique size-dependent properties, such as a widening of the bandgap in semiconductors and discrete energy levels in quantum dots. When the physical dimensions of a material or system are significantly reduced, two key phenomena emerge: surface/interface effects and quantum confinement effects [5, 6]. These effects induce substantial changes in the material's properties compared to those observed in its bulk form, resulting in notable deviations in measured behaviors.

1.1.1 Quantum confinement effect

The quantum confinement effect is a fundamental phenomenon that arises when the dimensions of a material are reduced to the nanoscale. In this regime, the motion of charge carriers, such as electrons and holes, becomes spatially restricted, leading to quantization of their energy levels. This effect fundamentally alters the electronic, optical, and transport properties of materials, setting them apart from their bulk counterparts. Quantum confinement is particularly prominent in low-dimensional systems, making it a cornerstone of modern nanotechnology and materials science [7]. The size at which a material exhibits quantum confinement varies depending on its specific properties and is governed by the quantum mechanical behavior of electrons and holes within the material. Quantitatively, this characteristic length scale is often described by the excitonic Bohr radius, a_B, which can be expressed as follows [8]:

$$a_B = \frac{\hbar^2 \varepsilon}{e^2}\left(\frac{1}{m_e^*} + \frac{1}{m_h^*}\right) \quad \textbf{(1.1)}$$

Where, $\hbar = h/2\pi$, h is Planck's constant, e is the fundamental electronic charge, ε is the bulk dielectric constant, and m_e^* and m_h^* are the effective masses of the electron and hole, respectively. For a semiconductor material system smaller than the excitonic Bohr radius a_B in at least one of the dimensions, the system can be said to be in the strong confinement regime, and if in comparable or larger dimensions, in the weak confinement regime [8]. For example, from theoretical calculation the value of excitonic Bohr radius for bulk ZnO was reported as ~2.34 nm [9].

1.1.2 Surface/interface effects

While confinement opens new opportunities, its effects are also coupled with surface and interface phenomena, which can introduce localized states and defects that influence overall material performance [10]. The surface and interface effects in confined materials play a crucial role in determining the physical and chemical properties of materials at small scales. When materials are confined to nanoscale dimensions, the behavior of atoms or molecules at the surface or interface becomes significantly different from that in bulk material [11]. An interface is a boundary that separates two distinct regions, each occupied by different substances or by the same substance in different physical states. When the interface occurs between matter and air, or between matter and a vacuum, it is referred to as a surface. At the nanoscale, the surface-to-volume ratio increases dramatically, making surface and interface phenomena dominant factors in determining the behavior of materials/semiconductors [12]. Surface atoms, often undercoordinated compared to their bulk counterparts, as surface atoms are not fully surrounded by other atoms, resulting in higher energy state and exhibit altered bonding configurations, leading to unique surface energy landscapes, strain distributions, increased reactivity, and defect dynamics. These effects are amplified as the material size decreases, making them particularly important in nanomaterials, thin films, and

other confined systems [11]. The interface effect, on the other hand, refers to the interactions between different materials or phases at their boundaries become more prominent, influencing the overall properties of the system [13]. Interfacial phenomena such as band alignment, charge transfer, and strain-induced electronic modifications play a critical role in tailoring the material characteristics for targeted device applications. On the optical front, nanoscale confinement and surface interactions can induce size-dependent shifts in absorption and emission spectra, enhance photoluminescence, and enable novel phenomena such as nonlinear optical behavior and plasmonic coupling [11, 13]. These effects can be tuned by controlling the size, shape, and composition of the confined material, allowing for the tailoring of properties for specific applications.

1.2 Effect of confinement and surface/interface in semiconductor materials

Semiconductors are the cornerstone of modern electronics and have revolutionized technology by enabling the miniaturization and integration of complex devices. These semiconductor materials (such as ZnO, TiO_2, SnO_2, Cu_2O), which have electrical conductivities between those of conductors and insulators, exhibit unique properties that can be tailored through doping and structural manipulation [14]. This versatility makes semiconductors critical for devices such as transistors, diodes, solar cells, and integrated circuits, which form the backbone of communication, computation, and energy systems. They can be divided into two categories according to whether the bandgap transition, [15] a crucial semiconductor property for optoelectronic applications, is direct or indirect. The energy gap is known as the "direct bandgap" if the valence band maximum (VBM) and the conduction band minimum (CBM) are located at the same location in k-space. For conventional semiconductors, this is often at the centre (Γ-point) of the Brillouin zone. An indirect bandgap semiconductor is one in which the k-vectors for the valence band maxima and conduction band minima disagree. Electron-hole pairs will most likely recombine radiatively if a semiconductor has

a direct bandgap and the electric dipole transition from VBM to CBM is permitted [16]. Consequently, high-quality direct bandgap semiconductors are employed to create light emitters with great efficiency. In contrast, photodetectors and the window layer of solar cells employ indirect bandgap semiconductors [15].

One of the governing elements that determines the optical/electronic spectra is the existence of defects in semiconductors. Defect states have the ability to relate to the emission spectra and influence the absorption spectra by absorbing sub-bandgap photons. Defect levels are crucial in a number of optoelectronic applications, including the regulation of luminescence centres in materials with a large bandgap at particular wavelengths [17]. Energy-level defects in the bandgap can serve as recombination sites, preventing light output from a light-emitting diode or carrier collection in a solar cell. Defects, however, may also be to cause for a device's deterioration [18]. In semiconductor applications, it is crucial to regulate intrinsic flaws and the resulting impacts on characteristics. The controllability of the defect density depends on the type of defect and the semiconductor itself [19].

Semiconductors have become indispensable in modern technology, and their properties are dramatically influenced by the effects of quantum confinement and surface/interface characteristics, especially when reduced to nanoscale dimensions. This effect restricts the motion of charge carriers to discrete energy levels, significantly altering the electronic and optical properties of the material [5]. Surface and interface effects, equally vital, dominate the behavior of semiconductors as their surface-to-volume ratio increases at the nanoscale. Unlike bulk materials, where internal atoms largely dictate properties, nanoscale semiconductors have a substantial proportion of their atoms exposed on the surface or at interfaces. These surfaces often possess unsaturated bonds or adsorbed species, leading to phenomena like surface states, defect traps, and band bending. Similarly, interfaces between different materials, such as in heterostructures, result in complex charge transfer, polarization, and strain effects. These interactions are crucial for devices

such as transistors [20], light-emitting diodes [21], and photovoltaic cell [21], where precise control over surface and interface properties determines efficiency and performance.

1.3 Properties and prospects of ZnO: Material of Interest

Zinc oxide (ZnO) is a semiconductor material with large band gap (~3.37 eV) and good chemical stability. There are three crystalline forms of ZnO: wurtzite, zinc blende and rarely rock salt. Nonetheless, the most thermodynamically stable of these is the hexagonal wurtzite phase, it can also be seen as two interpenetrating hexagonal close-packed (HCP) sublattices of separate Zn and O layers displayed along c-direction. Some of ZnO's unique characteristics are [22-24].:

- Direct and wide bandgap: make ZnO a promising material for short-wavelength optoelectronic devices [22].
- Large excitonic binding energy (60meV): makes it suitable for ultraviolet light-emitting diodes (LEDs) and laser diodes [25].
- Biocompatible and inexpensive: ZnO nanoparticles have exposed prospective application in drug delivery and bioimaging due to its biocompatibility.
- Excellent catalytic activity: used in photocatalysis for dye degradation.
- Strong luminescence: Due to a strong luminescence in the green–white region of the spectrum, ZnO is also a suitable material for phosphor applications.

  ZnO is a versatile semiconductor material with remarkable properties, making it a focal point of research in photonics, optoelectronics, and excitonic applications. This unique structure endows ZnO with a direct wide bandgap and a large exciton binding energy of 60 meV, enabling efficient exciton formation and recombination even at room temperature [23, 24].

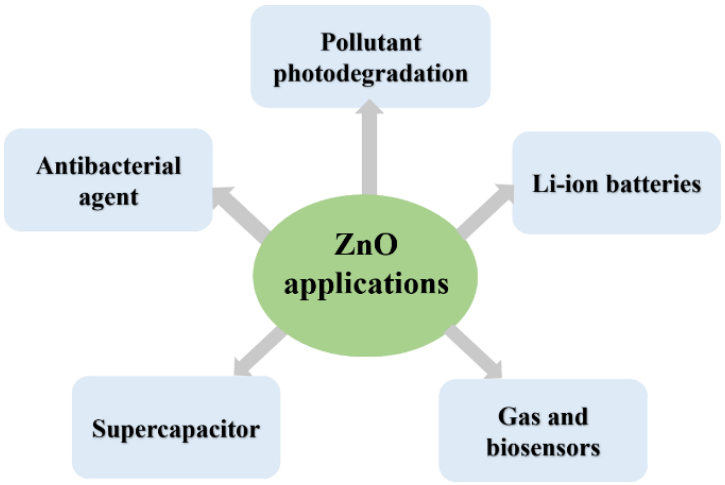

Figure 1.2: Examples of some important applications of ZnO nanostructures.

When ZnO films and associated devices are scaled down to nanoscale regime, the surface to volume ratio increases and the surface and interface play an important role in determining the material's properties, consequently the nanoscale structured ZnO exhibit some unique properties different from their bulk counterparts [11, 26, 27]. The confinement and interface effect can be altered in ZnO thin film by selecting an appropriate substrate as the choice of substrate also control these effects in ZnO nanostructures [28-30].

Defects in ZnO play a critical role in tuning its structural, optical and electronic properties. Native defects, such as oxygen vacancies, zinc interstitials, and oxygen interstitials, can significantly influence its excitonic behavior. These defects often act as deep or shallow donor/acceptor states within the bandgap, altering the material's absorption, emission, and conductivity characteristics. For instance, oxygen vacancies are commonly associated with green luminescence, while zinc interstitials can enhance n-type conductivity [31]. Understanding the types, concentrations, and distributions of these intrinsic defects is crucial for optimizing ZnO's performance in excitonic and optoelectronic applications [32].

Deep-level defects manifest as broad emissions in the photoluminescence (PL) spectra, particularly in the long wavelength region. Structural disorder in nanostructured ZnO significantly influences its optical properties, which has broad applications across various research fields. The distribution of these defects is often quantified by Urbach energy, associated with structural and/or thermal disorder [33]. The defect-induced exponential increase in photo absorption (PA) in the sub-bandgap region of semiconductors, as parameterized by Urbach energy, is universally observed. A higher Urbach energy indicates a broader distribution of defect levels within the crystal system. Numerous studies have reported the presence of Urbach tails in nanostructured ZnO systems, including ZnO nanocrystals and thin films [34-37]. Modulating ZnO defects is a key strategy for tailoring its properties for specific excitonic applications.

Over the years, researchers have developed numerous techniques, such as atomic layer deposition (ALD), pulsed laser deposition (PLD), chemical vapor deposition (CVD), molecular beam epitaxy (MBE), and magnetron sputtering, to grow high yield quality thin films with good crystallinity, low defect concentration and reproducible tunable electronic and optical properties [28]. It has been reported that ZnO film grown by these PLD, ALD, sputtering has preferred orientation along (002) direction on substrate at different deposition conditions, which allowed the control of the structure, defects or disorders, and thus the excitonic and optical properties of the films [38]. Techniques such as doping, annealing, and ion implantation can introduce or suppress defects in a controlled manner. Along with these structural growth mediated defects and disorders the doping of ZnO with transition metals (such as Fe, Co, Ni, Mn etc.) can introduce new luminescence centres [39, 40]. Additionally, defect engineering through advanced fabrication techniques,

such as Atomic Layer Deposition (ALD), Sol-gel, etc., enables precise control over defect density and spatial distribution.

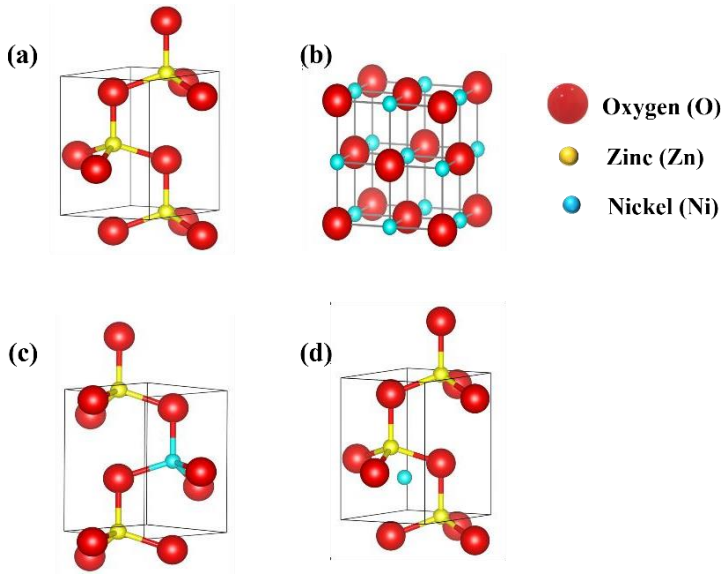

Figure 1.3: Schematic representation of crystal structures (a) ZnO wurtzite hexagonal, (b) NiO cubic structure, (c) Ni doped ZnO (Zn^{2+} replaced by Ni^{2+}), (d) Ni doped ZnO (Ni is at interstitial position).

Among these dopants the attention has been focused on Ni doped ZnO for significantly enhancing the material's properties, making it suitable for various advanced applications such as in spintronics, opto-electronics and sensing devices and it also improves the photocatalytic activity. The effect of Ni doping in ZnO not only induces a change in magnetic behaviour, but also imparts shift in the optical band gap [41, 42]. The combined effects of magnetic and optical characteristics, makes it an important source for the use in monolithic optical integrated circuit application with higher threshold [43]. The chemical stability of Ni^{2+} while occupying Zn^{2+} sites, makes it unique and identifies it as one of the most efficient doping element as it enhances ZnO with optical and electrical properties [44]. Therefore, Ni ions can be used to tune optical, electrical and magnetic properties of ZnO [45]. In addition, for higher doping

concentrations, Ni has the tendency to form clusters of metallic Ni or NiO as secondary phase; due to the solubility limit of Ni within ZnO host lattice. The as-prepared Ni-doped ZnO can be considered as potential candidate for spintronics, photodegradation of dyes, dye sensitized solar cells (DSSCs), etc. Their optical/magnetic properties are important in solar cells particularly in DSSCs as its photovoltaic responses such as short circuit current density and photocurrent conversion efficiency is influenced by magnetic effect [46].

The ability to modulate ZnO's defects opens exciting avenues for designing excitonic devices with tailored functionalities. By leveraging the interplay between ZnO's intrinsic structure and defect states, researchers can develop innovative solutions for next-generation optoelectronic and photonic technologies.

Based on this background, in the present thesis we explore the effect of surface/interface and consequently the effect of confinement for the direct bandgap semiconducting material i.e. zinc oxide (ZnO), in terms of its structural/morphological and optical properties. Specifically, the thesis work presents the effect of confinement in such ZnO nanostructured systems, where surface and interfaces play dominating role, along with the demonstration of growth mediated disorders/defects, which affects the structural and overall electronic/optical properties of the systems. Furthermore, we demonstrate the important effect of controlled external metal doping, e.g., Ni doping, in ZnO nanostructures to vary the structural/configurational and electronic properties in non-monotonous manner.

1.4 Objective and scope of this thesis

The work is focused towards the study of thickness dependent optical/electronic properties of metal-oxide (zinc oxide, ZnO) nanostructured thin-films, and effect of growth mediated disorder in the

atomic layer deposition (ALD) grown ZnO thin films of thickness range from ~2 nm to ~70 nm. On the other hand, we explore the effect of various concentration of metal (Ni) doping (in the range of Ni doping from 0 to 10 mol %) to introduce the extrinsic defects in nanostructured ZnO systems, specifically the ZnO nanoparticles, towards the controlled variation in structural and electronic properties of the systems, where ZnO nanoparticles were synthesized by sol-gel method.

1.5 Thesis outline

The chapter contents of the thesis are summarized as follows:

Chapter 1: It offers a brief overview, examines the state of the topic at present, and specifies the objectives to be met.

Chapter 2: It deals with the details of the experimental methodology used for the experimental work carried out in the thesis and procedures for the fabrication of the ZnO nanostructures (thin films and nanoparticles). The general background and overview of growth techniques employed (such as atomic layer deposition (ALD) for ZnO thin film growth and sol-gel method in synthesizing Ni doped ZnO nanoparticles) are also summarized in this chapter, along with their mechanism, characteristics and unique advantages over other growth techniques. It also summarizes various equipment used for various measurements, such as x-ray scattering technique involving x-ray diffraction (XRD) and x-ray reflectivity (XRR), UV-Vis spectroscopy, photoluminescence (PL) spectroscopy, Raman spectroscopy, photocatalytic activity etc., carried out during the research work.

Chapter 3: In this chapter we explore the thickness dependent optical/electronic properties of metal-oxide (zinc oxide, ZnO) nanostructured thin-films. This chapter presents the studies of optical/electronic properties of ALD grown ZnO thin films (ZnO_a) as function of film thickness. The studies on excitons and effect of growth

mediated disorder have been presented. Photoabsorption (PA) and photoluminescence (PL) measurements were employed for this purpose. Observation of quantum confinement effect (up to a threshold thickness ~20 nm) has been demonstrated and explained consistently with PA and PL studies. Moreover, an interesting phenomenon involving a non-monotonic change in the optical properties with increase of ZnO film thickness (at above the threshold thickness range) has been explored in details in this chapter.

Chapter 4: In this chapter, the origin of the observed non-monotonic change in the optical properties of ZnO with increasing film thickness (as demonstrated in Chapter 3) has been explored. Identification of the phenomena involving self-healing of defect mediated disorder in ZnO thin films, has been discussed in this chapter. For this purpose, the structure and morphology of the ZnO films of different thicknesses were studied elaborately via conducting XRD and FESEM. The results from FESEM and XRD, in combination with PL study, were utilized to explain the observed phenomena of spontaneous decrease of disorder (i.e., the non-monotonic variation in optical/electronic properties, as mentioned above) as a function of ZnO film thickness (*d),* above a threshold thickness of about ~20 nm. The results signify the occurrence of change of growth mode from an essentially smooth to a grainy structure, at around threshold thickness, and relates it to a mechanism of self-healing process of defect mediated (Zn interstitial) disorder in ZnO thin films.

Chapter 5: In this chapter**,** we explore the effect of concentration of metal doping to introduce the extrinsic defects in nanostructured ZnO systems towards the controlled variation in structural and electronic properties. We examine the defect induced structural configuration and corresponding electronic properties. Here specifically, we explore the defect mediated structural changes in ZnO nanoparticles due to different concentration of nickel (Ni) metal doping. For this study, different sets of Ni-dopped ZnO nanoparticle systems were synthesized by sol-gel method, with varying doping concentration from 0 (i.e., pure ZnO

nanoparticles) to 10 molar percent. The structural properties in Ni doped ZnO was investigated by employing x-ray diffraction (XRD) technique. X-ray diffraction (XRD) technique and Raman spectroscopy were employed to investigate the to investigate the structural/configurational/electronic changes in ZnO nanostructure due to the extrinsic defects generated by different concentration of Ni-doping. Finally, to explore whether these external doping mediated variation in structural configuration/ defects for such Ni doped ZnO nanostructures can exhibit any effect in their application in terms of their applications involving their structural, thus electronic properties, we carried out experiments with photocatalytic activity measurements, which has been presented in this chapter.

Chapter 6: The findings and conclusions drawn from the previously stated research are compiled in this chapter. The potential future scope of work that that can be carried out for further development in this field, is also covered in this chapter.

Chapter 2

Experimental and Characterization Techniques

This chapter provides a detailed description of the experimental procedures, characterization techniques, and sample preparation methods employed in this research work.

2.1 Atomic Layer Deposition (ALD) Technique

2.1.1 Fundamentals of ALD

Atomic layer deposition (ALD) is a vapor-phase deposition technique widely recognized for its ability to deposit thin films with exceptional precision and control [47]. In recent years, ALD has demonstrated significant potential in advanced semiconductor and energy conversion technologies. As device designs evolve to include smaller and more complex structures, ALD has emerged as a preferred method due to its superior conformality and precise control over film thickness and composition[47, 48]. The key to these unique capabilities lies in the cyclic and self-saturating nature of the ALD process.

2.1.2 Mechanisms

A schematic representation of the general ALD process is shown in Figure 2.1, which illustrates the ALD cycle. The ALD process involves sequential and alternating pulses of gaseous chemical precursors, which react with the substrate surface in distinct steps known as "half-reactions." Initially, precursor A is pulsed into the reactor chamber under the required vacuum conditions for a specified time, allowing it to fully react with the substrate surface through a self-limiting mechanism. Following this, an inert carrier gas (commonly N_2 or Ar) is used to purge the chamber, which removes the unreacted precursor or undesired

reaction by-products. Subsequently, precursor B is introduced, followed by another purge cycle with the inert gas, resulting in the deposition of a monolayer of the target material. This cyclic process is repeated until the desired film thickness is achieved.

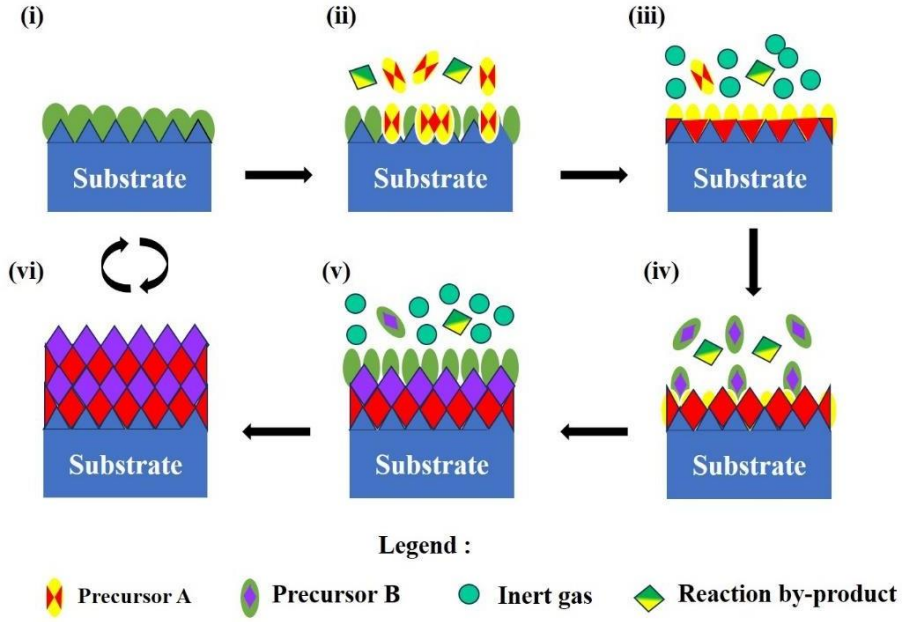

Figure 2.1: Schematic of the sequential ALD process. (i) Functionalized substrate, (ii) Precursor A is pulsed into the ALD chamber and it reacts with the substrate surface, (iii) Excess precursor and reaction by-products are purged with the inert carrier gas, (iv) Precursor B is pulsed into the ALD chamber, (v) Excess precursor and reaction by-products are purged with the inert carrier gas, and (vi) Steps ii–v is repeated until the desired film thickness is achieved.

2.1.3 Sample Preparation by ALD

The surface reactions in ALD are different significantly from other deposition techniques due to the sequential supply of the reactive precursor gases. For demonstrating the surface chemistry of the ALD process in detail, we have illustrated in Figure 2.2, a schematic of ALD deposition of zinc oxide (ALD-ZnO). The most successful ALD process of ZnO (ALD-ZnO) uses diethylzinc (DEZ, Zn $(C_2H_5)_2$) and water (H_2O) as precursors, as displayed in Figure 2.2. The principle of ALD-ZnO

growth from DEZ and H_2O consists of two self-terminating reactions described in equations **(2.1)** & **(2.2)** as follows [49, 50]:

$$ZnOH^* + Zn(CH_2CH_3)_2 \rightarrow ZnO - ZnCH_2CH_3^* + CH_3CH_3 \quad \textbf{(2.1)}$$

$$ZnCH_2CH_3^* + H_2O \rightarrow ZnOH^* + CH_3CH_3 \quad \textbf{(2.2)}$$

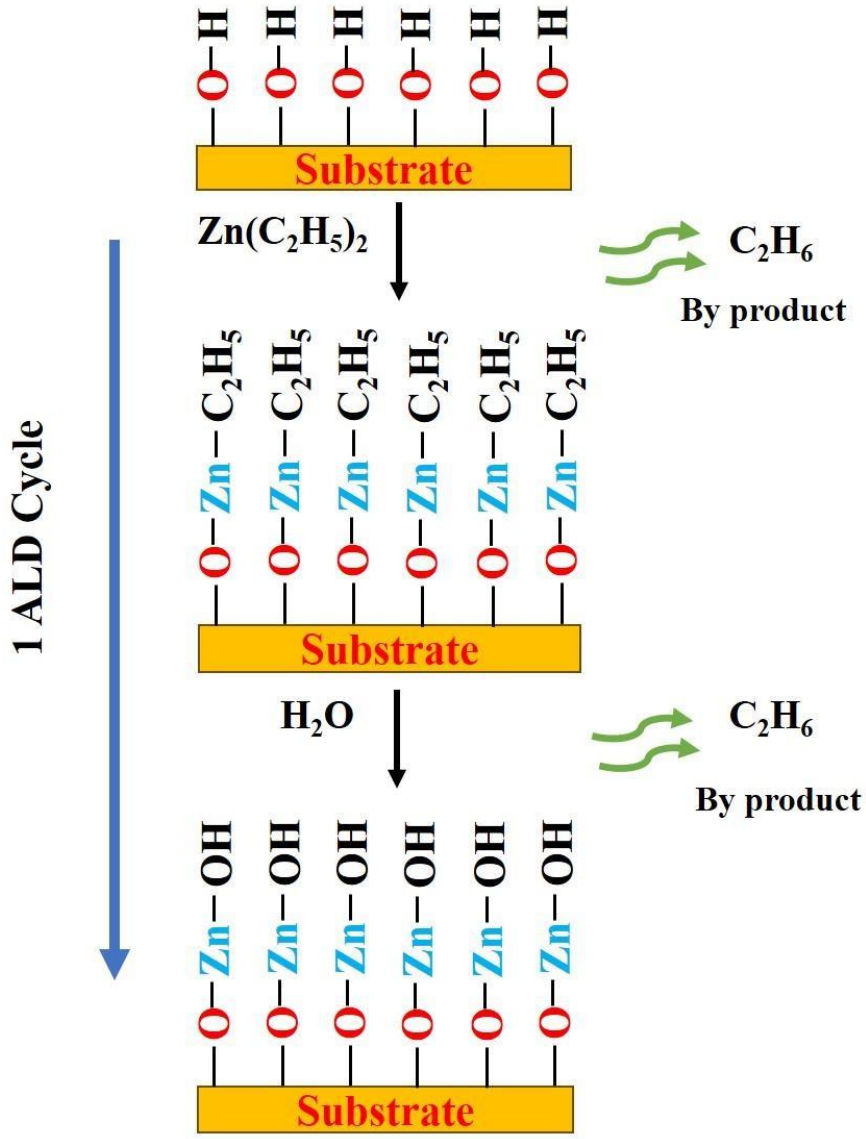

Figure 2.2: Schematic representation of ALD-ZnO growth.

Three key parameters play a vital role in determining the characteristics of the ALD process: deposition temperature, precursors, and purging time. Deposition temperature is particularly important for maintaining the self-limiting nature of ALD. The details for sample preparation are as follows:

ZnO thin films were grown on polished fused quartz (SiO_2) substrates of low roughness (< 5Å) at a growth temperature of 200 ºC using a BENEQ TFS-200ALD reactor. Before loading the substrates into the ALD reactor, all the substrates were sequentially cleaned in acetone and ethanol for 2 mins in an ultrasonic bath. They were afterwards kept in deionized (DI) water and finally dried in nitrogen (N_2, 99.999% purity). Diethyl zinc [DEZn, $Zn(C_2H_5)_2$, [Sigma-Aldrich] and DI water were used as precursors for Zn and oxygen respectively. Nitrogen (N_2, 99.999% purity) was used both as a carrier and purging gas. The precursors were alternatively introduced into the reactor using their intrinsic vapor pressures from external containers kept at 18 ºC. The reactor pressure during the growth was kept at 1.75 mbar. One ALD reaction cycle consisted of 0.2 s exposure to DEZ, followed by 0.75 s for N_2 purge, 0.2 s exposure to H_2O and then N_2 purge for 0.75 s. Based on the standard operating mode [51, 52], the mentioned values of growth parameters were set for attaining the saturation level, which exhibit a steady-state growth. The chosen growth temperature is sufficient for taking place of the surface reactions but, not for initiating desorption of the precursors (being in the "ALD window"), so that the only limiting process is chemisorption and reaction [51-54].

2.1.4 Experimental setup of ALD

The experimental setup of our ALD system is shown in Figure 2.3. BENEQ TFS-200 ALD reactor is used in this experimental work.

Figure 2.3: ALD system used in the present research work.

A simplified schematic of the ALD reactor used in our research work has been shown in Figure 2.4.

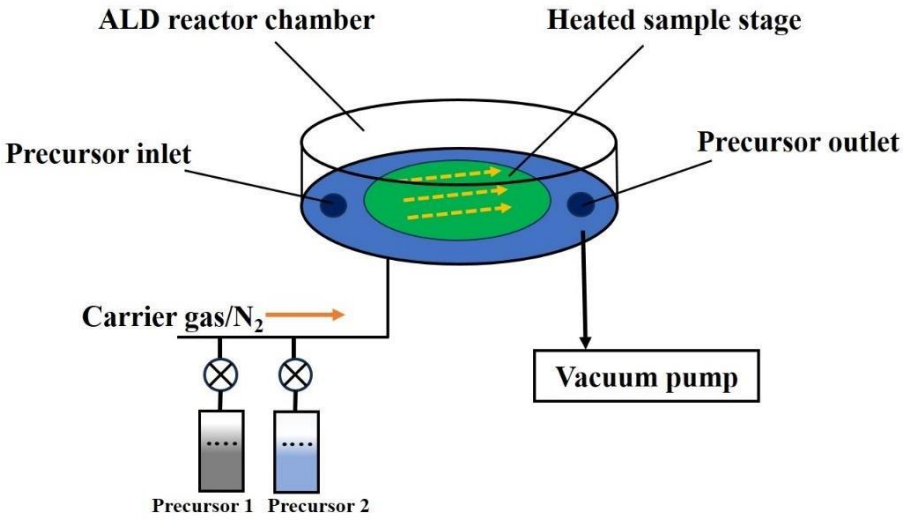

Figure 2.4: Simplified schematic of the ALD reactor used in the present research work.

2.2 Sol-Gel

The sol-gel technique is a versatile and widely used method for the synthesis of nanostructured materials, including thin films, nanoparticles, and porous structures [55]. This method involves the transition of a solution system (sol) into a solid-phase network (gel) through hydrolysis and polycondensation reactions of precursor molecules. The sol-gel process is especially favored for the fabrication of oxide materials due to its ability to produce high-purity and homogenous materials under relatively mild conditions [56, 57].

Process Description

These are following different steps involved in sol-gel process.

- Sol Preparation: The process typically begins with the preparation of a sol, which is a colloidal suspension of precursor molecules such as metal alkoxides (e.g., zinc acetate, titanium

isopropoxide) or metal salts in a suitable solvent, often an alcohol.

- Hydrolysis and Condensation: The precursor molecules undergo hydrolysis and condensation reactions when water is added to the system, often in the presence of an acid or base catalyst. These reactions lead to the formation of a three-dimensional network of oxo-bridges (M–O–M, where M is the metal ion), resulting in a gel.
    - Hydrolysis:

$$M(OR)_X + H_2O \rightarrow M(OH)_{X-1} + ROH$$

    - Condensation:

$$M(OH) + M(OR) \rightarrow \mathrm{M-O-M + ROH}$$

    Where M is central metal atom in the precursor, O is oxygen, H hydrogen atom from water (H_2O) or hydroxyl (OH) groups. R is organic group (alkyl group) attached to the metal, and X is number of organic groups.
- Gelation: The sol transitions into a gel through further condensation and cross-linking of the hydrolyzed species, forming a solid network within the liquid medium.
- Drying: The gel is dried to remove the solvent and water, leaving behind a porous material. Careful control of the drying process is essential to prevent cracking or shrinkage.
- Calcination: Finally, the dried gel is subjected to heat treatment (calcination) to remove any residual organic components and to densify the material, yielding the desired oxide structure.

Advantages of the Sol-Gel Technique

The sol-gel technique offers several advantages, making it a widely used method in material synthesis:

- Versatility: Applicable to a wide range of materials, including metal oxides and composites.
- Homogeneity: Ensures uniform mixing of components at the molecular level.

- Controlled Microstructure: Allows precise control over particle size, porosity, and morphology.
- Low Processing Temperature: Suitable for the synthesis of temperature-sensitive materials.

We have synthesized the ZnO nanostructure and Ni doped ZnO nanostructure using sol-gel technique [58]. The method is described below:

In this process, Zinc Acetate and Nickel Acetate were taken in the required amount as precursors for synthesizing different Ni-doped ZnO samples with different percentages of Ni-doping. Then, they were added with 2-methoxy ethanol and kept on a hot plate for 15 minutes for stirring by a magnetic stirrer at 300 rpm. At the same time, the required amount of mono-ethanolamine was mixed with the solution as a stabilizer. Then, the solution was stirred at 400 rpm and heated at 60 ºC for 60 minutes. After that, the solution was kept overnight. As a result of this, a clear solution was obtained. Then the solution was kept inside a hot air oven for drying. The sample then formed a gel-like consistency. It was subsequently calcinated in a box furnace.

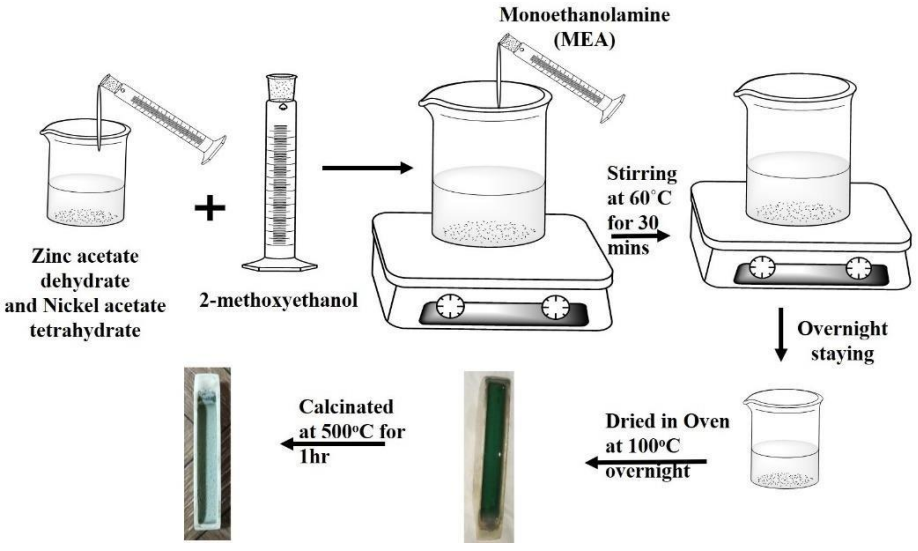

Figure 2.5: Schematic showing the synthesis of Ni-doped ZnO nanoparticle using Sol-gel process with different Ni concentrations (from 0 mol% to 10 mol%).

2.3 Physical Characterization Techniques

2.3.1 X-ray Scattering

X-ray scattering techniques, e.g., X-ray reflectivity (XRR) and X-ray diffraction (XRD) have been used in this present work. The thickness of the ZnO films was determined by using X-ray reflectivity (XRR) measurements. The crystalline structures of the ZnO films were investigated by X-ray diffraction (XRD).

Experimental setup

XRR and XRD measurements were conducted using Rigaku Smart Lab automated multipurpose X-ray diffractometer with Cu K_α radiation (λ = 1.54 Å).

Generally, there are three basic elements in X-ray diffractometer

(i) X-ray source

(ii) Sample stage

(iii) X-ray detector

X-rays for research purposes are produced in a standard way: by accelerating electrons with a high voltage and then allowing them to collide with a metal target. X-rays are produced when these electrons are suddenly deaccelerated upon collision with the metal target; these X-rays are called bremsstrahlung or "braking radiation". If the bombarding electrons are having sufficient energy, they can knock an electron out from the inner shells of the target metal atoms. Then electrons from higher energy states drop down to lower energy states to fill the vacancy, emitting x-ray photons with precise energies determined by the electron energy levels. Those X-rays are called characteristic X-rays. Characteristic X-rays are used for determining crystal structures of X-ray diffraction. The most common target material for X-ray diffraction is Copper, with Cu K_α radiation (λ = 1.54 Å). These X-rays are collimated and directed onto the sample of interest. When the geometry of the incident X-rays impinging the sample satisfies the Bragg Equation, constructive interference happens. A detector records and processes this

X-ray signal and converts the signal to a count rate which is then output to a device such as a computer monitor.

The experimental setup is shown in Figure 2.6.

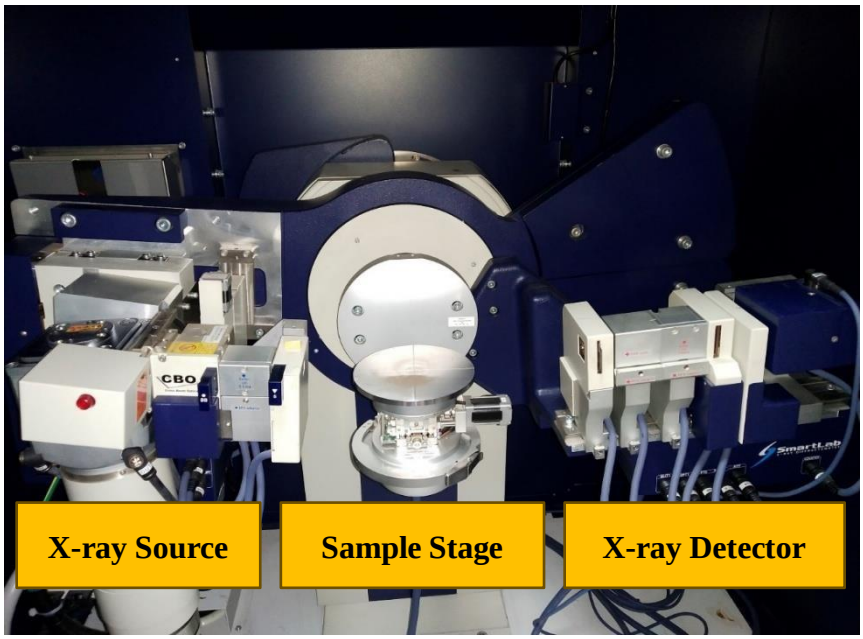

Figure 2.6: X-ray diffractometer used in the present research work.

A Theoretical Background of X-ray Scattering

X-ray scattering techniques are a family of non-destructive analytic techniques which reveal information about the crystal structure, chemical composition, and physical properties of the polycrystalline materials and thin films [59]. X-ray scattering is a probe for the investigation of surfaces on angstrom scales. This technique is non-destructive and the specimen requires no special conditioning and also measurements can be done under ambient conditions.

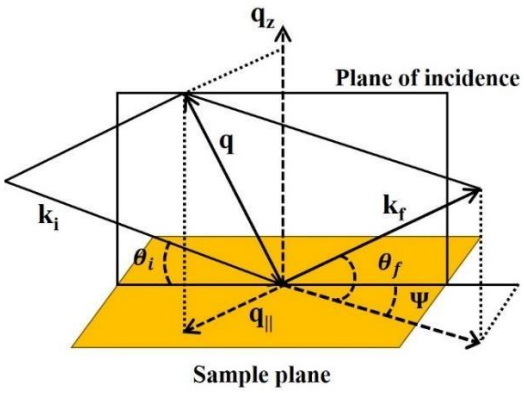

Figure 2.7: Schematic showing the generalized scattering geometry.

Figure 2.7 shows the schematic for scattering geometry in the general case of a surface experiment. The plane of incidence contains the incident wave vector $\boldsymbol{k_i}$ and the normal to the surface. If $\boldsymbol{k_f}$ is the scattered wave vector, then the momentum transfer vector $\boldsymbol{q}$ is given by equation **(2.3)**[59, 60],

$$\boldsymbol{q} = \boldsymbol{k_f} - \boldsymbol{k_i} \quad \textbf{(2.3)}$$

The components of $\boldsymbol{q}$ in x, y, and z directions are given by equations **(2.4)**, **(2.5)** & **(2.6)** respectively,

$$q_x = k_0(\cos\theta_f \cos\psi - \cos\theta_i) \quad \textbf{(2.4)}$$

$$q_y = k_0(\cos\theta_f \sin\psi) \quad \textbf{(2.5)}$$

$$q_z = k_0(\sin\theta_f + \sin\theta_i) \quad \textbf{(2.6)}$$

Where the components of $\boldsymbol{q}$, parallel to the sample surface are q_x, q_y and perpendicular to the sample surface is q_z.

Where $k_0 = 2\pi/\lambda$, λ is the wavelength of the incident radiation. In a reflectivity experiment, we work in the plane of incidence and thus we have an in-plane angle $\psi = 0$. In specular reflectivity, the incident angle (θ_i) and the scattered angle (θ_f) are kept equal. This provides information about the thickness and electron density profile of the individual layers and the interfacial roughness [61, 62]. Off-specular diffuse scattering $(\theta_i \neq \theta_f)$ gives a better understanding of the in-plane correlation and also the correlation between the interfaces [61, 63]. The specular reflectivity technique has been discussed below.

2.3.1.1 X-Ray Reflectivity

In X-ray reflectivity measurements, a well-collimated monochromatic X-ray beam is made to be incident on the sample surface at a grazing angle θ_i (starting from a few milli-radians) and the reflected intensity is recorded in the plane of incidence at an angle θ_f .If the angle of incidence of impinging X-rays is sufficiently small, penetration depth and the scattering is limited to the surface region. X-ray reflectivity (XRR) is an

important non-destructive characterization technique for studying the structure and the organization of the thin films at the nanometric scales [60, 64]. The XRR technique has the following characteristics: (i) it can be used to measure film thickness precisely from a few nm to 100 nm, (ii) it can be used for determining the surface and interface roughness and electron density of thin films, and (iii) it can be also used to investigate the layer structure of multilayer thin films.

Basic principles and Theory of X-ray reflectivity

X-rays are part of the electromagnetic spectrum. The most widely used X-rays in materials science are having a typical wavelength, of the order of 1 Å. The interaction of X-rays with matter can be described by the index of refraction, n, which basically characterizes the change of direction of the X-ray when it passes from air to a material. The index of refraction for X-rays can be written as written in equation **(2.7)** [60]:

$$n = 1 - \delta + i\beta \quad \textbf{(2.7)}$$

With, $\delta = \frac{\lambda^2}{2\pi} r_e \rho_e$ **(2.8)**

and, $\beta = \frac{\lambda}{4\pi}\mu$ **(2.9)**

Where δ and β signify for the scattering and absorption of the material, respectively; $r_e = 2.82 \times 10^{-15}$ m in the classical electron radius, ρ_e is the electron density of the material, and μ is the absorption length.

In the case of X-rays, the refractive index of a material is slightly less than unity. When an X-ray passes from air to the reflecting material, it is possible for the beam to reflect entirely from the surface, if the incident angle, θ (the angle between the incident beam and the surface of the sample) is smaller than the critical angle θ_c. This is called the total external reflection of X-rays. Then from Snell's law:

$$\cos\theta_c = n = 1 - \delta \quad \textbf{(2.10)}$$

As n is very close to unity, the angle θ_c is very small and a Taylor series approximation of θ_c gives:

$$\theta_c^2 = 2\delta = \frac{r_e\lambda^2}{\pi}\rho_e \quad \textbf{(2.11)}$$

Using the values of the typical parameters given above, θ_c is of the order one milli-radian. When an X-ray beam is incident on a flat material, part of the intensity is reflected and part of it is transmitted through the material. If the surface of the material is flat, the reflected intensity will be confined in a direction symmetric from the incident one and will be named specular. The specular reflectivity can be defined as:

$$R(\theta) = \frac{I_r(\theta)}{I_0} \quad \textbf{(2.12)}$$

Where I_0 is the incident intensity and $I_r(\theta)$ is the reflected intensity at an angle θ. The domain of validity of X-ray reflectivity is limited to small incident angles, where it is possible to consider the electron density as a continuous [64]. In this approximation, the reflection can be considered as a classical problem of reflection of an electromagnetic wave at the interface. This leads to the classical Fresnel relationship which gives the reflection coefficient in amplitude for the (s) and (p) polarization. The reflectivity which is the modulus square of this coefficient can be formulated in the case of X-rays as written in equation **(2.13)**:

$$R(\theta) = rr^* = \left|\frac{\theta-\sqrt{\theta^2-\theta_c^2-2i\beta}}{\theta+\sqrt{\theta^2-\theta_c^2-2i\beta}}\right|^2 \quad \textbf{(2.13)}$$

The equation is independent of the polarization. The X-ray reflectivity can be observed only in specular conditions (i.e., the incident angle is equal to the exit angle).

Figure 2.8 depicts the geometry for XRR in specular conditions.

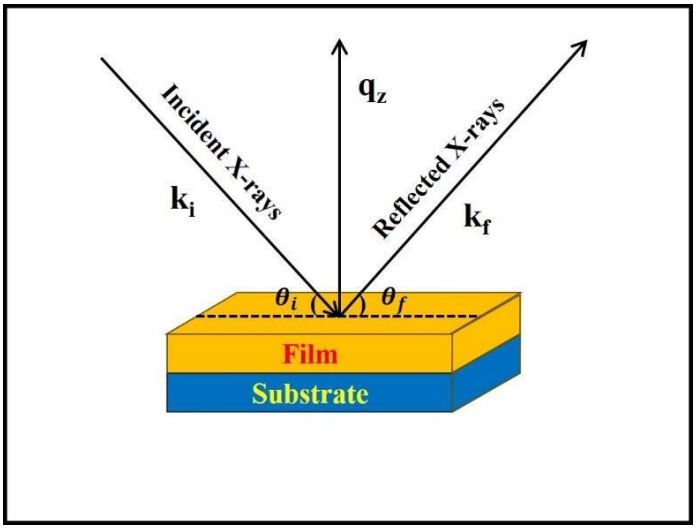

Figure 2.8: Geometry for X-ray reflectivity in specular conditions.

Specular reflectivity scans, i.e., scans in the plane that contains the incident beam and the normal to the sample surface, with incident angle $\boldsymbol{\theta_i}$ = scattering angle $\boldsymbol{\theta_f}$, were performed with the variation of the incident angle. If $\boldsymbol{q} = \boldsymbol{k_f} - \boldsymbol{k_i}$ is the momentum transfer vector and $\boldsymbol{k_f}$ and $\boldsymbol{k_i}$ are the scattered and incident X-ray wave vector respectively, then this geometry makes the components in the sample plane, $\boldsymbol{q_x} = \boldsymbol{q_y} = \boldsymbol{0}$, and $\boldsymbol{q_z}$ $(= (\frac{\boldsymbol{4\pi}}{\boldsymbol{\lambda}}) \boldsymbol{\sin\theta_i})$, the component normal to the surface. The X-ray reflectivity, $\boldsymbol{R(q_z)}$, calculated from any electron density $\boldsymbol{\rho(z)}$, is [65, 66]:

$$R(q_z) = R_F(q_z) \left| \frac{1}{\Delta\rho} \int \frac{d\rho(z)}{dz} e^{-iz\sqrt{q_z(q_z^2 - q_c^2)^{1/2}}} dz \right|^2 \qquad \textbf{(2.14)}$$

Where, R_F is the Fresnel reflectivity obtained from a single ideal step-function interface, $\Delta\rho$ is the total change in electron density across the interface and q_c is the momentum transfer at a critical angle for total external reflection. Equation **(2.14)** can be used to calculate $R(q_z)$ from a given analytic function $\rho(z)$ but the calculation of the reverse is not simple. When $R(q_z)$ is experimental data collected over a finite range and with finite accuracy, we cannot directly calculate $\rho(z)$. The general procedure to solve the inverse problems has been employed for the analysis of x-ray reflectivity data: a model $\rho(z)$, specifically a slab model is assumed, and parameters in the model are adjusted until a good

fit of the data has been achieved, following the Parratt formalism [67-71]. This expression for reflectivity (equation **2.15**) is valid for an ideally smooth interface, and is then modified in the presence of the Gaussian interface width or 'roughness' (σ) as:

$$R^{rough}(q_z) = R(q_z)\exp(-q^2\sigma_z^2) \quad \textbf{(2.15)}$$

The extracted values of film thickness, electron density, and interface width or roughness from the best fit of reflectivity data, were used to construct the electron density profiles (EDPs), i.e., the electron density as a function of film depth from the top for thin films (ZnO thin films), after convoluting the profile with the interface widths.

2.3.1.2 X-ray Diffraction

X-ray diffraction (XRD) is one of the most suitable and reliable techniques for probing the structure of a material as the wavelength of X-rays (of the order of Å) is comparable to the interatomic distances [72, 73]. XRD is a non-destructive method of calculating d-spacing (spacing between successive atomic planes), and therefore the lattice constants. Strain and mean crystallite size also can be determined from the XRD data. In XRD, X-ray is incident on the material at some incidence angle and gets diffracted through a different set of atomic planes which are present in the crystal structure. When, both, d (d-spacing) and θ (the angle of incidence of X-ray), satisfy Bragg relation $2d \sin\theta = n\lambda$ (here, d is the inter-planer distance, λ is the wavelength of incident X-ray and n is an integer), constructive interference happens between the diffracted waves. The diffracted X-ray photons are detected and counted then by the detectors. In this way with satisfying Bragg's condition, a peak, across the corresponding 2θ value appears in the intensity (I) verses angle (2θ) curve. Conversion of the diffraction peaks to d-spacing enables to identify the material under investigation. It is important to mention that the XRD pattern of each element/material is unique and can be considered as a signature of its structural phase. This uniqueness makes the XRD able to identify and validate the purity of a structural phase for a given material. XRD pattern consists of almost complete

information about the crystal structure, like lattice parameters, grain size, strain, phase composition, orientation etc. Schematic of the geometry for the XRD setup has been shown in figure 2.9. Here, 2θ is the angle between the incident beam and the diffracted beam, φ is the angle of rotation about a plane perpendicular to the surface, χ is the angle about the line parallel to the surface, whereas, ω is the angle between incident X-ray beam and sample surface. In '$\theta - 2\theta$' scanning, angle ω is treated as θ. Depending upon the type of information to be extracted; XRD can be operated in different scanning modes.

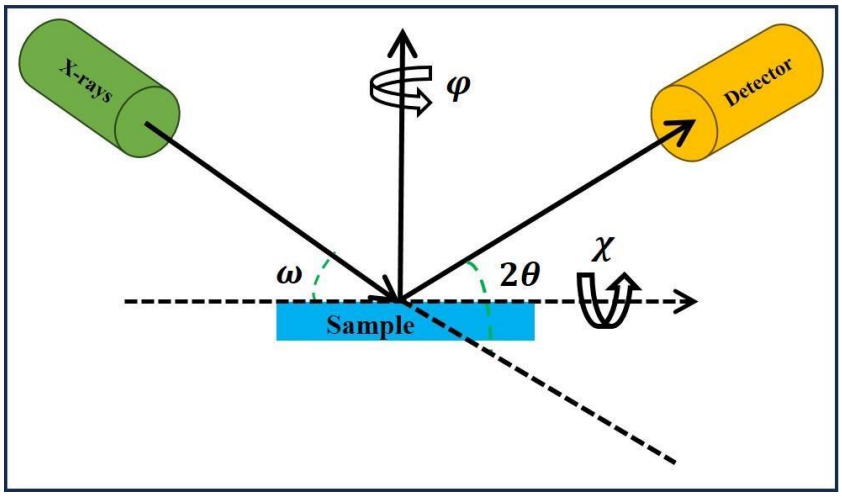

Figure 2.9: Schematic of the geometry for XRD.

2.3.2 UV-Visible Spectroscopy

Ultraviolet-visible (UV-Vis) spectroscopy refers to the absorption or reflection spectroscopy in the UV-Vis spectral region. After irradiation, molecules in a sample absorb light in the ultraviolet and visible part of the electromagnetic spectrum and undergo electronic transitions which give UV-Vis spectra. UV-Vis spectroscopy is a reliable analytical tool for the qualitative and quantitative analyses of the samples [74, 75]. The detailed theory of UV-Vis spectroscopy has been discussed in this section.

Experimental setup for UV-Visible Spectroscopy

The basic parts of the spectrophotometer are a light source, a diffraction grating in a monochromator, and a detector (see Figure 2.10). The light source has two lamps: a deuterium arc lamp (or D_2 lamp), which is in the range of 190 nm to 370 nm, used for the UV region; and a tungsten lamp (320-100 nm) used for the visible region.

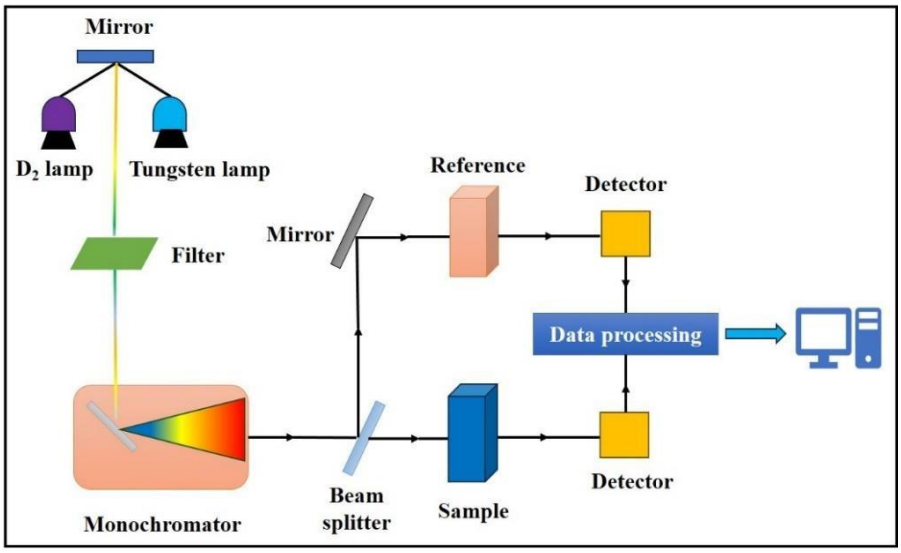

Figure 2.10: Schematic of the UV-Visible spectrophotometer.

The scanning monochromator allows the diffraction grating to "step through" each wavelength so that its intensity may be measured as a function of wavelength. Basically, this spectrophotometer is a double-beam spectrophotometer. The light is split into two beams before reaching the sample. One beam is used as the reference; the other beam passes through the sample. The reference beam intensity is taken as 100% transmission (or 0 absorbance), and the displayed measurement is the ratio of the two beam intensities. The output of the detector is a plot of intensity versus wavelength which gives information about the sample. The detectors used are typically photomultiplier tubes, photodiodes, or charged couple devices.

Chapter 2

Theory of UV-Visible Spectroscopy

When sample molecules are irradiated with UV or visible light having an energy equivalent to the possible electronic transition within the molecule, the electrons in the molecule absorb some of the light energies, are excited to a higher energy level, which is the characteristic of molecules. The principle of UV-Vis spectrophotometer follow the Beer-Lambert law. The law tells how the attenuation of light is related to the properties of the material through which the light is traveling.

This law is expressed through the equation:

$$A = \log_{10}(\frac{I_0}{I}) = \varepsilon lc \quad \textbf{(2.16)}$$

Where, A stands for the absorbance, I_0 refers to the intensity of light incident to the sample, I is the intensity of light transmitted from the sample, l stands for the length of the sample and ε refers to the molar absorptivity or molar extinction coefficient, which is the probability of electronic transitions. From the Beer-Lambert law, it has been established that if the number of molecules capable of absorbing light at a certain wavelength is more, then we will get a greater extent of the absorption of light.

A UV-Vis spectrophotometer records both the degree of absorption (i.e., intensity) and absorption peak for each wavelength. The resulting spectrum is a graph of absorbance versus wavelength. The wavelengths of the absorption peaks represent the types of bonds that are present in a given molecule and are valuable in determining the electronic transition in a molecule.

UV-Vis spectroscopy can be also used to explore the optical properties of thin films. The absorption coefficient α can be calculated from the Beer-Lambert's law as [76]:

$$\alpha = \frac{2.303 \ .Abs(\lambda)}{d} \quad \textbf{(2.17)}$$

Where, d and Abs are the film thickness and film absorbance, respectively. The optical band gap (E_g) can be obtained from absorption spectra.

Estimation of optical bandgap

The optical band gap of powder samples and thin films (i.e., Ni-doped ZnO powder samples, Ni-doped ZnO thin films, and ZnO thin films in this study) has been determined using the Tauc model [77, 78] and the Davis and Mott model [79] in the high absorbance region written in the equation :

$$\alpha(\nu)h\nu = B(h\nu - E_g)^n \quad \textbf{(2.18)}$$

Where E_g is the optical band gap, B is a constant, $h\nu$ is the incident photon energy and $\alpha(\nu)$ is the absorption coefficient. For the direct band gap semiconductor i.e., ZnO, $n = 1/2$ was appropriately found as it gives the best linear curve in the band-edge region, [80, 81] correspondingly, the relationship between $(\alpha h\nu)^2$ and $h\nu$ has been plotted. The band gap energy, E_g, can be determined by extrapolating the linear portion of $(\alpha h\nu)^2 = 0$ in that graph.

Estimation of Urbach energy

Along with this using the UV-Vis spectra we can also estimate the Urbach energy of thin films. Urbach energy is a parameter typically used to quantify energetic disorder in the band edges of a semiconductor. In the UV-Vis absorption spectra the Urbach tail dominates the absorption in the region just below the exciton peak. The absorption coefficient below the excitonic peak is modelled by Urbach rule described below [82],

$$\alpha = \alpha_0 \exp((h\nu - E_0)/E_u) \quad (2.19)$$

Where, α_0 and E_0 are characteristic parameters of the material, $h\nu$ is the photon energy and E_u is the Urbach energy. We need to fit the absorption data just below the free exciton peak to extract the Urbach energies. For this we further simplify the equation 2.19 as follows

$$\ln \alpha = h\nu/E_u + [\ln \alpha_0 - E_0/E_u] \quad (2.20)$$

This equation is equivalent to the line equation $y = mx + c$, where $m = 1/E_u$ is the slope of the curve. To estimate the Urbach energy we plot a graph between ln *α versus E* and then fit the linear region of this curve with linear equation, so the reciprocal of the of the slope of the curve gives the Urbach energy.

2.3.3 Photoluminescence Spectroscopy

Photoluminescence (PL) spectroscopy is a very efficient and important tool to investigate the optoelectronic properties of materials [83, 84]. When electron-hole pairs are created in a semiconductor, or when carriers are excited into higher energy levels from which they return to their equilibrium states, light can be emitted from the material [85]. Among semiconductors many of them are well suited for light emission, particularly the compound semiconductors having direct band gaps[85]. The general property of light emission is called luminescence. If carriers are excited by the absorption of photons, the radiation resulting from the recombination of the excited carriers is called photoluminescence. The detailed theory of Photoluminescence spectroscopy has been discussed below.

Experimental setup

A typical schematic representation of the PL spectrometer is shown in figure 2.11. The basic equipment setup contains two main parts: (i) a light source to provide excitation, and (ii) a detection system to collect and analyze photons emitted from the sample.

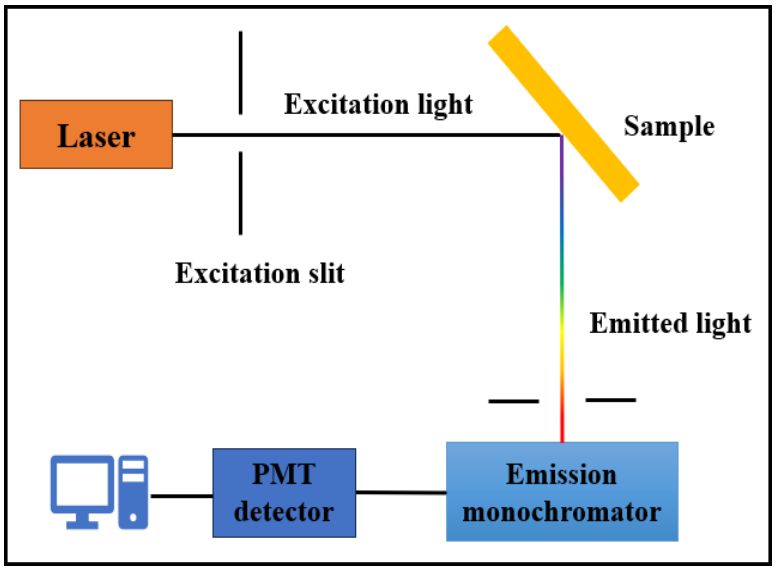

Figure 2.11: Schematic of PL spectrometer setup.

In this work, the photoluminescence (PL) emission from the ZnO films was measured at room temperature using a PL spectrometer (Dongwoo Optron DM 500i) having an excitation source consisting of a continuous wave He-Cd laser (excitation wavelength, 325 nm, PMT detector).

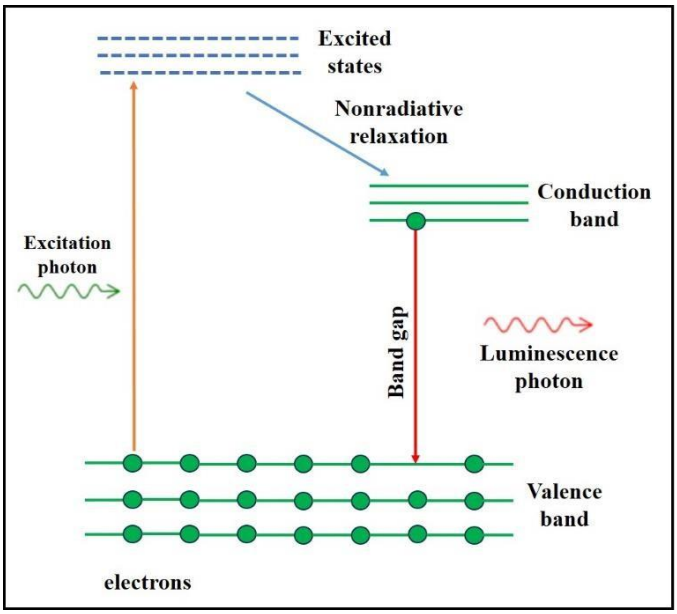

Figure 2.12: Principle of photoluminescence spectroscopy.

Theory of Photoluminescence

Photoexcitation causes electrons within the material to excite into permissible higher energy states. When these electrons return to their equilibrium states, the excess energy is released and may include the emission of light (a radiative process) or not (a non-radiative process) as shown in Figure 2.12. The energy of the emitted light is related to the difference in energy levels between the two electron states involved in the transition between the excited state and the equilibrium state. In semiconductor systems, the most common radiative transition is between states in the conduction and valence bands, with the energy difference being known as the bandgap. During a PL experiment, excitation is provided by laser light with energy much larger than the optical band gap. The photo-excited carriers consist of electrons and holes, which relax towards their respective band edges and recombine by emitting light at the energy of the band gap. Radiative transitions in

semiconductors may also involve localized defects or impurity levels, therefore, the analysis of the PL spectrum leads to the identification of specific defects or impurities, and the magnitude of the PL signal allows for determining their concentration. Thus, photoluminescence is a process of photon excitation followed by photon emission and is important for determining band gap, purity, crystalline quality, and impurity defect levels of semiconducting material. It also helps to understand the underlying physics of the recombination mechanism.

Photoluminescence (PL) is a very powerful technique to probe the crystallinity and defect-related information of ZnO films. In general, photoluminescence spectra of ZnO typically consist of two bands. One of these is the near band edge emission (NBE), i.e., free excitonic emission located near the energy of the band gap, i.e., in the UV region ($\sim 380\ nm$). This free excitonic PL (also called 'edge' PL) can only be seen in films of good structural quality, in which non-radiative processes are inefficient and in which carriers are not dominantly trapped by some defect centers [19, 86]. The second one is the defect-related deep-level emission (DLE) which is located in the visible region (generally green-yellow emission). Usually, the visible emission is considered to be related to various intrinsic defects present in ZnO [19, 86]. Native or intrinsic defects are imperfections in the crystal lattice that involve only the constituent elements. They include vacancies (missing atoms at regular lattice positions), interstitials (extra atoms occupying interstitial positions in the lattice), and antisites (a Zn atom occupying an O lattice site or vice versa). Figure 2.13 shows the defect energy levels in ZnO[87].

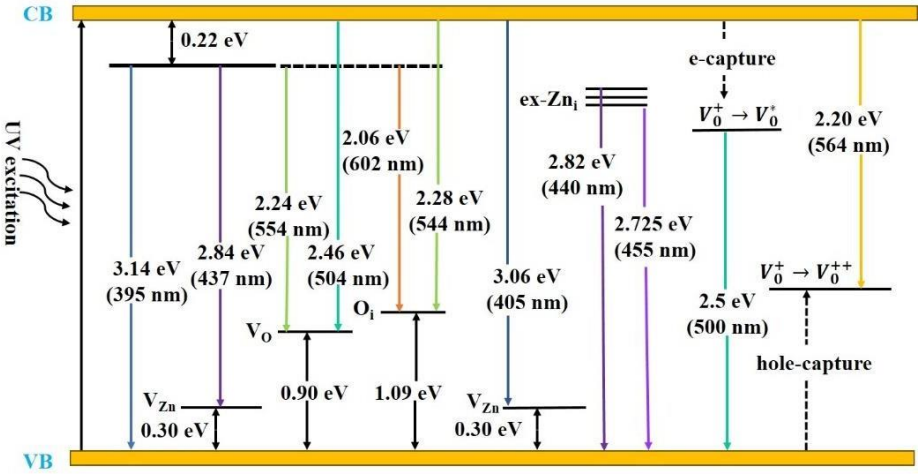

Figure 2.13: Energy level diagram showing some of the principal defect levels in ZnO. The ZnO has an assumed bandgap of 3.36 eV. Potential transitions between the various levels are color-coded [87].

Figure 2.12 shows various shallow and deep energy levels in ZnO originating from intrinsic defects present in the crystal. V_{Zn}, Zn_i, ex-Zn_i, V_O, V_0^+, V_0^{++}, V_0^* and O_i denotes zinc vacancy, $V_0^+ \rightarrow V_0^{++}$ Zinc interstitial, extended states of zinc interstitial, oxygen vacancy, singly charged oxygen vacancy, doubly charged oxygen vacancy, neutral state of oxygen vacancy, and oxide interstitial, respectively. Some of the photogenerated electrons and holes are tapped by these shallow and deep energy levels and correspond to different visible emissions.

2.3.4 Raman Spectroscopy

Raman spectroscopy is a spectroscopic technique which is used to observe vibrational, rotational, and other low-frequency phonon modes in a system [88, 89]. It is based on inelastic scattering of monochromatic light, usually from a laser source. Inelastic scattering means that the frequency of photons in monochromatic light changes upon interaction with a sample. Photons of the laser light are absorbed by the sample and then remitted. The frequency of the reemitted photons is shifted up or down in comparison with the original monochromatic frequency, which is called the Raman effect. This shift provides information about

vibrational, rotational, and other low-frequency transitions in molecules. Raman spectroscopy can be used to study solid, liquid, and gaseous samples. The detailed theory of Raman spectroscopy has been described below.

Experimental Setup for Raman Spectroscopy

Figure 2.14 shows the schematic of the experimental set-up of the Raman spectrometer. A Raman system typically consists of four major components: (i) excitation source (i.e., laser), (ii) sample illumination system and light collection optics, (iii) wavelength selector (filter or spectrophotometer), and (iv) detector (photodiode array, CCD or PMT).

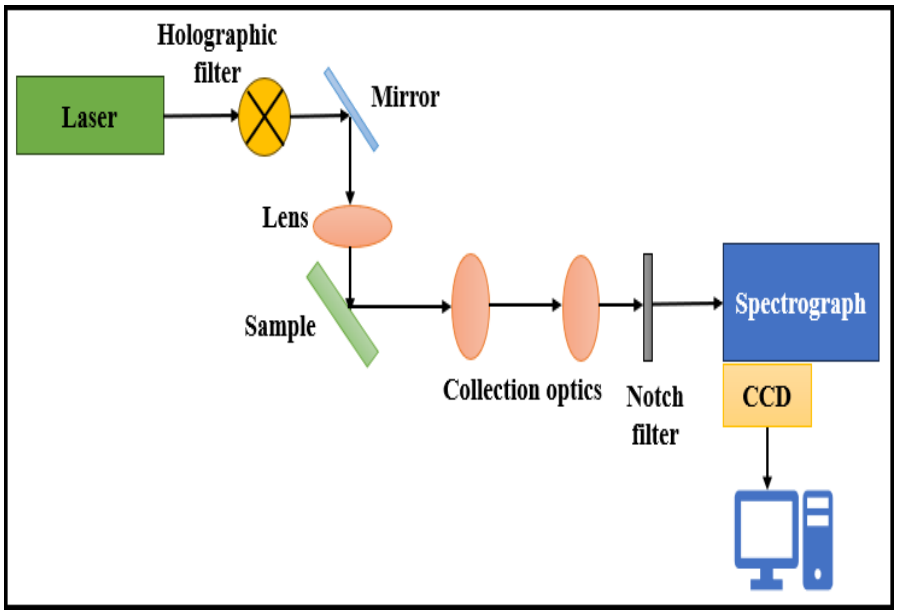

Figure 2.14: Schematic diagram of the Raman spectrometer.

In this work, Raman spectra were obtained using a Raman spectrometer (LabRAM HR Evolution, HORIBA Scientific) with a 633 nm He-Ne laser-focused on a spot of size ≈ 0.8 μm on the samples.

Theory of Raman Spectroscopy

The Raman effect is based on molecular deformations in electric field E determined by molecular polarizability α. The laser beam can be

considered as an oscillating electromagnetic wave with electric field vector E. By interacting with the sample it induces electric dipole moment, $P = \alpha E$, which deforms the molecules. Because of periodical deformation, molecules start vibrating with characteristic frequency ν_m. In other words, monochromatic laser light with frequency ν_0 excites molecules and transforms them into oscillating dipoles. Such oscillating dipoles emit light having three different frequencies (see figure 2.15), when:

(i) A molecule having no Raman-active modes absorbs a photon with the frequency ν_0. The excited molecule returns to the same basic vibrational state and emits light with the same frequency ν_0 as an excitation source. This type of interaction is called elastic Rayleigh scattering.

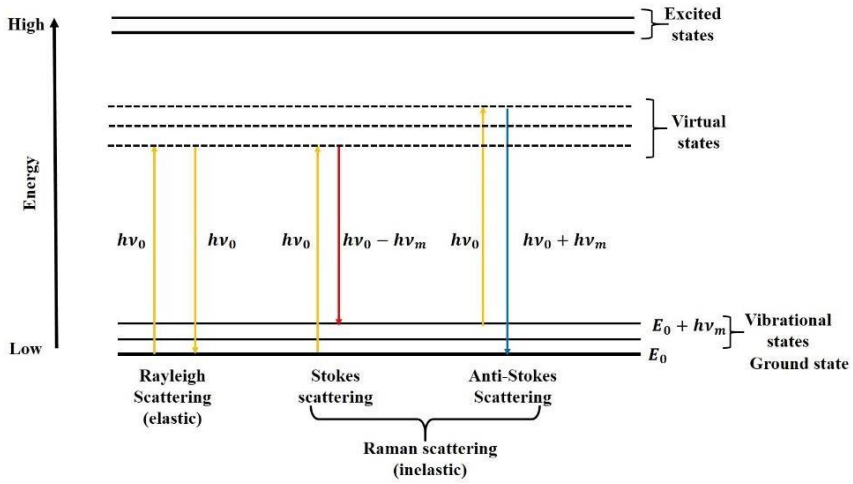

Figure 2.15: Energy-level diagram showing the states involved in Raman spectra.

(ii) A photon with frequency ν_0 is absorbed by the Raman-active molecule which at the time of interaction is in the basic vibrational state. Part of the photon's energy is transferred to the Raman-active mode with frequency ν_m and the resulting frequency of scattered light is reduced to $\nu_0 - \nu_m$. This Raman frequency is called Stokes frequency, or just 'Stokes'.

(iii) A photon with frequency ν_0 is absorbed by a Raman-active molecule, which, at the time of interaction, is already in the excited vibrational state. Excessive energy of excited Raman-active mode is released, the molecule returns to the basic vibrational state and the resulting frequency of scattered light goes up to $\nu_0 + \nu_m$. This Raman frequency is called Anti-Stokes frequency, or just 'Anti-Stokes'.

Most of the incident photons undergo elastic Rayleigh scattering. This type of signal is useless for practical purposes of molecular characterization. Only about 0.001% of the incident light produces an inelastic Raman signal with frequencies $\nu_0 \pm \nu_m$. Spontaneous Raman scattering is very weak and special measures should be taken to distinguish it from the predominant Rayleigh scattering. Instruments such as notch filters, tunable filters, laser stop apertures, and double and triple spectrometric systems are used to reduce Rayleigh scattering and obtain high-quality Raman spectra. Raman scattering is sensitive to the crystal lattice structure of ZnO through its vibrational properties. Raman spectroscopy is a non-destructive characterization technique, based on inelastic light scattering which provides information about the phonon vibrational and rotational mode properties of the said material. Wurtzite-type ZnO consists of space group C_{6v}^4 with two formula units in the primitive cell [90, 91]. Each primitive cell of ZnO consists of four atoms, each occupying C_{3v} sites, which gives 12 phonon branches: 9 optical modes and 3 acoustic modes [92]. At the center of the Brillouin zone (Γ point), it is predicted by the group theory that the following lattice optical phonons have the following irreducible representation [90] :

$$\Gamma_{opt} = 1A_1 + 2B_1 + 1E_1 + 2E_2 \qquad (2.21)$$

Where A_1 and E_1 are polar modes and both of them are infrared and Raman active. E_2 modes are non-polar and only Raman is active. The E_2 modes have two wave numbers, namely, E_2 (high) and E_2 (low) which are associated with the motion of Oxygen and Zn sub lattice respectively

[92]. Strong E_2 (high) mode is characteristic of the wurtzite lattice and indicates good crystallinity. The vibrations of A_1 and E_1 modes can polarize in the unit cell, which creates a long-range electrostatic field splitting the polar modes into longitudinal optical (LO) and transverse optical (TO) components. The B_1 modes are Raman and infrared inactive (silent modes).

2.3.5 Scanning Electron Microscopy

A scanning electron microscope (SEM) uses a beam of electrons to image the samples by scanning the surface in a raster scan pattern. SEM is one of the most widely used microscopes in the research community as it is having extremely high magnification, higher resolution, larger depth of focus, and ease of sample observation [93, 94].

Working principle of Scanning Electron Microscopy

A scanning electron microscope uses a beam of electrons for imaging the samples. An SEM consists of the following components: (i) an electron gun, (ii) electromagnetic lens system, (iii) detectors, and (iv) sample holder. The electron gun delivers an intense beam of high-energy electrons. There are two types of electron guns named, thermionic guns and field emission guns. The thermionic gun uses a heated filament for overcoming the work function of the filament material so that the electrons can escape from the material itself. On the other side, the field emission gun uses a large electrical potential gradient across the filament to pull out the electrons. The electron beam follows a vertical path through the column of the microscope. The beam passes through the electromagnetic lenses which focus and direct the beam down towards the sample. Figure 2.16 represents a general schematic of a field emission scanning electron microscope (FESEM) instrument. The high energy electrons after interactions with the samples undergo either inelastic scattering with the atomic electrons or elastic scattering with the

atomic nucleus. As a result of this electron and sample interaction, backscattered electrons (BSEs), secondary electrons (SEs), and characteristics X-rays are produced. Several detectors are used to detect these BSEs, SEs, and X-rays. The secondary electrons make the most detailed image of the surface of an object, while BSEs image can provide atomic number contrast in addition to topographic contrast. X-ray detectors give information on the material composition.

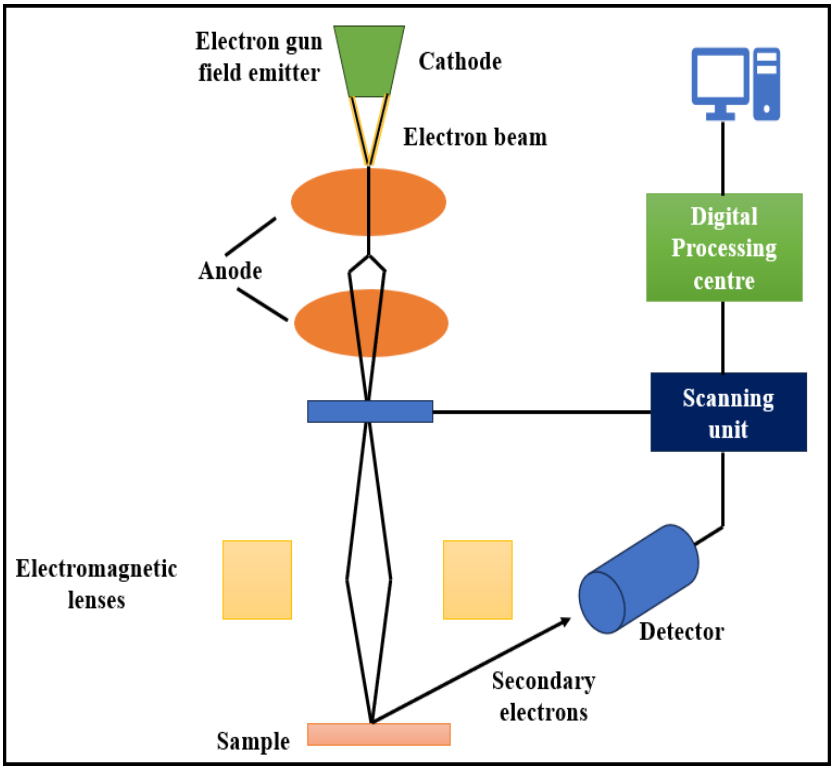

Figure 2.16: General Schematic of the field emission scanning electron microscope (FESEM) instrument.

In this work the surface morphologies of ZnO films were investigated by field emission scanning electron microscopy (FESEM, Zeiss Ultra Plus).

Chapter 3

Thickness dependent optical/electronic properties of metal oxide (ZnO) nanostructured thin films: excitons and effect of disorder

3.1 Outline of work

In this chapter we explore the thickness dependent optical/electronic properties of metal-oxide (zinc oxide, ZnO) nanostructured thin-films. This chapter presents the studies of optical/electronic properties of ALD grown ZnO thin films (ZnO_a) of different thicknesses (ranging from ~5 nm to ~70 nm) with very low surface roughness and bulklike electron density, on selected substrates, fused quartz (SiO_2) as function of film thickness. The studies on excitons and effect of growth mediated disorder have been presented. Photoabsorption (PA) and photoluminescence (PL) measurements were employed for this purpose. Observation of quantum confinement effect (up to a threshold thickness ~20 nm) has been demonstrated and explained consistently with PA and PL studies. The growth mediated internal defects and disorders in the ZnO films has been observed and the to quantify these defects or disorders the Urbach energy is estimated. The consistent trends in the thickness dependent optical properties of the ZnO films as an effect of interface and confinement for ZnO films on SiO_2 was observed. Moreover, an interesting phenomenon involving a non-monotonic change in the optical properties with increase of ZnO film thickness (at above the threshold thickness range) has been explored in details in this chapter. †,‡

†Don P. Benny, Vikas Munya, **Arpan Ghosh**, Ravinder Kumar, Dipayan Pal, Herbert Pfnür, Sudeshna Chattopadhyay. *Journal of Electronic Materials* 52, no.12 (2023):8293-8302.

‡ Prateeksha Rajpoot, **Arpan Ghosh**, Amandeep Kaur, Simran Arora, Mohamed Henini, Subhabrata Dhar, Sudeshna Chattopadhyay. *MRS Bulletin* 49, no. 9 (2024): 885-898.

3.2 Experimental

Atomic layer deposition (ALD) technique has been employed to grow the ZnO thin films on fused quartz substrate of different thicknesses (as discussed in chapter 2). Thickness variation of the ZnO films (~2 nm to ~70 nm) was achieved by varying the number of ALD cycles from 30 to 410. Above 60 cycles we obtained a growth rate of about 1.6 Å per cycle, which is similar with the growth rate reported by other research groups [54, 95]. The nucleation delay which is substrate-dependent during the initial stage of growth process [96-98] was also observed here: after completion of 30 ALD cycles, the film thickness was only 2 nm, i.e., the average initial growth rate per cycle (GPC) was only 0.7 Å/cycle. In the transition range between 30 and 60 cycles the GPC speeds up to 1.6 Å/cycle and remains constant within limits of uncertainty for larger number of ALD cycles [99]. The thickness of the ZnO films was determined by x-ray reflectivity (XRR) as discussed in this chapter. Therefore, the ZnO thin films generally grown by ALD will be named ZnO_a films, whereas for the special case of ALD-grown ZnO thin films on fused quartz, the term ZnO_a/qz will be used.

3.3 XRR analysis for ZnO film thickness on fused quartz (SiO_2) substrate

As discussed in Chapter 2, Section 2.3.1(a), the X-ray reflectivity (XRR) technique provides critical insights into thin films' thickness, electron density profiles (EDPs), and surface and interface roughness.

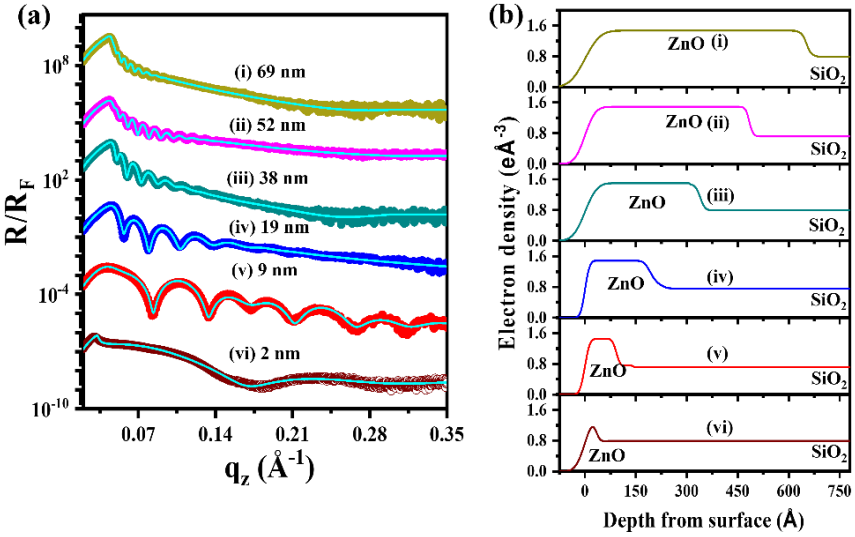

Figure 3.1: (a) Reflectivity profiles, i.e., specular reflectivity (R) normalized with Fresnel reflectivity (R_F), (R/R_F) vs. normal momentum transfer q_z (in $Å^{-1}$) for different ZnO films grown on SiO_2 at 200 ºC process temperature, with film thickness: (i) 69 nm, (ii) 52 nm, (iii) 38 nm, (iv) 19 nm, (v) 9 nm and (vi) 2 nm; R_F is the theoretical reflectivity from an ideal surface. Circles and lines represent the experimental data and theoretical fit respectively. (b) Corresponding extracted electron density (ρ) profile from XRR fits.

Figure 3.1(a) presents the normalized specular reflectivity (R/R_F) data for ZnO films of varying thickness deposited on SiO_2 substrates at 200 ºC. Experimental data, shown as circles, are accompanied by theoretical fits represented by lines, derived using Parratt's exact recursive method [67-71]. The XRR profiles exhibit pronounced Kiessig fringes [29, 30], and the electron density analysis confirms the formation of ZnO thin

films with bulk-like electron density and minimal surface and interface roughness.

Figure 3.1(b) illustrates the corresponding EDPs obtained from XRR fitting. The results indicate that the electron densities of ZnO films grown via atomic layer deposition (ALD) are comparable to bulk ZnO, except for a slight reduction in density observed for films thinner than approximately 10 nm. This behavior suggests the formation of high-quality, pinhole-free ZnO films with nearly complete surface coverage. The ALD-grown ZnO films in this study range in thickness from approximately ~2 nm to ~69 nm. The growth rate, as determined from XRR analysis, was approximately 1.6 Å per cycle at 200 ºC, consistent with previously reported values for ZnO growth via ALD. Film thicknesses, corresponding growth parameters, surface roughness, and other relevant parameters are extracted utilizing the model fitting using Parrat's formalism (discussed in chapter 2) are summarized in some of the works referred [29, 30].

3.4 Optical/electronic properties of ALD grown ZnO

To study the optical properties of ZnO_a/qz, photo absorption (PA) and photoluminescence (PL) techniques have been employed and variation in the spectra with film thicknesses has been discussed here.

3.4.1 Photo absorption (PA) study

Photo absorption spectra of ALD grown ZnO is taken using UV-Vis spectrometer presented below.

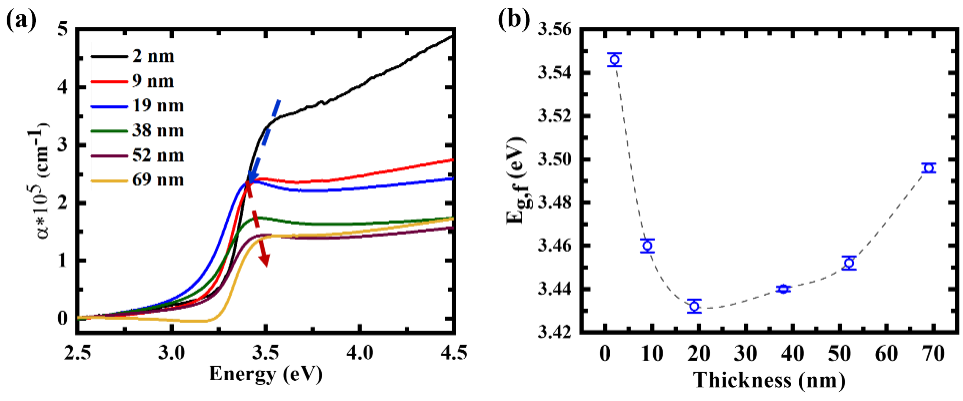

Figure 3.2: UV-Vis absorption spectroscopy of ZnO thin films of varying thicknesses grown on fused quartz (SiO_2) substrates. (a) Plot of absorption coefficient (α) versus photon energy $(h\nu)$. (b) Plot of exciton energy ($E_{g,f}$) versus ZnO_a film thickness.

Figure 3.2(a) illustrates the photo absorption (PA) spectra of ALD-grown ZnO thin films deposited on fused quartz substrates (denoted as ZnO_a/qz). These films exhibit varying thicknesses, specifically ranging from ~2 nm to ~69 nm. Within this spectral data, a notable observation is made regarding the initial behavior of both the leading absorption edge and the excitonic peak ($E_{g,f}$). As the thickness of the ZnO films increases from 2 nm up to approximately 19 nm, these features demonstrate a pronounced excitonic redshift. The redshift behavior reaches a saturation point at a critical thickness of around 19 nm, beyond which the trend does not continue. This observed trend is visually indicated by a blue dashed arrow in Figure 3.2(a). Beyond a film thickness of ~19 nm, there is a noticeable excitonic blueshift in the absorption edge of the ZnO thin films as the thickness further increases from ~38 nm to ~69 nm. This shift signifies an increase in energy and is indicative of changes in the electronic and optical behavior of the material as a function of thickness. These changes in the optical properties are non-monotonic, meaning they do not follow a simple, linear trend. The trend of redshift up to ~19 nm indicated by a blue dashed arrow in Figure 3.2(a) has the corresponding data points of the peak positions presented in Figure 3.2(b). A quantitative analysis of this behavior shows that this increase of wavelength with film thickness, *d*, is compatible with a quantum size effect (see Figure 3.2). Photoluminescence (PL) shows an identical behavior (as demonstrated in the next section 3.4.4). With further increase of *d*; however, we see a blueshift in both PA and PL. The origin of this reversal of shift will be discussed in the next few sections.

Along with this energy shift in the absorption edge and excitonic peak ($E_{g,f}$) it was observed that there is an increase in the absorption coefficient with decreasing film thicknesses. Such increase in absorption coefficient

with decreasing ZnO film thickness on SiO_2 substrate can be explained by the band alignment at the heterojunction at ZnO/SiO_2 interface. The band alignment of ZnO on SiO_2 which is a type-I quantum well consisting of a narrower-bandgap semiconductor grown on a wider-bandgap substrate. In this case, both the electron and the hole are confined in the ZnO film, which leads to an increase in the electron–hole overlap matrix element in thin ZnO films, resulting in higher absorption coefficient at the band edge [29, 30]. In our study, the absorption coefficients for ZnO/SiO_2 samples were estimated from UV-Vis absorption spectra, measured in the transmission mode. With decreasing film thickness, the absorption coefficient of thinner ZnO films (at and below ~20 nm) was found to increases for ZnO/SiO_2 samples [30].
Furthermore, Figure 3.2 exhibits a clear gradual increase in absorption below the threshold peak, which can be effectively characterized as an Urbach tail, corresponding to the disorder developed in the system. We will explain such observed Urbach energy variation with increasing ZnO film thickness in the following sections.

3.4.2 Estimation of the Urbach energy

The Urbach Energy (E_u), or Urbach Edge, is a parameter typically denoted, with dimensions of energy, used to quantify energetic disorder in the band edges of a semiconductor. The parameterization of defects distribution can be done by Urbach energy which are associated with structural and/or thermal disorder. A higher Urbach energy indicates a wider distribution of defects levels in crystal system. The origin of the Urbach tail is usually attributed to structural disorder, phonons, impurities, or excitons which have been reported in various articles [100-103].

In this analysis, we have described that the gradual rise in absorption observed below the threshold peak, as depicted in Figure 3.2, is effectively characterized by the Urbach tail when the near-threshold region is plotted on a semi-logarithmic scale (Figure 3.3). This representation allows for a good approximation of the exponential

dependence of the absorption coefficient (α) on the excitation energy. Such exponential behavior indicates the influence of various disorder mechanisms within the ZnO thin films. Below the excitonic peak, the absorption coefficient (α) can be written in equation **(3.1)** modelled by the Urbach rule (described in section 2.3.2) [104]

$$\alpha = \alpha_0 \exp((h\nu - E_0)/E_u), \qquad \textbf{(3.1)}$$

Where, α_0 and E_0 are characteristic parameters of the material, $h\nu$ is the photon energy, E_u is the Urbach energy, which is related to the energy width of the Urbach tail. The Urbach energy (E_u) was calculated from the inverse slope of the fit of $\ln(\alpha)$ versus $h\nu$, as shown in Figure 3.3.

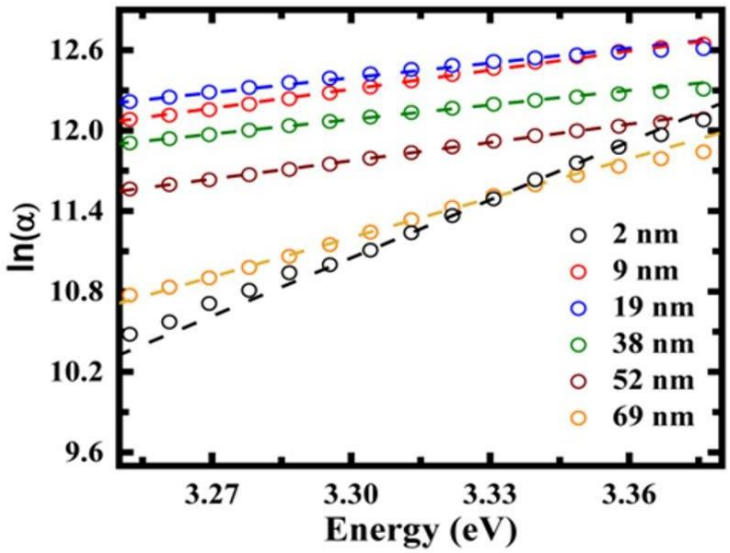

Figure 3.3: Representation of $\ln(\alpha)$ versus energy ($h\nu$) plots below the excitonic threshold to evaluate the Urbach energy E_u of ZnO thin film on quartz substrate.

The data between $\alpha = 27000$ cm^{-1} and $\alpha = 220{,}000$ cm^{-1} were fitted to equation **(3.1)** as the data below 27,000 cm^{-1} were too complex to be included for the analysis, which was also reported in a similar type of data analysis [33, 105].

3.4.3 Variation of the Urbach energy as a function of ZnO film thickness

The variation of Urbach energy (E_u) as a function of ZnO film thickness is depicted in Figure 3.4. The data clearly demonstrates that E_u increases with increasing film thickness of ZnO_a initially, reaching a threshold thickness around 19 nm. At this point, E_u levels off into a plateau up to a thickness of approximately 40 nm. Beyond this thickness, E_u begins to decrease again.

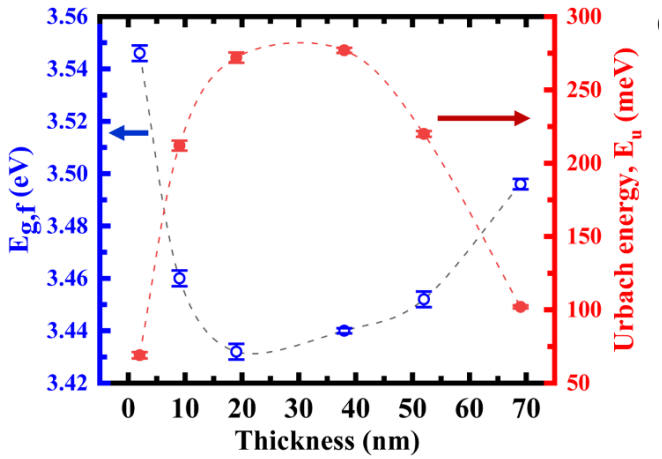

Figure 3.4: Plots of the Urbach energy (E_u) (red filled circles) and the exciton energy or peak in optical absorption ($E_{g,f}$) (blue open circles) of the ZnO_a, as a function of film thickness.

To further understand this phenomenon, we attempted to correlate various properties with the observed behavior of E_u. Specifically, we found a significant correlation between the thickness-dependent variation of E_u and the exciton peak energy ($E_{g,f}$). To illustrate this relationship, $E_{g,f}$ of ZnO_a was plotted as a function of film thickness on the same graph (Figure 3.4). The results indicate a reciprocal relationship between E_u and $E_{g,f}$, which aligns with general observations reported in the literature [33, 103]. For film thicknesses greater than 40 nm, this relationship corresponds to a narrowing of the excitonic

distribution, which is manifested by a decrease in Urbach energy. This behavior suggests that as the film thickness increases beyond 40 nm, there is a reduction in the density of defect states, leading to a more ordered electronic structure. This trend continues until we approach a film thickness of approximately 70 nm, at which point the properties of the ZnO films closely resemble those of bulk ZnO. This indicates that the films are reaching bulk-like excitonic excitation.

Furthermore, we have also estimated the optical bandgap ($E_{g,e}$) of the direct bandgap semiconductor ZnO thin films was determined using the Tauc model [1], focusing on the high absorbance region. The Figure 3.5 presents a plot of $(\alpha h\nu)^2$ versus $h\nu$.

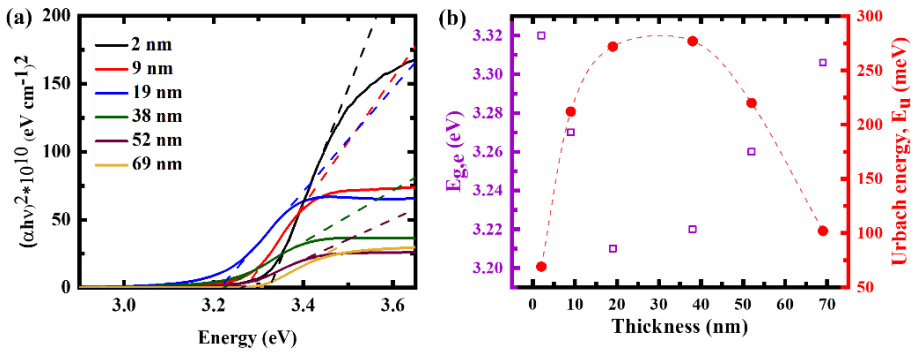

Figure 3.5 : UV-Vis absorption spectroscopy of ZnO thin films of varying thicknesses grown on polished fused quartz (SiO_2) substrates (ZnO_a/qz): (a) Plot of $(\alpha h\nu)^2$ vs. photon energy ($h\nu$), where α is the absorption coefficient. The optical bandgap, $E_{g,e}$, value can be obtained by extrapolating the linear portion to the photon energy axis, using the equation (2.18) of chapter 2 in manuscript, where the value of n is 1/2 for allowed direct transition; (b) Plots of the Urbach energy (E_u) (red filled circle) and optical bandgap ($\nu_{g,e}$) (purple open square) of the ZnO_a as a function of film thickness; The dotted straight line is the eye guided line.

From the Figure 3.5 we can see that as the film thickness decreases, the $E_{g,e}$ initially reduces until it reaches a threshold thickness of approximately 19 nm, below which the $E_{g,e}$ increases with further decreasing thickness. This trend parallels the variation observed in the excitonic peak energy, $E_{g,f,}$ (see Figure 3.4) as a function of ZnO film thickness. Such congruence between the behaviors of $E_{g,e}$ and $E_{g,f}$ aligns with the general observations reported under Figure 3.6.

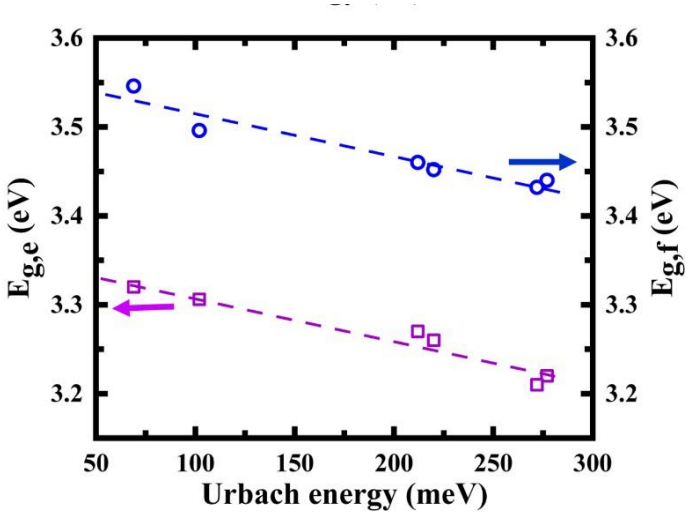

Figure 3.6: Plots of the exciton energy ($E_{g,f}$) (blue open circles) and the optical band gap ($E_{g,e}$) (red filled circles) versus the Urbach energy (E_u). The dotted straight lines are guides to the eye.

Figure 3.6 illustrates that the peak in optical absorption, designated as ($E_{g,f}$), exhibits a dependence on film thickness that is consistent with the variation in the photo-absorption edge or optical bandgap ($E_{g,e}$). The separation between the values of ($E_{g,f}$) and ($E_{g,e}$) is approximately 0.2 eV. To reconfirm these non-monotonic changes in the optical properties of ALD grown ZnO thin film on SiO_2 with the film thickness extracted from PA, we have performed PL study.

3.4.4 Photoluminescence (PL) study

Figure 3.7 presents the PL spectra of ALD-grown ZnO thin films (ZnO_a). The inset provides a log scale representation for better clarity. These PL spectra have been accurately fitted using four Gaussian peaks, as detailed in Figure 3.7 and Table 3.1.

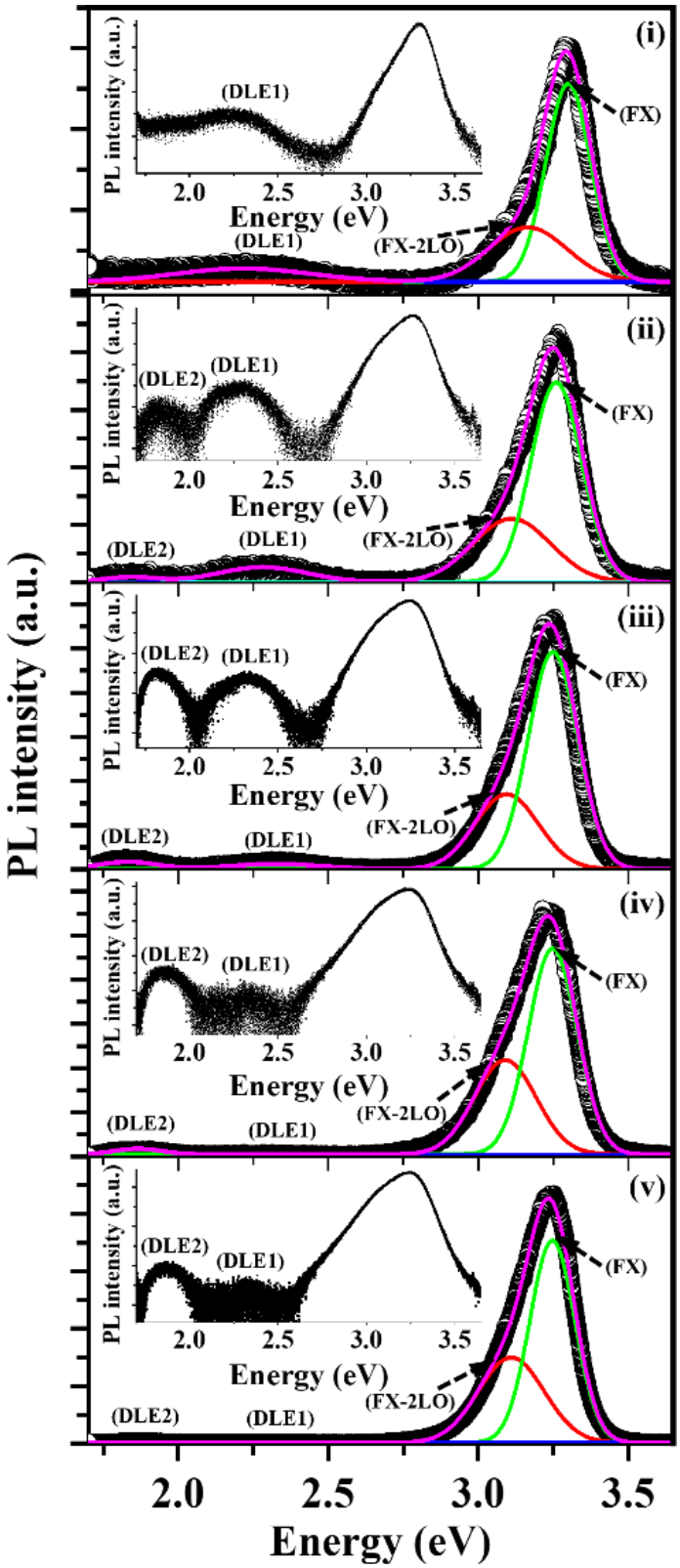

Figure 3.7: Room temperature PL spectra of ZnO thin films (ZnO_a) for thicknesses of (i) 9 nm (ii) 19 nm (iii) 38 nm (iv) 52 nm and (v) 69 nm.

The spectra are normalized with respect to the UV peak. The PL spectra show near band (NBE) and defect level emissions (DLE). Insets show the corresponding PL spectra in log scale to display the weak DLE components clearly. The contributions from FX and FX-2LO to NBE and the contribution of green (DLE1) and red emissions (DLE2) to DLE were extracted by Gaussian fits of the PL spectra. The combined effects of the four Gaussians are indicated by the pink solid curves. Circles: experimental data.

The spectra reveal distinct peaks corresponding to near-band emission (NBE) and defect level emission (DLE). The NBE peaks, which appear in the ultraviolet (UV) region, are predominantly attributed to the free exciton (FX) emissions. Additionally, a shoulder peak corresponding to the second-order longitudinal optical phonon replica (FX-2LO) is observed adjacent to the main FX peak. In the visible region, DLE peaks are clearly distinguishable, indicating the presence of defect-related states within the ZnO films [106-109]. The observation of both NBE and DLE emissions underscores the role of excitonic and defect-related processes in determining the optical behavior of ZnO films, which is critical for optimizing their performance in optoelectronic applications. The observed separation between the FX peak and its FX-2LO is approximately twice the phonon energy values documented in the literature, which range from 72 to 76 meV [33, 107, 110]. The presence of the FX-2LO peak, rather than the first-order longitudinal optical phonon replica (FX-1LO), is indicative of oriented crystal growth along the C-axis and high crystal quality. This is because FX-1LO transitions are forbidden in perfect crystals due to parity conservation principles [106, 111]. In addition to the prominent NBE, the PL spectra also exhibit defect level emissions DLE corresponding to various defect states within the sub-bandgap region of the semiconductor. These defect emissions are labeled as DLE1 and DLE2 in Figure 3.7. The emission peak at 2.25 eV, designated as DLE1, is attributed to defects related to oxygen vacancies (V_O) within the ZnO thin films. This emission, commonly referred to as green emission, becomes more pronounced in thinner films due to the

increased influence of surface states and defect levels. Such oxygen vacancies in ZnO creates localized states within the band gap, which facilitate radiative recombination processes resulting in visible light emission [106, 109, 112-114].

The emission peak at ~ 1.85 eV is attributed to DEL2, which is related to zinc interstitials (Zn_i). It has been observed that initially with increasing film thickness the DLE2 become more prominent up to the threshold thickness. After this threshold thickness the intensity of these DLE2 starts to decrease. Since this intensity is proportional to the concentration of Zn interstitials, it seems that the Zn interstitials are the main source of disorder.

Along with these two DLE emission peaks the positions of the FX and FX-2LO, determined through the deconvolution of the NBE emission, are presented in Table 3.1. While the excitation of LO phonons itself is relatively unaffected by structural disorder, the intensity of the FX-2LO is notably more sensitive to such disorder.

Towards the estimation or quantification of the defects or disorders and their thickness dependency in such ZnO_a systems, we extracted the relevant parameters (I_{FX}, $I_{FX\text{-}2LO}$, I_{DLE1}, I_{DLE2}, I_{NBE}) from Figure 3.7, and plot those in Figure 3.8 along with the Urbach energy (E_u).

Table 3.1: Photoluminescence (PL) study ZnO_a thin films (The positions of FX and FX-2LO obtained after the deconvolution of NBE.)

Thickness (nm)	Near band edge emission (NBE)				I_{FX-2LO}/I_{NBE}	I_{FX-2LO}/I_{FX}	Deep level emission (DLE)				I_{DLE}/I_{NBE}
	FX		FX-2LO				DLE1		DLE2		
	Energy (eV)	FWHM (eV)	Energy (eV)	FWHM (eV)			Energy (eV)	I_{DLE1}/I_{NBE}	Energy (eV)	I_{DLE2}/I_{NBE}	
9	3.3	0.15	3.165	0.26	0.36	0.56	2.22	0.14	-	-	0.14
19	3.26	0.17	3.11	0.26	0.327	0.49	2.28	0.09	1.84	0.018	0.108
38	3.249	0.16	3.095	0.21	0.306	0.44	2.32	0.03	1.83	0.028	0.058
52	3.248	0.19	3.09	0.24	0.367	0.58	-	-	1.86	0.017	0.017
69	3.247	0.15	3.11	0.22	0.382	0.62	-	-	1.87	0.002	0.002

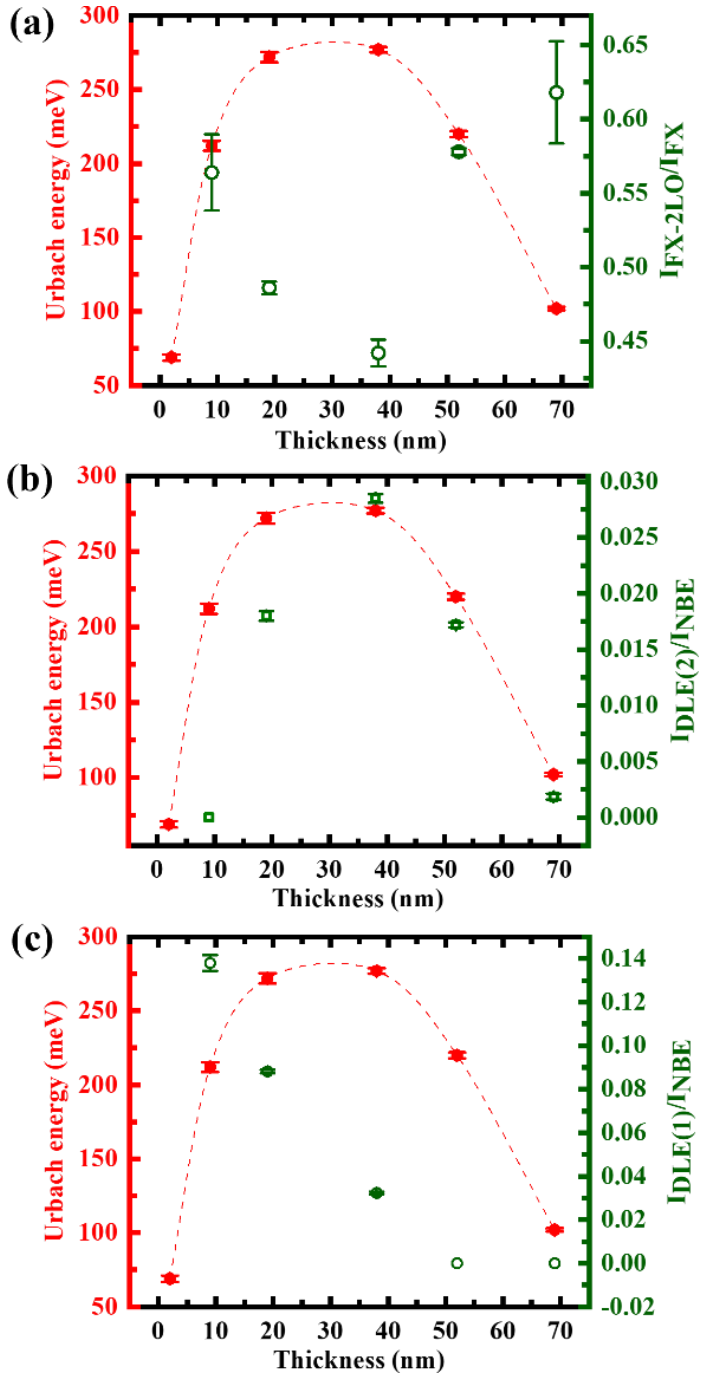

Figure 3.8: Plot of (a) Urbach energy (filled circles) and I_{FX-2LO}/I_{FX} (open circles) versus thickness. (b) Urbach energy (filled circles) and I_{DLE2}/I_{NBE} (open squares) versus thickness. (c) Urbach energy (filled circles) and I_{DLE1}/I_{NBE} (open stars) versus thickness. Urbach energy was estimated from UV-Vis spectroscopy, whereas I_{FX}, I_{FX-2LO}, I_{NBE}, I_{DLE1} and I_{DLE2} were estimated from photoluminescence (PL) study.

In Figure 3.8(a), the sensitivity of FX-2LO for defects, is depicted through a clear anti-correlation between the intensity of the FX-2LO peak and the degree of disorder within the ZnO thin films, as quantified by the Urbach energy. As the disorder increases, the intensity of the FX-2LO peak diminishes. The peaks in Urbach energy and the corresponding minimum intensity of the FX-2LO peak collectively indicate a concentration build-up of defects as the film thickness varies. This relationship suggests that defect concentration reaches its broad maximum within the thickness range of approximately 20 to 40 nm. These defects further analyzed by examining the thickness-dependent variation of the defect level emissions DLE1 and DLE2.

The concentration of defects associated with DLE2, which corresponds to zinc interstitials, was quantified by calculating the ratio of the integrated defect emission intensity (I_{DLE2}) to the near-band-edge emission intensity (I_{NBE}), presented in figure 3.8(b). This ratio provides a measure of the relative defect concentration. Analysis of the thickness dependence of Urbach energy revealed a trend that closely follows the variation in the intensity of DLE2, as depicted in Figure 3.8(b).

Conversely, the structural disorder within the ZnO thin films is evidently not directly associated with oxygen vacancies, as indicated by the behavior of DLE1. As shown in Figure 3.8(c), the intensity of the DLE1 emission decreases monotonically with increasing film thickness, eventually reaching the detection limit for films thicker than 50 nm. This trend suggests that the concentration of oxygen vacancies diminishes as the film thickness increases. This observed behavior implies that oxygen vacancies are predominantly situated at the surface of individual grains within the ZnO films. As the film thickness increases, the grain size correspondingly enlarges, leading to a reduction in the relative surface area where these vacancies can reside. Consequently, the concentration of oxygen vacancies becomes less significant in thicker films, explaining the monotonic decrease in DLE1 intensity.

Based on the observed results, it is highly probable (as illustrated in Figure 3.5) that the increase in Urbach energy is primarily driven by the escalating concentration of zinc interstitials (Zn_i) with increasing film thickness up to approximately 20 nm. As these interstitial defects accumulate, they degrade the crystalline quality of the films, which is evidenced by the corresponding decline in the intensity of the FX-2LO. The FX-2LO peak's reduced intensity within this thickness range aligns with the assumption that an increased defect concentration hampers the crystallinity and ordered structure of the material.

As we know that the energy gap estimated from UV-Visible spectroscopy results, using the Tauc plot (as described in figure 3.5), does not directly provide the precise band gap values. Instead, it indicates the onset of the absorption edge that is influenced by the Urbach effect in the low energy region. So, in addition, PL results were utilized to derive a more accurate estimation of the band gap of ZnO thin films (details are below in 3.4.5 section).

3.4.5 Confinement effect/Quantum size effect in ZnO_a films: bandgap variation from PL studies

The estimation of bandgap energy, $E_{g,PL}$, is based on the position of the FX peak. The band gap energy of ZnO thin films was calculated by summing the FX peak energy with its binding energy (i.e., exciton binding energy), which is 60 meV, as referenced in the literature [82]. The behavior of the bandgap energy, $E_{g,PL}$, in relation to the thickness of ZnO layers below the threshold can be determined by analyzing the free exciton peak observed in the PL spectra. When plotting the peak energy of $E_{g,PL}$ against the inverse square of the layer thickness ($1/d^2$) for data up to 19 nm, as shown in Figure 3.9, the increase in $E_{g,PL}$ follows a linear trend. This linear relationship indicates that the increase in $E_{g,PL}$ with decreasing film thickness can be attributed to the quantum size effect,

where electron confinement within the thin ZnO layers becomes significant.

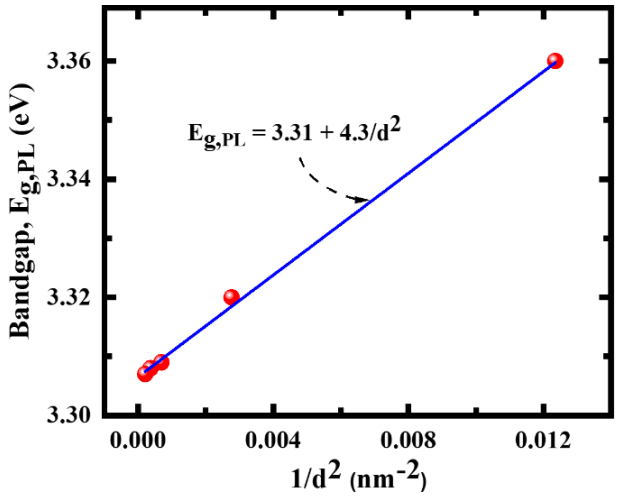

Figure 3.9: Confinement effect in ZnO_a films. Bandgap energy ($E_{g,\,PL}$) versus $1/d^2$ plot, where d is the film thickness: circles and lines represent experimental data and theoretical fit, respectively.

According to the effective mass approximation (EMA) theory, $E_{g,PL}$ of nanostructures with size d can be determined using the following mathematical expression [115] **(3.2)**,

$$E_{g,PL} = E_{g,bulk} + F/d^2 \qquad \textbf{(3.2)}$$

where $E_{g,bulk}$, is the bandgap value of the bulk ZnO crystal, and F is the quantum confinement constant, were found to be 3.31 eV and 4.3 eV-nm^2 respectively, which were quite consistent with the respective values reported in the different literatures [29].

This analysis reveals the existence of two distinct growth regimes in ZnO thin films based on their thickness. For films with thicknesses below 20 nm, the layers are essentially homogeneous and act as confined environments, restricting electron movement to within the specific layer thickness. This confinement effect is characteristic of quantum size effects, where the thin layers maintain uniformity and continuous electronic properties across the entire film. In contrast, as the film thickness exceeds 20 nm, the layers begin to exhibit grain formation. In

these thicker films, the material is no longer a continuous homogeneous layer but rather composed of individual grains or crystallites.

3.5 Summary

In this chapter, studies of optical/electronic properties of ALD grown ZnO thin films (ZnO_a) as function of film thickness were conducted via photoabsorption (PA) and photoluminescence (PL). A non-monotonic change in the optical properties with variation of ZnO film thickness was observed. The PA studies demonstrates, the red shift in exciton energy (i.e., peak in optical absorption ($E_{g,f}$)) with the increasing ZnO_a film thickness (d) in the range of ~2 nm to ~19 nm, indicates the quantum size effect. The quantum confinement effect has been also clearly evident from PL study. The quantum size effect at film thickness d up to 20 nm follows the expected $1/d^2$ dependence on film thickness and indicates the existence of a homogeneous film. Simultaneously, the Urbach energy (E_u) or disorder, as extracted from the PA studies, increases with increasing ZnO_a film thickness in the first stage until a threshold film thickness at around 19 nm is reached, followed by a plateau up to d = 40 nm, above which it starts to decrease again. Peak in optical absorption ($E_{g,f}$) and photoabsorption edge or optical bandgap ($E_{g,e}$) have same dependence on film thickness with their corresponding values separated by 0.2 eV. Urbach energy (E_u) anti-correlates with the excitonic energy or peak position in optical absorption ($E_{g,f}$) and with optical bandgap ($E_{g,e}$). Detailed PL studies demonstrate the presence of two different types of defects levels, oxygen vacancy (DLE1, concentration increases with film thickness) and Zn interstitial (DLE2, show non-monotonic trend with film thickness) in these systems.

(In next chapter, the scientific reason for the origin of the observed phenomenon in chapter 3 has been explored.)

Chapter 4
Self-healing of defect mediated disorder in ZnO thin films

4.1 Outline

In this chapter, the origin of the observed non-monotonic change in the optical properties of ZnO with increasing film thickness (as demonstrated in Chapter 3) has been explored. Identification of the phenomena involving self-healing of defect mediated disorder in ZnO thin films, has been discussed in this chapter. For this purpose, the structure and morphology of the ZnO films of different thicknesses were studied elaborately via conducting XRD and FESEM. The results from FESEM and XRD, in combination with PL study, were utilized to explain the observed phenomena of spontaneous decrease of disorder (i.e., the non-monotonic variation in optical/electronic properties, as mentioned in chapter 3) as a function of ZnO film thickness (*d)*, above a threshold thickness of about ~20 nm. Along with this, from an analysis of the XRD pattern, which estimates the strain along the surface normal (c-axis) and, coupled to it, the in-plane compressive stress in ZnO_a films. The results signify the occurrence of change of growth mode from an essentially smooth to a grainy structure, at around threshold thickness, and relates it to a mechanism of self-healing process of defect mediated (Zn interstitial) disorder in ZnO thin films. from an analysis of the x-ray diffraction (XRD) pattern, which estimates the strain along the surface normal (c-axis) and, coupled to it, the in-plane compressive stress in ZnO_a films. †,‡

†Don P. Benny, Vikas Munya, **Arpan Ghosh**, Ravinder Kumar, Dipayan Pal, Herbert Pfnür, Sudeshna Chattopadhyay. *Journal of Electronic Materials* 52, no.12 (2023):8293-8302.

‡ Prateeksha Rajpoot, **Arpan Ghosh**, Amandeep Kaur, Simran Arora, Mohamed Henini, Subhabrata Dhar, Sudeshna Chattopadhyay. *MRS Bulletin* 49, no. 9 (2024): 885-898.

4.2 Structural/morphological analysis of ALD ZnO: Study of Growth Modes

The structural and morphological analysis or ALD grown ZnO films has been performed using field emission scanning electron microscopy (FESEM) and X-ray diffraction (XRD) techniques, which have been discussed here.

4.2.1 Morphological analysis: FESEM

The variation in the morphology and growth mode of the ALD grown ZnO are evident from the FESEM images of thin film with different thickness presented in figure 4.1.

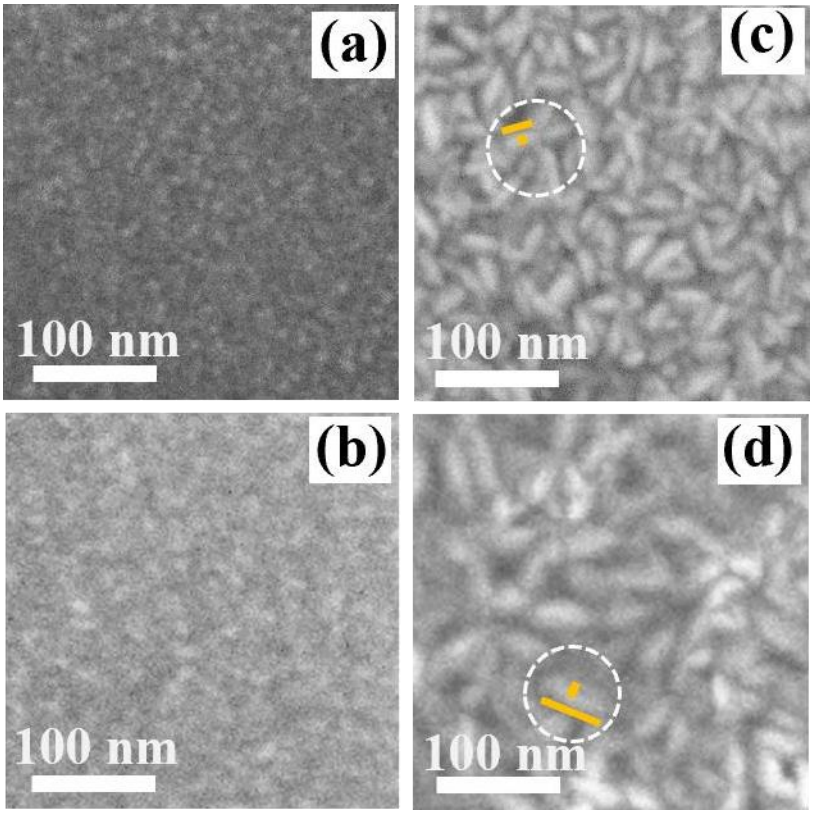

Figure 4.1: Top-view SEM images of ZnO thin films on fused quartz (ZnO_a/qz) of characteristic film thicknesses: (a) 9 nm, (b) 19 nm, (c) 38 nm, and (d) 69 nm. The average in-plane grain sizes (major and minor axes) for 38 nm and 69 nm thick samples are shown within the dotted circles.

4.2.1.1 Observations

The FESEM images presented in Figure 4.1 clearly illustrate the morphological evolution of ZnO thin films as a function of film thickness. The change of growth mode is evident from the FESEM shown in Figure 4.1. For film thicknesses up to 20 nm, as shown in Figures 4.1(a) and 4.1(b), the ZnO films are characterized by dense, nanocrystalline, and smooth surfaces. This suggests a homogeneous layer formation with high crystallinity and minimal surface roughness, indicative of high-quality thin films in this thickness range.

In contrast, ZnO films with higher thicknesses display a distinct transition to a grainy morphology. This change is more evident in thicker films, exemplified by the FESEM images for 38 nm and 69 nm thick films in Figures 4.1(c) and 4.1(d), respectively. The images reveal that the grain size increases with increasing film thickness, indicating a shift from a nanocrystalline structure to a polycrystalline one with larger grain dimensions.

For the 69 nm thick ZnO film, the grains exhibit an elongated shape with average in-plane dimensions of approximately 51 nm and 13 nm, respectively. Similarly, for the 38 nm thick film, the average in-plane dimensions are approximately 26 nm and 8 nm, respectively. This gradual increase in grain size with thickness suggests that thicker films undergo a process of grain growth and coalescence, resulting in a more pronounced polycrystalline morphology.

4.2.1.2 Correlation of growth mode with PA and PL results

The transition in growth mode from a nanocrystalline structure to a grainy morphology for ZnO films with thicknesses greater than 20 nm is closely associated with several key optical and structural changes. As the film thickness increases beyond 20 nm, the Urbach energy (E_u) reaches a saturation point, as shown in Figures 4.1(b) and 3.8. This saturation indicates a plateau in the degree of structural disorder and defect density within the material.

Simultaneously, this change in growth mode corresponds with the observed minimum in excitonic peak energy ($E_{g,f}$), as depicted in Figure 3.4. The minimum $E_{g,f}$ signifies a critical thickness at which the quantum confinement effects and structural disorder are balanced, resulting in the lowest energy state for excitonic transitions.

Additionally, the formation of anisotropic crystallites, which are tens of nanometers in size, is observed in this thickness range. These crystallites' appearance is linked to the minimal intensity of the FX-2LO phonon replica peak, which reflects the sensitivity of phonon-exciton interactions to structural disorder. As the layer thickness continues to increase, these crystallites grow larger, leading to the recovery of FX-2LO intensity (shown in Figure 3.8). This recovery suggests an improvement in crystal quality and a reduction in defect states as the grains coalesce and grow.

The increasing concentration of zinc interstitials (Zn_i) in ZnO thin films with thicknesses up to 20 nm significantly contributes to the overall structural disorder of the material. This disorder predominantly manifests along the out-of-plane direction [116, 117].

The observed structural and chemical disorder within ZnO thin films leads to a destabilization of the initial growth mode once a critical concentration of defects is reached. This phenomenon has been widely reported in the literature for various thin film growth techniques [107, 118, 119]. The change in growth mode also appears to influence the energetics of vacancy formation within the material.

As evidenced by Figure 3.7, the defect level emission DLE2, associated with zinc interstitials, shows saturation and subsequent reduction with increasing film thickness beyond a certain transition point. This suggests that the formation of Zn interstitials becomes increasingly unfavourable as the film thickness (d) increases. Given that d is directly related to the average crystallite size, it can be inferred that the concentration of these interstitial defects *spontaneously* decreases as the crystallites grow larger and begin to exhibit more bulk-like properties. This behavior indicates

the presence of a self-healing mechanism for Zn interstitials, where the defects are naturally reduced as the material approaches bulk characteristics.

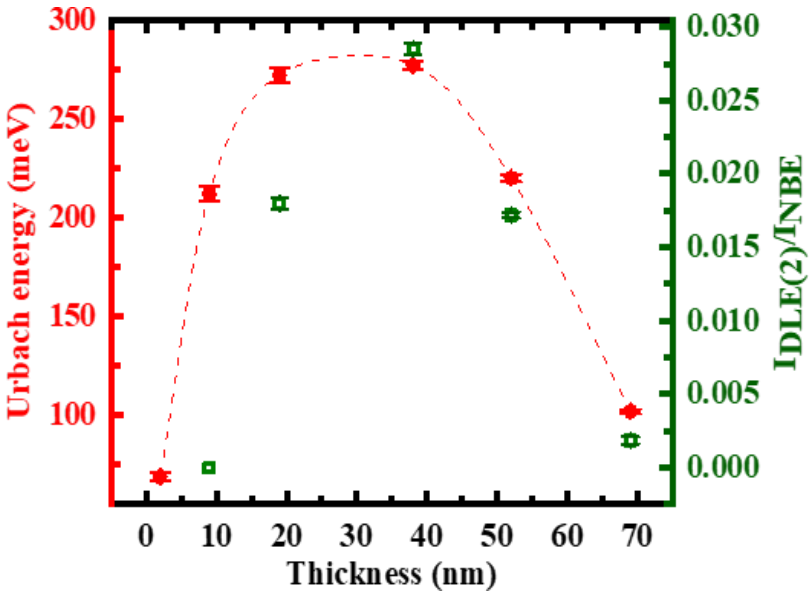

Figure 4.2: Plot of Urbach energy (filled circles) (as estimated from UV-Vis spectroscopy) and I_{DLE2}/I_{NBE} (open squares) (as estimated from photoluminescence study) versus thickness.

Correspondingly, the Urbach energy (E_u), which measures the degree of structural disorder, decreases with increasing film thickness. This decrease is consistent with the reduction in Zn interstitial concentration. The primary mechanism proposed for the *spontaneous* annihilation of Zn interstitials involves the diffusion of Zn atoms to the surface of ZnO crystalline grains, where they undergo oxidation. This diffusion and oxidation process effectively eliminates the interstitial defects, thereby improving the crystalline quality and reducing structural disorder within the film.

In addition to the points previously outlined in FESEM, there are further two more observations that reinforce the scenario we're emphasizing, (i) derived from XRD analysis, (ii) derived from PL analysis. These observations provide compelling evidence that supports the proposed

mechanism and highlights the detailed structural changes occurring within the ZnO thin films, further validating the conclusions drawn from the FESEM data.

4.2.2 X-ray diffraction (XRD) of ALD ZnO: Stress/strain analysis

The X-ray diffraction (XRD) analysis confirms that the ZnO thin films exhibit a hexagonal wurtzite crystal structure, corresponding to the space group P63mc. This crystallographic orientation aligns with the standard diffraction pattern for hexagonal wurtzite ZnO, as referenced in the JCPDS PDF card number 01-079-2205.

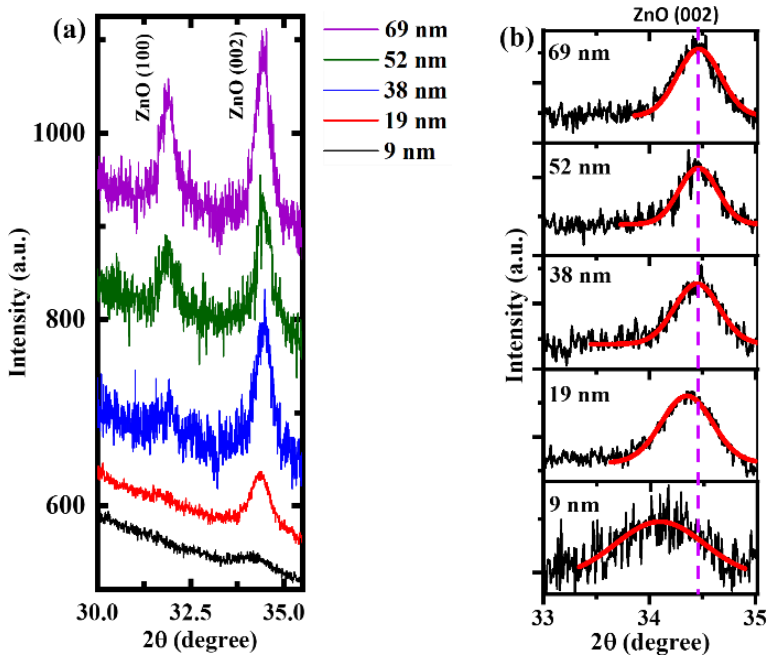

Figure 4.3: (a)-(b): X-ray diffraction pattern of ZnO ultrathin films of varying thicknesses (9 nm to 69 nm) grown on fused quartz (SiO_2) substrates (ZnO_a/qz). (b) is the zoomed portion of (a).

In our XRD measurements, the ZnO films show a notably strong ZnO (002) diffraction peak, whereas the ZnO (101) peak is very weak or almost vanishing (see Figure 4.3). In contrast, standard XRD patterns for bulk hexagonal wurtzite ZnO typically display maximum intensity at the ZnO (101) peak, as indicated by the same JCPDS PDF card number 01-

079-2205 reference. This discrepancy suggests that our ZnO films are preferentially oriented along the (0002) direction, with the c-axis perpendicular to the substrate surface. This preferred orientation is indicative of high-quality crystalline alignment in the thin films. The full width at half maximum (FWHM) of the most intense XRD peak, specifically the (002) peak, is a crucial parameter for determining the crystallite size of ZnO thin films. Using Scherrer's formula, which relates the FWHM of a diffraction peak to the average size of crystalline domains, we can estimate the out-of-plane mean grain size of the ZnO films. For thicker ZnO films, with thicknesses ranging from 38 nm to 69 nm, the average out-of-plane domain size, also referred to as the mean crystallite size, is approximately 20 nm. This suggests that the crystallites in these thicker films are relatively large and well-defined, contributing to the overall crystalline quality of the material. In contrast, for thinner ZnO films with thicknesses at or below 19 nm, the out-of-plane domain size decreases in proportion to the film thickness. This indicates that the crystallite size becomes smaller as the film thickness decreases, these observations are summarized in Table 4.1.

Table 4.1: Out-of-plane average domain size (mean crystallite size) for ALD grown ZnO thin films onto polished fused quartz (amorphous SiO_2) substrates, i.e., ZnO_a films.

ZnO film thickness (from XRR) (nm)	**ZnO (002) peak (from XRD)**		
	Peak position (2θ) (Degree)	**FWHM (Degree)**	**Out of plane domain Size (nm)**
9	34.10	0.92	9
19	34.34	0.48	18
38	34.45	0.42	20
52	34.46	0.36	23
69	34.47	0.41	20

Additionally, a notable shift in the ZnO (002) peak towards lower 2θ angles is observed as a function of increasing film thickness. This peak shift becomes particularly significant at and below the threshold thickness of approximately 19 nm, as shown in Figure 4.3(b). The shift towards lower angles is likely due to strain effects or lattice parameter variations associated with film thickness, reflecting changes in the structural properties as the films transition from thinner to thicker regimes. The variation of in-plane compressive stress in ZnO_a films with increasing film thickness, which may cause the observed variation in surface morphology in FESEM.

The out-of-plane (along the c-axis), layer spacing, also known as the lattice parameter *c*, of ZnO thin films (ZnO_a) was determined by analyzing the ZnO (002) diffraction. To calculate the lattice parameter c, Bragg's law was employed (see eq. 4.1).

$$c = \frac{\lambda}{\sin\theta} \quad \textbf{(4.1)}$$

The observed increase in the lattice parameter *c* for ZnO thin films at and below the threshold thickness, in comparison to thicker films and unstrained ZnO thin films (c_0), indicates a significant variation in structural parameters with film thickness. Specifically, the c values range from 5.20 Å to 5.26 Å, which suggests that as the film thickness decreases, the lattice parameter c tends to increase. This increase in the lattice parameter cc introduces compressive stress along the in-plane direction of the ZnO thin films. The compressive stress arises because the atoms in the crystal lattice are forced into closer proximity, leading to a distortion of the crystal structure. This distortion is more pronounced in thinner films due to the limited volume available to accommodate the lattice expansion.

Having discussed the in-plane compressive stress within the crystal structure, we will now proceed to estimate the strain present in the crystal lattice. Now, the strain (ε) of ZnO thin films along the c-axis

perpendicular to the substrate is defined as [120] written in equation **(4.2)**,

$$\varepsilon = \frac{c - c_0}{c_0} \quad \textbf{(4.2)}$$

c is the lattice parameter of the thin film calculated from XRD peak ZnO (002) and c_0 is the lattice parameter of the unstrained ZnO thin film, 5.206 Å [118]. Residual stress (σ) within the plane of hexagonal thin film systems can be determined by utilizing equation (4.3) alongside the biaxial strain model. [120],

$$\sigma = [2C_{13} - \frac{C_{33}(C_{12}+C_{11})}{C_{13}}]\,\varepsilon \quad \textbf{(4.3)}$$

Where, C_{ij} are the elastic stiffness constants of the ZnO single crystal (C_{11}=208.8 GPa, C_{33}=213.8 GPa, C_{12}=119.7 GPa, C_{13}=104.2 GPa).

The analysis reveals that compressive in-plane stress arises in ZnO thin films when their thickness is below a certain threshold. This threshold thickness, which is identified to be between 19 nm and 38 nm, is critical for the development of compressive stress within the films. As illustrated in Figure 4.4, the dotted horizontal line represents the point of zero in-plane compression. This line indicates that the threshold thickness value is approximately 23 nm. This value is consistent with the out-of-plane average domain size (mean crystallite size) of ZnO films that exhibit no stress, which corresponds to the thicker ZnO films with thicknesses ranging from 38 nm to 69 nm.

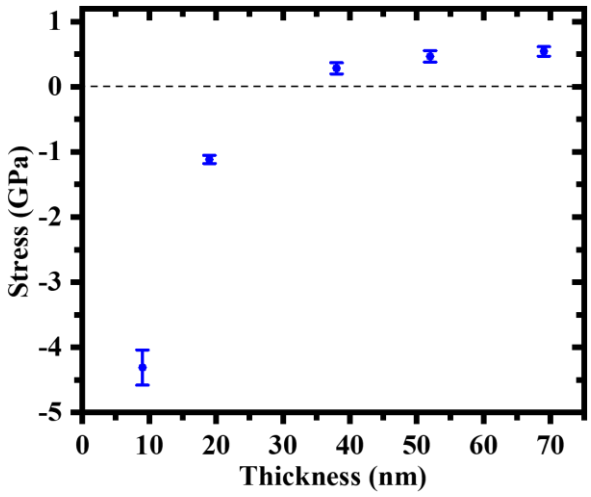

Figure 4.4: Plot of the evolution of in-plane stress in ZnO_a films with decreasing film thickness.

It is important to note that the compressive stress observed in thinner ZnO films primarily originates from extrinsic factors. These factors include lattice mismatch or differences in the thermal expansion coefficients between the film and the substrate. In the case of our ZnO films, which are deposited on an amorphous SiO_2 substrate (polished fused quartz), the compressive stress resulting from lattice mismatch is relatively small [121]. Nevertheless, as the in-plane compressive stress increases in thinner films—specifically those at or below the threshold thickness—there is a noticeable increase in the bandgap energy. This phenomenon has been observed in prior studies, where an increase in bandgap was correlated with rising in-plane compressive stress [107].

From these XRD analysis, results suggests that the change of growth mode to mesoscopic crystallites is coupled with an almost complete relaxation of the in-plane compressive stress [107], as expected.

The second supporting observation of FESEM results, is the behavior of the bandgap energy, $E_{g,PL}$, as a function of layer thickness for layers below the threshold, which was determined by the free exciton peak from the PL (The detail about this effect has already been discussed in chapter 3 under section 3.4.5 in Figure 3.9). This analysis also shows that there are two separate growth regimes, with the thin layers below 20 nm acting as essentially homogeneous layers that restrict the electrons to the layer of a given thickness, while the thicker layer is split up into grains.

4.3 Summary

In this chapter, origin of the observed non-monotonic change in the optical properties of ZnO with increasing film thickness has been explored. Identification of the phenomena involving self-healing of defect mediated disorder in ZnO thin films, has been discussed. The change of growth mode of thin film is evident from the FESEM. Dense nanocrystalline and smooth ZnO films are formed for film thicknesses up to 20 nm. On the other hand, ZnO films with a higher thickness exhibit a grainy morphology, with an increasing grain size as a function of increasing film thickness. The change of growth mode from the nanocrystalline to the grainy structure for ZnO film thickness, correlates with the saturation of the Urbach energy (E_u) as a function of film thickness, as well as with the minimum of exciton peak energy ($E_{g,f}$). The results imply that the concentration of these interstitials is *spontaneously* reduced for crystallites that approach more and more bulk properties, i.e., there is a mechanism of self-healing for these interstitial defects. Furthermore, the XRD pattern, estimated values of strain (along the surface normal) and the in-plane compressive stress were suggesting that the change of growth mode to mesoscopic crystallites is coupled with an almost complete relaxation of the in-plane compressive stress, correlates to the change in growth mode of the films.

Chapter 5

Effect of metal doping in nanostructured ZnO: Structural and electronic properties

5.1 Outline of work

In this chapter, we explore the effect of concentration of metal doping to introduce the extrinsic defects in nanostructured ZnO systems towards the controlled variation in structural and electronic properties [122] [123]. We examine the defect induced structural configuration and corresponding electronic properties. Here specifically, we explore the defect mediated structural changes in ZnO nanoparticles due to different concentration of nickel (Ni) metal doping [124, 125]. For this study, different sets of Ni-dopped ZnO nanoparticle systems were synthesized by sol-gel method, with varying doping concentration from 0 (i.e., pure ZnO nanoparticles) to 10 molar percent. The structural properties in Ni doped ZnO was investigated by employing X-ray diffraction (XRD) technique. X-ray diffraction (XRD) technique and Raman spectroscopy were employed to investigate the to investigate the structural/configurational/electronic changes in ZnO nanostructure due to the extrinsic defects generated by different concentration of Ni-doping [126, 127]. Finally, to explore whether these external doping mediated variation in structural configuration/ defects for such Ni doped ZnO nanostructures can exhibit any effect in their application in terms of their applications involving their structural, thus electronic properties, we carried out experiments with photocatalytic activity measurements, which has been presented in this chapter.

5.2 Experimental

Nickel (Ni) doped ZnO nanostructure was synthesized by Sol-gel technique with different doping concentration ranging from (0 mol% to 10 mol%) have been studied to explore the effects of metal doping on structural and electronic properties of ZnO. The detailed synthesis process Sol-gel technique is already elaborated in Chapter 2.

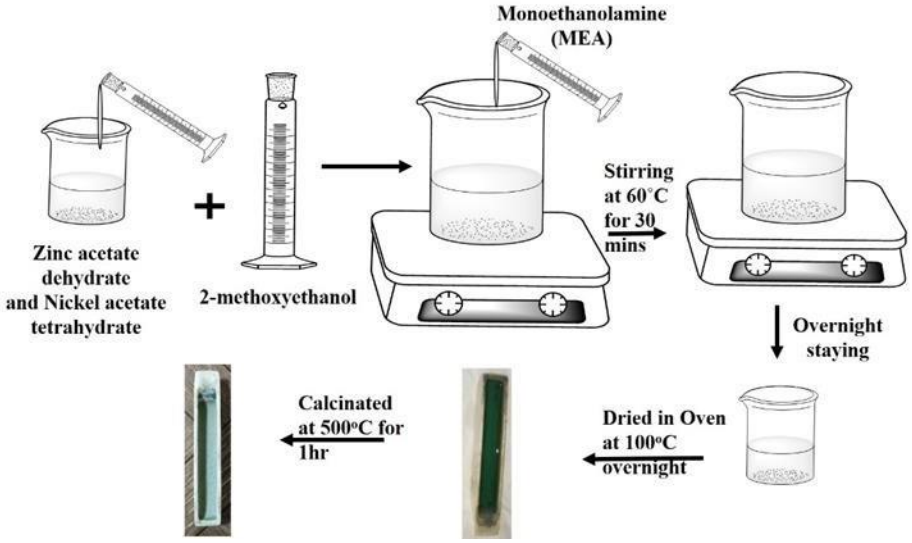

Figure 5.1: Schematic showing the synthesis of Ni-doped ZnO nanoparticle using Sol-gel process with different Ni concentrations (from 0 mol% to 10 mol%).

5.3 Structural changes in Ni doped ZnO nanoparticles

A series of samples of Ni-dopped ZnO nanoparticles were synthesized by sol-gel method, with varying doping concentration from 0 (i.e., pure ZnO nanoparticles) to 10 molar percent.

The structural changes in Ni doped ZnO was investigated by employing X-ray diffraction (XRD) technique. Figure 5.2 revealed that the obtained XRD pattern of ZnO has a wurtzite hexagonal crystal structure, which has been confirmed from JCPDS card 01-089-1397 and also the presence of the NiO phase at and above ~ 3.5 mol% Ni doping has been evident,

by the JCPDS PDF card (00-047-1049) [128]. The XRD patterns of pure ZnO, 3.64 mol% Ni-doped ZnO, and 8 mol% Ni-doped ZnO are presented in Figure 5.2, which shows the successful incorporation of Ni into the ZnO lattice. Figure 5.3 highlights the distinct shifts in the peak positions (*2θ*) corresponding to the three intense diffraction planes: (101), (100), and (002). These shifts observed for 3.64% Ni-doped ZnO and 8% Ni-doped ZnO clearly indicate the structural modifications induced by Ni doping. Figure 5.3 shows that at lower concentration of Ni doping (Ni ≤ 3.5-4 mol%) the diffraction angles (*2θ*) for the three prominent peaks—ZnO (101), ZnO (100), and ZnO (002)—shift towards lower values, corresponding to an increase in *d*-spacing. This behavior can be attributed to Ni^{2+} ions being trapped in non-equilibrium positions within the ZnO lattice [44]. Such incorporation introduces lattice distortions and expands the interplanar spacing. In contrast, at higher concentration of Ni doping (Ni ≥ 3.5-4 mol%), the diffraction angles (*2θ*) for the same peaks shift towards higher values, indicating a reduction in the corresponding d-spacings. This phenomenon is due to the substitution of Zn^{2+} ions (ionic radius 0.60 Å) with smaller Ni^{2+} ions (ionic radius 0.55 Å) at lattice sites, resulting in lattice contraction [129].

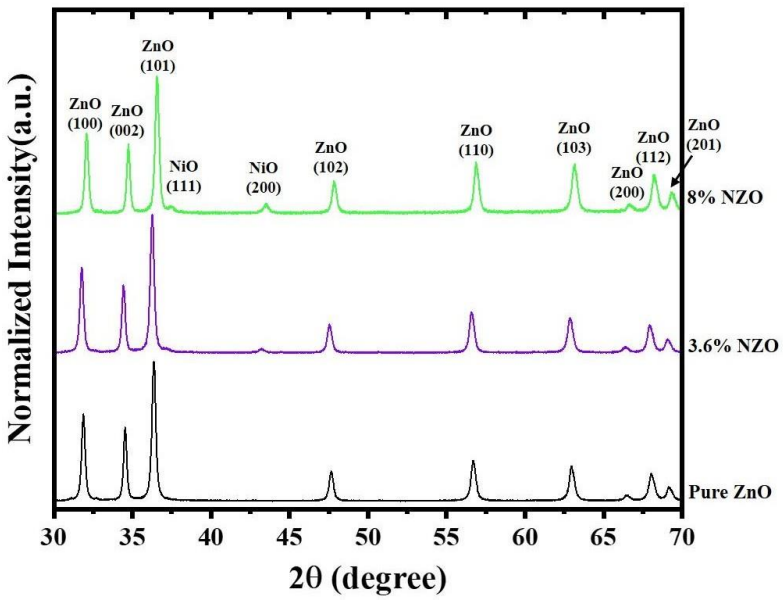

Figure 5.2: XRD pattern of pure ZnO and Ni doped ZnO (NZO) at different Ni concentrations.

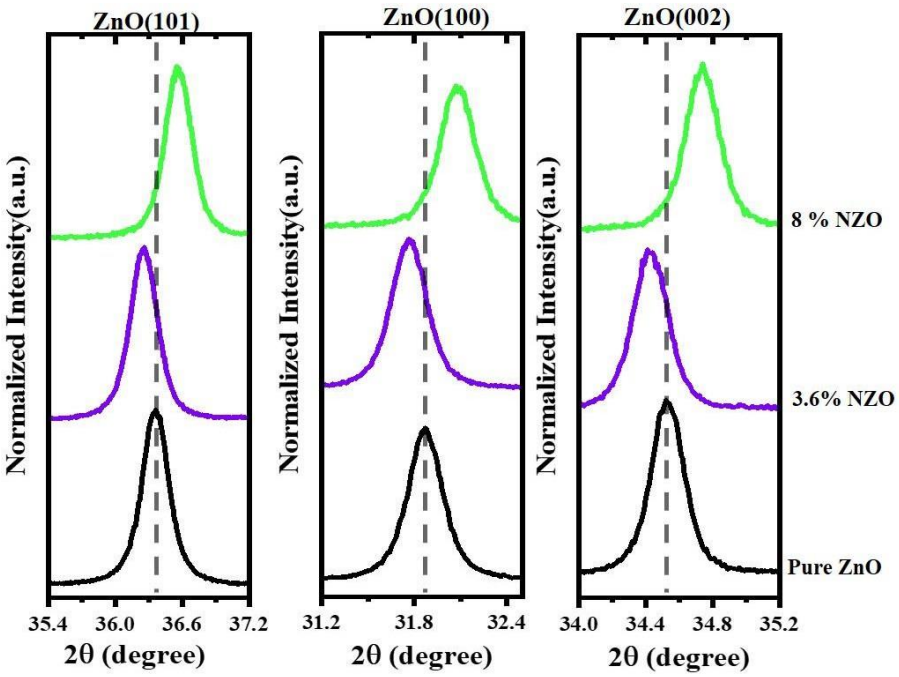

Figure 5.3: XRD peak shift of ZnO (101), (100) and (002) planes with different Ni doping concentrations. The dotted line shown in the figure are guides to viewer eye.

For a qualitative understanding of structural changes of pure ZnO and Ni-doped ZnO, Rietveld refinement analysis is performed. Figure 5.4 shows some characteristic Rietveld refinement results, exhibiting pure ZnO, 3.6% Ni-doped ZnO, and 8% Ni-doped ZnO [130]. This detailed Rietveld refinement provides insights into the structural parameters and phase composition of the samples.

From the Rietveld refinement shown in Figures 5.4 and 5.5, the crystallite sizes (*D*) of pristine ZnO, Ni-doped ZnO, and the emerging NiO phase were calculated using Debye Scherrer's formula (equation 5.1.)

$$D = \frac{K\lambda}{\beta \cos\theta} \qquad \textbf{(5.1)}$$

where λ is the wavelength of incident X-ray, β is the full width at half maximum (FWHM) of the diffraction peak, K is a dimensionless shape factor, with a value close to 0.9 and 2θ is the diffraction angle.

The estimated crystallite size for undoped ZnO and Ni-doped ZnO is approximately 26 to 27 nm, while the crystallite size of the NiO phase [131], formed at different Ni% concentrations, ranges between 17 and 20 nm. As observed earlier, the emergence of the NiO phase begins at and above 3.6% Ni doping in ZnO. However, Rietveld refinement reveals that the crystallite size of the NiO phase remains consistent within the range of 17–20 nm, even as the Ni doping concentration increases beyond 3.6%. This observation indicates that while the formation of the NiO phase is influenced by Ni doping, the crystallite size of this secondary phase stabilizes at higher doping levels, suggesting limited further structural evolution of the NiO phase under these conditions [132].

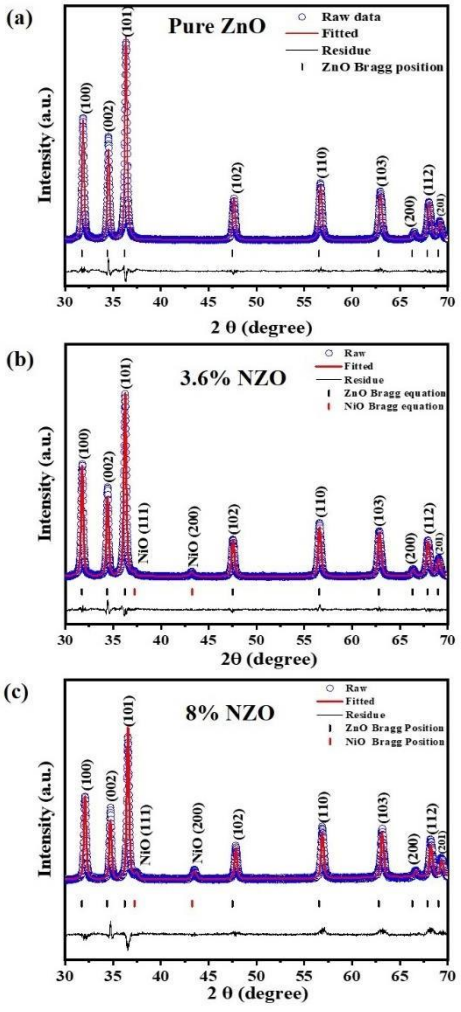

Figure 5.4: Rietveld analysis of characteristic Ni doped ZnO samples. (a) Pure ZnO (i.e., 0% Ni doping) (b) 3.6% Ni doped and (c) 8% Ni doped ZnO samples.

From Figure 5.5, it has been observed that Ni doping above ~3.5 to 4 mol% leads to a decrease in the corresponding d-spacing values, with a reduction of up to ~0.6% at 10 mol% Ni doping. This decrease in d-spacing is indicative of structural contraction within the ZnO lattice, likely resulting from the substitution of Zn^{2+} ions (ionic radius 0.60 Å) with the smaller Ni^{2+} ions (ionic radius 0.55 Å) at lattice sites. This substitution introduces significant lattice modifications, aligning with the structural changes noted in XRD studies.

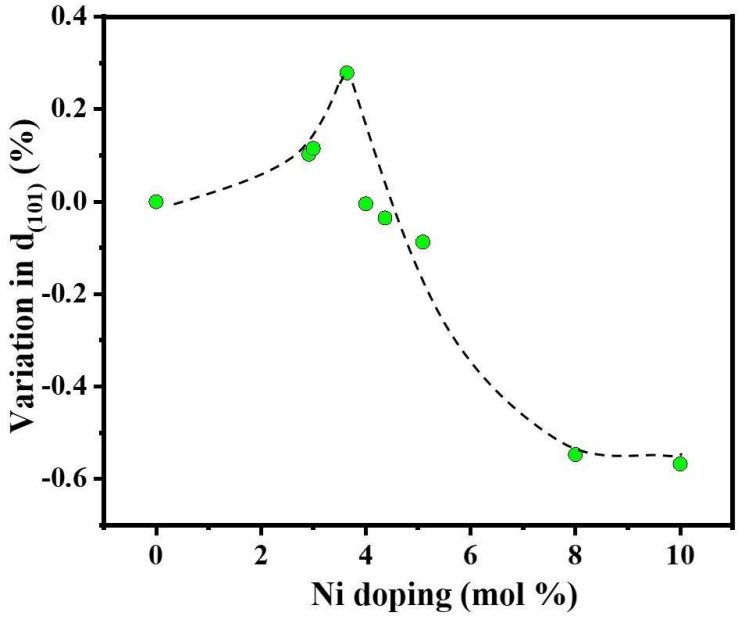

Figure 5.5: Representation of variation in *d*-spacing (%) corresponding to the plane (101) with Ni doping (mol%).

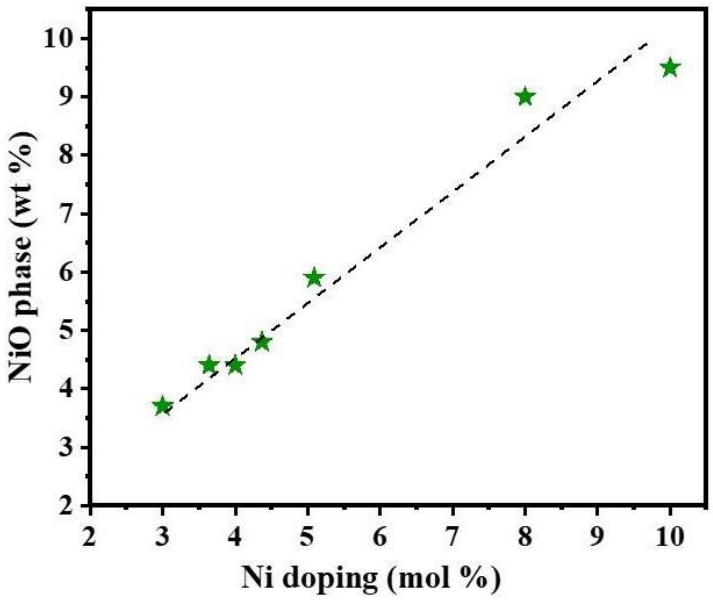

Figure 5.6: Representation of variation in NiO phase (wt%) with variation in Ni doping (mol%) in ZnO. An eye guided dotted line is shown in the Figure.

From the XRD studies, it can be concluded that significant structural changes in the configuration of Ni-doped ZnO occur beyond the threshold value of 3.5 mol% Ni doping. Notably, the emergence of a new NiO phase is observed at and above this the threshold value of 3.5 mol%. Furthermore, it is evident that the crystallite size of the NiO phase stabilizes and remains unchanged with further increases in Ni doping beyond 3.5%, indicating a structural equilibrium for the NiO phase formation at higher doping levels. These findings highlight the critical role of the 3.6% Ni doping threshold in inducing both structural modifications in ZnO and the formation of a stable NiO secondary phase**.** From Figure 5.6, the Rietveld refinement of XRD data reveals an increasing presence of NiO phases as the Ni doping concentration rises, ranging from ~3.6 wt% at ~3% Ni doping to ~9.5 wt% at ~10% Ni doping. Interestingly, while the amount of NiO phases increases, the crystallite size of these phases remains relatively constant, at approximately 17–20 nm. This indicates that while the formation of NiO

phases becomes more pronounced with higher doping concentrations, their crystallite dimensions are unaffected, suggesting a stable growth mechanism of NiO domains within the ZnO matrix.

5.4 Results from Raman Spectroscopy for Ni doped ZnO nanoparticles

In view of the XRD inferences, Raman spectroscopy was employed to verify the proposition, and for further understanding of the structural/configurational changes in ZnO nanostructure due to the different concentration of Ni-doping.

The Raman spectrum of pure ZnO exhibits characteristic peaks that provide valuable insights into the vibrational properties of its hexagonal wurtzite crystal structure [133]. These peaks arise from the optical and acoustic phonon modes associated with the Zn and O atoms in the lattice. The most prominent features include the $\boldsymbol{E_2}$ **(low)** mode, observed around 98 cm^{-1}, which corresponds to the vibrations of heavier Zn atoms. Another significant mode is the $\boldsymbol{E_2}$**(high)** mode at ~438 cm^{-1}, arising from the vibrations of lighter oxygen atoms. It is the most intense and well-defined peak in the spectrum, commonly used as an indicator of crystallinity and structural quality [6]. The second-order Raman peaks were observed at ~204 cm^{-1} and 330 cm^{-1}, which is related to $2E_2$(low) and E_2(high)-E_2(low) [124].

In Figures 5.7 and 5.8, the Raman spectra of Ni-doped ZnO reveal an additional broad vibrational mode around 530 cm^{-1}, marked by an asterisk (*), which is absent in the spectra of undoped ZnO [134]. This mode is attributed to a local vibrational mode associated with Ni^{2+} ions substituting Zn^{2+} ions in the ZnO lattice [26]. The substitution of Ni^{2+} introduces localized distortions and modifies the vibrational dynamics of the host lattice, resulting in the emergence of this new mode.

Another significant contributing factor to the appearance of this additional vibrational mode is the activation of host lattice defects [129].

With increasing Ni doping content, intrinsic defects such as oxygen vacancies and zinc interstitials are amplified, further perturbing the lattice vibrational modes [134]. These defects not only influence the structural and electronic properties but also play a critical role in modifying the vibrational characteristics of ZnO.

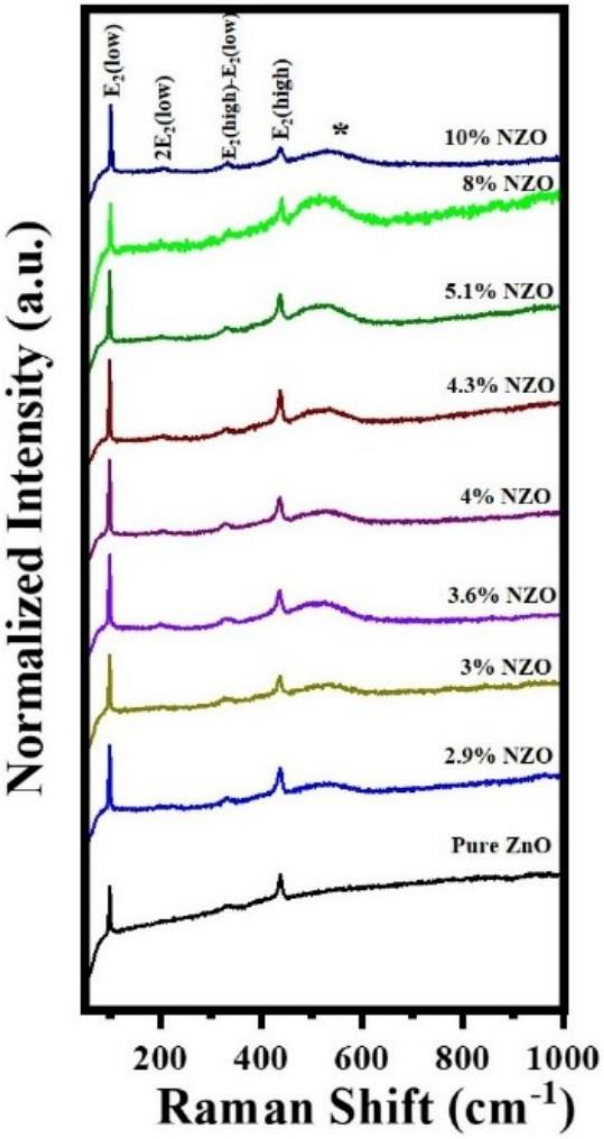

Figure 5.7: Representation Raman spectra of pure ZnO and Ni doped ZnO (NZO) for different doping concentration in mol%**.**

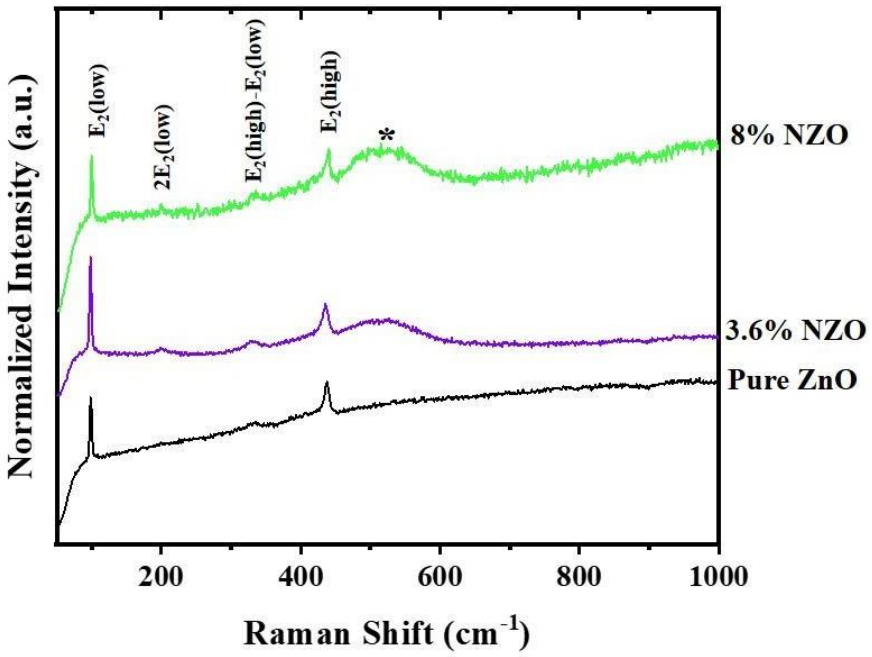

Figure 5.8: Representation of Raman spectra of characteristic Ni doped ZnO and pure ZnO system.

Figure 5.9 shows the shift of E_2(high) and E_2(low) vibrational peaks in Raman spectra of ZnO, which gives clear indication of structural modification of ZnO with Ni doping.

The Raman spectra, as illustrated in Figures 5.9(a) and 5.9(b), reveal that at higher Ni doping concentrations (Ni ≥ 3.5–4 mol%), the E_2(High) and E_2(Low) vibrational modes of ZnO shift to higher wavenumbers compared to undoped ZnO. This shift is attributed to the substitution of Zn^{2+} ions (ionic radius: 0.60 Å, atomic mass: 65 amu) by smaller and lighter Ni^{2+} ions (ionic radius: 0.55 Å, atomic mass: 58 amu) at equilibrium lattice sites within the ZnO base lattice [129]. This substitution induces lattice contraction due to the smaller ionic radius of Ni^{2+}, which strengthens the Zn–O bonds and alters the vibrational dynamics of the lattice. The decrease in the reduced mass of the

vibrational system caused by the substitution also contributes to the shift of vibrational frequencies to higher wavenumbers. These results are fully consistent with the inferences drawn from XRD data.

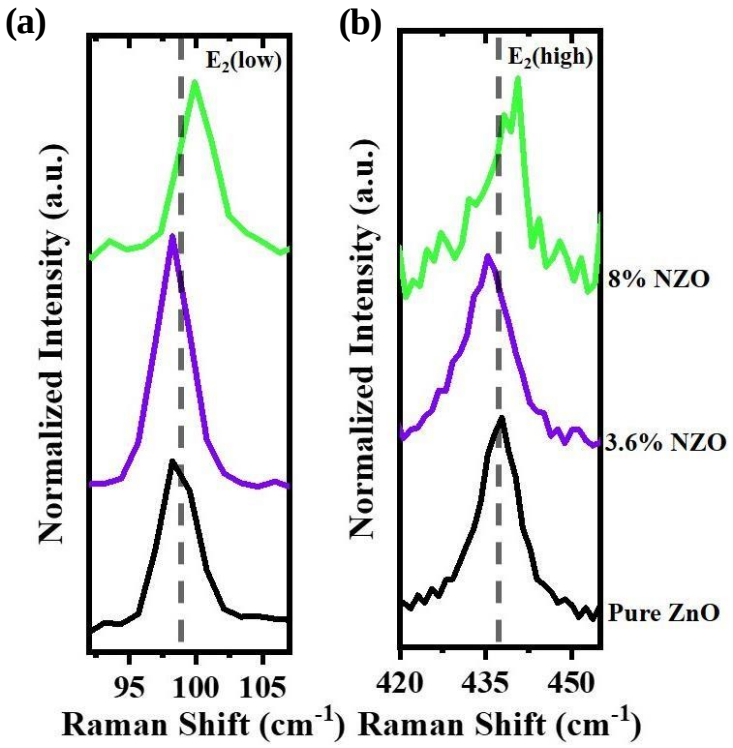

Figure 5.9: Raman spectra of pure and Ni-doped ZnO samples. (a) Peak shift of E_2(low) vibrational mode of 3.6% NZO and 8 % NZO with respect to pure ZnO. (b) Peak shift of E_2(high) vibrational mode of 3.6% NZO and 8% NZO with respect to pure ZnO.

Furthermore, Figures 5.10(a) and 5.10(b) show the variation in the positions of the E_2(High) and E_2(Low) vibrational modes of ZnO with different Ni doping percentages. At lower doping concentrations (Ni ≤ 3.5–4 mol%), these modes exhibit a shift towards lower wavenumbers compared to undoped ZnO. This behavior is attributed to the trapping of Ni^{2+} ions in non-equilibrium positions within the ZnO lattice, which introduces local lattice distortions and alters the vibrational dynamics of the material. The incorporation of Ni^{2+} ions in these non-equilibrium sites increases the overall reduced mass of the vibrational system, leading to

the observed shift to lower wavenumbers. These shifts in vibrational modes provide direct evidence of the structural modifications induced by Ni doping in ZnO, reflecting the impact of dopant concentration on the lattice dynamics and material properties**.** These results are fully consistent with the inferences drawn from XRD data reflecting the impact of dopant concentration on the lattice dynamics and material properties**.**

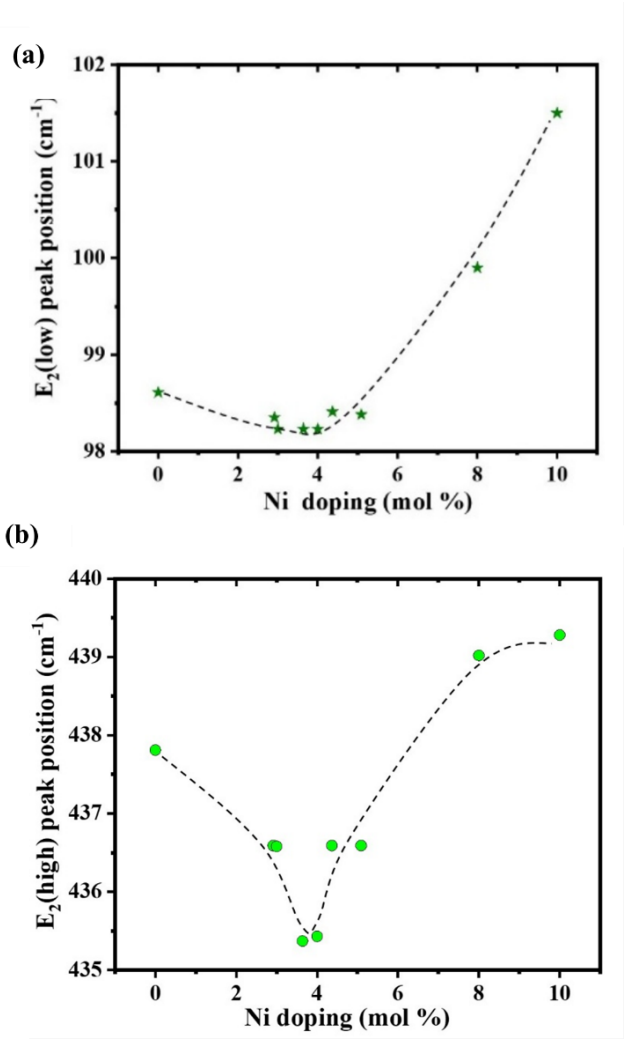

Figure 5.10: Variation of (a) *E2*(low) and (b) *E2*(high) peak position in Ni doped ZnO, with variation of doping concentration (mol%).

In Figure 5.11, the combined analysis of XRD and Raman spectroscopy provides consistent and complementary insights into the structural and vibrational modifications in Ni-doped ZnO nanostructures. The variation

in lattice parameters, as evidenced by XRD data, correlates with shifts in vibrational modes observed in Raman spectra.

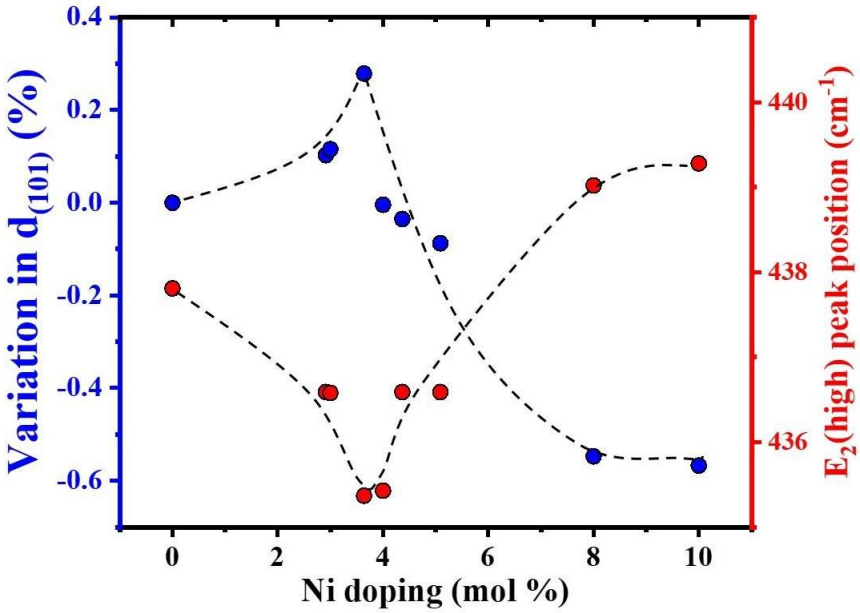

Figure 5.11: Representation of variation in *d*-spacing (%) corresponding to the plane (101) and E_2(high) peak position as a function of Ni-doping percentage.

The combined analysis of XRD and Raman spectroscopy provides consistent and complementary insights into the structural, and vibrational modifications of Ni-doped ZnO nanostructures. Both studies reveal the existence of a critical threshold in Ni doping concentration, approximately in the range of 3.5 to 4 mol%. Below this threshold, the pronounced effects of Ni^{2+} ions being trapped in non-equilibrium positions within the ZnO lattice are evident. And above the threshold Ni doping concentration replacement of Zn^{2+} ion with the Ni^{2+} ion at the lattice site in ZnO base lattice is predominant

5.5 Effect of structural/configuration changes in Ni doped ZnO nanostructured systems based on doping concentration: Application in photocatalytic activity

Finally, to explore whether these external doping mediated variation in structural configuration/defects for such Ni doped ZnO nanostructures can exhibit any effect in their application in terms of their involving their structural, and electronic properties changes, thus we carried out experiments on photocatalytic activity measurements [135, 136].

The photocatalytic activity of Ni-doped ZnO samples was systematically investigated and compared with pure ZnO by evaluating the photodegradation rate of Rhodamine B (RhB) under ultraviolet (UV) light illumination. The experiments were performed using a 150 W high-pressure mercury (Hg) lamp emitting UV light, where the degradation of RhB served as the model reaction. For each set of measurements, first, the sample was dispersed with 1 mg/ml concentration in RhB (22×10^{-6} M) aqueous solution and stirred rigorously with magnetic stirrer in dark to reach the equilibrium. Subsequently, the solution was exposed to UV light while maintaining stirring at room temperature and ambient pressure. At regular time intervals, a specific amount of the solution was withdrawn, centrifuged, and analyzed for degradation. The degradation rate of RhB was determined by monitoring the relative intensity of its characteristic optical absorption band centered at ≈554 nm, measured using a UV–vis spectrophotometer (Perkin Elmer Lambda-35). The measurements were repeated until RhB degradation exceeded 70%, enabling accurate evaluation of the photocatalytic performance for each sample.

The results, depicted in Figure 5.13, show the absorption spectra of RhB under UV illumination for regular time intervals in the presence of pure ZnO and Ni-doped ZnO samples with varying Ni doping percentages. It was observed that the characteristic absorption peak of RhB at 554 nm decreased monotonically with increasing UV exposure time, indicating progressive degradation of RhB. Notably, the sample with 3.6% Ni doping exhibited exceptional photocatalytic performance, achieving nearly 100% degradation of RhB within 80 minutes.

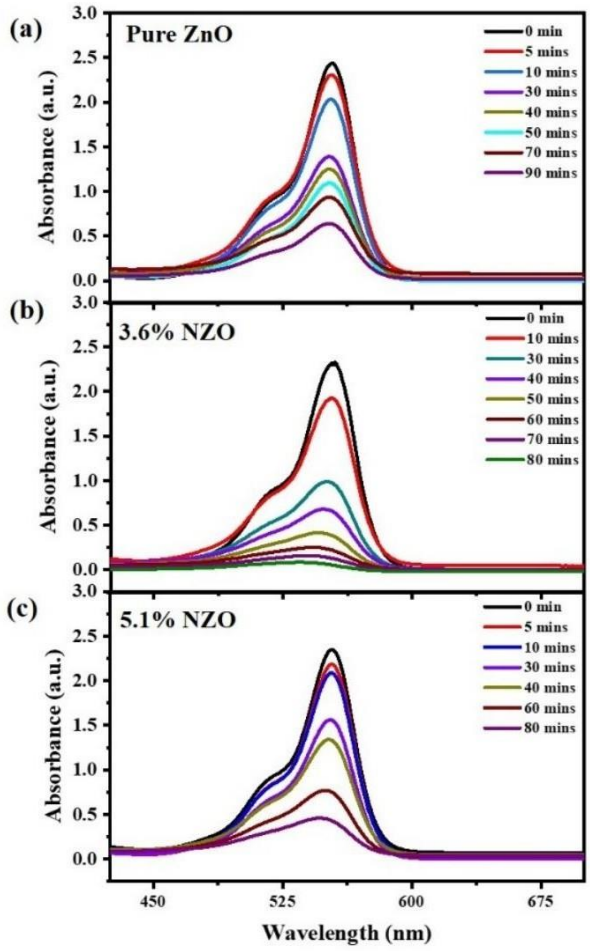

Figure 5.12: Absorption spectra of RhB after different photodegradation durations upon UV irradiation in presence of: (a) pure ZnO (b) 3.6% Ni doped ZnO (c) 5.1% Ni doped ZnO.

Figure 5.14 shows the normalized concentration, C/C_0, of remaining RhB after degradation at each irradiated time interval, for different Ni

doped ZnO along with pure ZnO sample as reference. Here, the changes of normalized concentration (C/C_0) of RhB with UV irradiation due to degradation are assumed to be proportional to the corresponding normalized absorbance (A/A_0) of the 554 nm main peak of the absorption spectrum of the dye solution [136]. The photocatalytic reaction rate constant, k, was calculated by fitting the C/C_0 vs time (t) data for a given sample using the well-known expression for the first order reaction given by Equation:

$$\frac{C}{C_0} = e^{-k*t} \qquad \textbf{(5.2)}$$

Where, k quantifies the photocatalytic activity of catalyst [137].

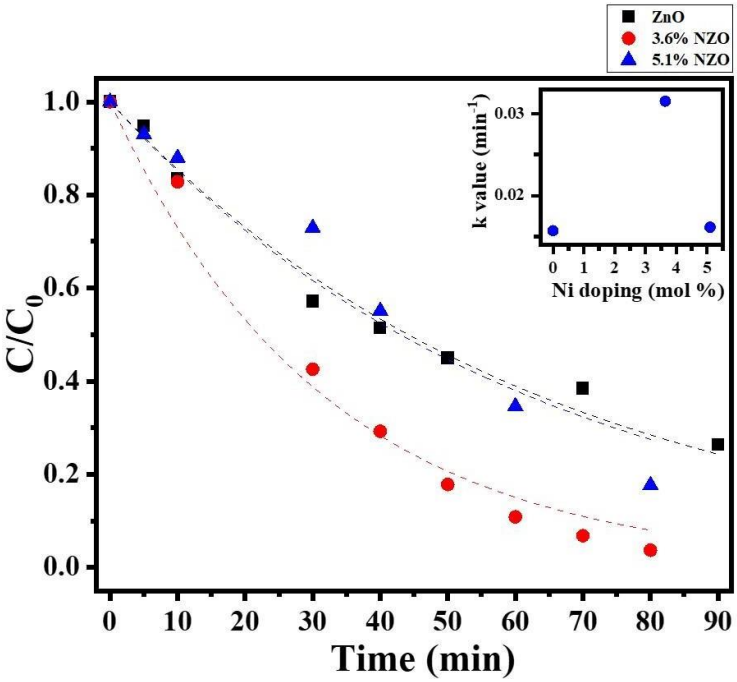

Figure 5.13: Change in normalized concentration (C/C_0) of RhB dye vs. irradiation time in the presence of ZnO (black square), 3.6% Ni-doped ZnO (red circle), and 5.1% Ni-doped ZnO (blue triangle). Inset shows photodegradation reaction rate constant (k) in min^{-1} with different Ni doping percentage.

Therefore, from Figure 5.12 and Figure 5.13, we conclude that the maximum efficiency of photocatalytic activity of Ni-doped ZnO system for threshold amount of Ni doping (i.e., at ~3.6 mol% Ni doping) exhibiting 100% enhancement in degradation rate constant (*k*), in comparison to that of the pure ZnO. Interestingly, it shows much better efficiency with respect to that of the higher concentration of Ni doped ZnO (i.e., above the threshold doping concentration, e.g., 8 mol% Ni doping) as well.

5.6 Summary

In summary, this chapter investigates the structural, configurational, and electronic modifications in ZnO induced by Ni doping, with a focus on insights obtained through XRD, Raman spectroscopy, and photocatalytic studies. XRD analysis highlights significant changes, including variations in d-spacing and the formation of NiO secondary phases, confirmed by Rietveld refinement. At lower Ni doping levels (up to 3.5–4%), Ni^{2+} ions occupy non-equilibrium positions in the ZnO lattice, leading to increased d-spacing and Raman mode shifts to lower wavenumbers. In contrast, at higher doping levels (≥ 4%), Ni^{2+} ions substitute Zn^{2+} ions at lattice sites, causing *d*-spacing to decrease and Raman modes to shift to higher wavenumbers. These structural and vibrational changes directly correlate with the doping concentration, providing valuable insights into the interplay between doping and material properties.

The photocatalytic performance of Ni-doped ZnO was evaluated through the degradation of Rhodamine B under UV light. Among the investigated samples, 3.6% Ni-doped ZnO demonstrated superior photocatalytic efficiency, achieving nearly 100% degradation of RhB within 80 minutes. This enhancement is attributed to the optimal role of Ni doping in the ZnO nanostructure system, which induces significant changes in its electronic and optical properties. These changes facilitate efficient

photocatalytic activity at threshold doping concentration of Ni in the ZnO system.

Together, the findings establish Ni-doped ZnO as a highly tunable material with enhanced functional properties suitable for advanced applications in optoelectronics, spintronics, sensing, and environmental remediation. The integration of structural, vibrational, and photocatalytic studies in this chapter provides a comprehensive understanding of the role of Ni doping in tailoring ZnO's properties for diverse technological applications. Further investigations are ongoing to get in-depth understanding of this system by employing additional techniques such as photoluminescence (PL) spectroscopy, XPS, FTIR, etc.

Chapter 6

Conclusion and Future scope

6.1 Conclusion

This chapter recaps all the conclusions derived from the research conducted and detailed in this thesis. Additionally, it explores potential future directions and opportunities for further advancements in this field.

This thesis investigates the impact of confinement, focusing on how surfaces and interfaces influence the structure, morphology, and optical properties of nanostructured semiconductor material Zinc Oxide (ZnO). The thesis work explores the effect of growth mediated intrinsic defects and the external doping induced extrinsic defects in confined ZnO nanostructured systems, towards the control of its structural and thus its electronic and optical properties.

In the first part of the work, the study of surface/interface and confinement effects on optical/electronic and structural properties of ALD grown ZnO thin film (ZnO_a) on SiO_2, as a function of film thickness ware explored via photoabsorption (PA) and photoluminescence (PL). A non-monotonic change in the optical properties with variation of ZnO film thickness was observed. The PA studies demonstrates (presented in Figure 1), the red shift in exciton energy (i.e., peak in optical absorption ($E_{g,f}$)) with the increasing ZnO_a film thickness (d) in the range of ~2 nm to ~19 nm, indicates the quantum size effect. The quantum confinement effect has been also clearly evident from PL study. The quantum size effect at film thickness d up to 20 nm follows the expected $1/d^2$ dependence on film thickness and indicates the existence of a homogeneous film. Importantly, with further increase of d (from ~38 nm to ~69 nm), however, a blueshift in both PA and PL was observed. Simultaneously, the Urbach energy (E_u) or disorder, as extracted from the PA studies, increases with increasing ZnO_a film thickness in the first stage until a threshold film thickness at around 19

nm is reached, followed by a plateau up to d = 40 nm, above which it starts to decrease again. Peak in optical absorption ($E_{g,f}$) and photoabsorption edge or optical bandgap ($E_{g,e}$) have same dependence on film thickness with their corresponding values separated by 0.2 eV. Urbach energy (E_u) anti-correlates with the excitonic energy or peak position in optical absorption ($E_{g,f}$) and with optical bandgap ($E_{g,e}$). Detailed PL studies demonstrate the presence of two different types of defects levels, oxygen vacancy (DLE1) and Zn interstitial (DLE2) in these systems. There is a continuous trend of increasing concentration of oxygen vacancies (DLE1) with decreasing film thickness, as a results of enhanced surface effect. On the other hand, there is a non-monotonic trend in concentration of Zn interstitial (DLE2) vacancies with film thickness. Importantly, the thickness dependence of the Urbach energy follows a similar trend as the intensity of DLE(2).

In the next section of the thesis, origin of the observed non-monotonic change in the optical properties of ZnO with increasing film thickness has been explored. Identification of the phenomena involving self-healing of defect mediated disorder in ZnO thin films, has been discussed. The change of growth mode of thin film is evident from the FESEM. Dense nanocrystalline and smooth ZnO films are formed for film thicknesses up to 20 nm. On the other hand, ZnO films with a higher thickness exhibit a grainy morphology, with an increasing grain size as a function of increasing film thickness. The change of growth mode from the nanocrystalline to the grainy structure for ZnO film thickness, correlates with the saturation of the Urbach energy (E_{u}) as a function of film thickness, as well as with the minimum of exciton peak energy ($E_{\mathrm{g,f}}$). The results imply that the concentration of these interstitials is *spontaneously* reduced for crystallites that approach more and more bulk properties, i.e., there is a mechanism of self-healing for these interstitial defects. Furthermore, the XRD pattern, estimated values of strain (along the surface normal) and the in-plane compressive stress were suggesting that the change of growth mode to mesoscopic crystallites is coupled

with an almost complete relaxation of the in-plane compressive stress, correlates to the change in growth mode of the films.

Now, the above-mentioned findings allow us to propose a physical scenario for the origin of this unusual behavior found as a function of film thickness.

1. The quantum size effect at film thickness d up to 20 nm follows the expected $1/d^2$ dependence on film thickness and indicates the existence of a homogeneous film.
2. At the same time, there is a build-up of disorder in these films under the chosen ALD growth conditions that we mainly attribute to Zn interstitials in the bulk.
3. On the contrary, there is a continuous trend of decreasing concentration of oxygen vacancies that is not correlated with (2). We suggest that these vacancies are mainly formed close to the surface. Otherwise, they should also contribute to the disorder.
4. The spontaneous decrease of disorder as a function of d without any change in growth conditions can be directly related to the change of growth mode from an essentially smooth to a grainy structure. This effect seems to be enhanced by larger and larger ZnO crystallites formed as a function of *d*.
5. We suggest that this change of morphology also reduces the activation barrier for water dissociation and/or the activation energy for diffusion of Zn interstitials. Only if these migrate to the surface and react with oxygen atoms there will be a spontaneous effect of self-annealing in the whole material. Further experiments will be useful to corroborate this scenario by varying the pressure of the precursors and growth temperature.

The second part of the thesis, investigates the structural, configurational, and electronic modifications in ZnO induced by Ni doping. XRD analysis highlights significant changes, including variations in d-spacing and the formation of NiO secondary phases. At lower Ni doping levels (up to 3.5–4%), Ni^{2+} ions occupy non-equilibrium positions in the ZnO lattice, in contrast, at higher doping levels (≥ 4%), Ni^{2+} ions substitute Zn^{2+} ions at lattice sites, leading to increase and decrease in d-spacing, respectively along with the Raman mode shifts to lower and higher wavenumbers, respectively. These structural and vibrational changes directly correlate with the doping concentration, providing valuable insights into the interplay between doping and material properties. The significance of this Ni-doped ZnO system towards its application in photocatalysis was evaluated through the degradation of Rhodamine B (RhB) dye under UV light. Among the investigated samples, 3.6% Ni-doped ZnO demonstrated superior photocatalytic efficiency, achieving nearly 95% degradation of RhB within 80 minutes. This enhancement is attributed to the optimal role of Ni doping in facilitating charge separation and suppressing recombination of photogenerated charge carriers.

The study is important to optimize the properties of ALD ZnO thin film layer and ZnO nanoparticles where different kind of defects play a crucial role in tuning the properties of these nanostructured materials for a particular targeted application. It will provide an insight in determining compatible nanostructure for optoelectronic devices.

6.2 Future prospects of the work

Integrating the benefits from different aspects of the present study, there is much scope to continue this work further in future. Some possible studies are enlisted below:

- The confinement induced (surface/interface mediated) internal structure change leading to thickness dependent optical

properties of ZnO films can be used for further optimizing the performance of ZnO in various applications such as optoelectronic devices (e.g. color sensors, LEDs etc.), photovoltaic applications through tuning of optical properties.

- The work opens a new avenue to explore other prospective materials combinations aiming towards finding tunable properties and corresponding structure/morphology for specific applications in the field of flexible electronics devices (e.g., hybrid optoelectronic devices).
- Following the growth approach of ZnO, the relevant modified electrode materials with advanced structural/morphological properties, can be fabricated to overcome the present-day issues, to achieve higher efficiency in rechargeable batteries.
- Atomic layer deposition of ZnO could be used to modify/coat the surface of novel electrode material for improvement the performance of batteries.
- The findings provide insight for Ni-doped ZnO as a highly tunable material with enhanced functional properties suitable for advanced applications in optoelectronics, spintronics, sensing, and environmental remediation. The integration of structural, vibrational, and photocatalytic studies provides a comprehensive understanding of the role of Ni doping in tailoring ZnO's properties for diverse technological applications.

The knowledge developed through surface/interface and confinement mediated studies can have potential future direction in the applicability of the materials in various devices. The quest of new functionalities utilizing the properties of modified metal oxide in flexible electronics devices, LEDs, sensors and photovoltaic devices, etc. may lead to easier and cheaper application in the near future. The knowledge developed through this surface and interface studies can have the possible major future direction in the applicability of the materials in various devices.

References:

[1] W.G. Kreyling, M. Semmler-Behnke, Q. Chaudhry, A complementary definition of nanomaterial, Nano Today, 5 (2010) 165-168.
[2] B.D. Malhotra, M.A. Ali, Nanomaterials in Biosensors: Fundamentals and Applications, Nanomaterials for Biosensors. 2018:1-74. doi: 10.1016/B978-0-323-44923-6.00001-7. Epub 2017 Oct 21.
[3] H. Dosch, Some general aspects of confinement in nanomaterials, Applied Surface Science, 182 (2001) 192-195.
[4] A. Ashrafi, Quantum Confinement: An Ultimate Physics of Nanostructures, Encyclopedia of Semiconductor Nanotechnology, 1 (2011) 1-67.
[5] X. Zhou, Q. Shen, Y. Wang, Y. Dai, Y. Chen, K. Wu, Surface and interfacial sciences for future technologies, National Science Review, 11 (2024) nwae272.
[6] D. Pal, S. Chattopadhyay, 10 - Surface and interface effects: properties of nanostructured ZnO, in: K. Awasthi (Ed.) Nanostructured Zinc Oxide, Elsevier, 2021, pp. 253-287.
[7] T. Edvinsson, Optical quantum confinement and photocatalytic properties in two-, one- and zero-dimensional nanostructures, Royal Society Open Science, 5 (2018) 180387.
[8] K.R. Choudhury, F. So, Z. Kafafi, Colloidal semiconductor nanocrystal-enabled organic/inorganic hybrid light emitting devices, (2011).
[9] Y. Gu, I.L. Kuskovsky, M. Yin, S. O'Brien, G.F. Neumark, Quantum confinement in ZnO nanorods, Applied Physics Letters, 85 (2004) 3833-3835.
[10] D.C. Agrawal, Introduction to nanoscience and nanomaterials, World Scientific Publishing Company, 2013.
[11] A.L. Schoenhalz, J.T. Arantes, A. Fazzio, G.M. Dalpian, Surface and Quantum Confinement Effects in ZnO Nanocrystals, The Journal of Physical Chemistry C, 114 (2010) 18293-18297.
[12] S. Raha, M. Ahmaruzzaman, ZnO nanostructured materials and their potential applications: progress, challenges and perspectives, Nanoscale Advances, 4 (2022) 1868-1925.
[13] Z. Kang, H. Si, S. Zhang, J. Wu, Y. Sun, Q. Liao, Z. Zhang, Y. Zhang, Interface Engineering for Modulation of Charge Carrier Behavior in ZnO Photoelectrochemical Water Splitting, Advanced Functional Materials, 29 (2019) 1808032.
[14] K.M. Gupta, N. Gupta, Semiconductor Materials: Their Properties, Applications, and Recent Advances, in: K.M. Gupta, N. Gupta (Eds.) Advanced Semiconducting Materials and Devices, Springer International Publishing, Cham, 2016, pp. 3-40.
[15] L.-D. Yuan, H.-X. Deng, S.-S. Li, S.-H. Wei, J.-W. Luo, Unified theory of direct or indirect band-gap nature of conventional semiconductors, Physical Review B, 98 (2018) 245203.
[16] P. Yu, Fundamentals of semiconductors, Springer, 2005.
[17] A. Alkauskas, M.D. McCluskey, C.G. Van de Walle, Tutorial: Defects in semiconductors—Combining experiment and theory, Journal of Applied Physics, 119 (2016) 181101.
[18] E.C. Larkins, J.S. Harris Jr, Quality gaas and aigaas, Molecular beam epitaxy: applications to key materials, (1995) 114.

[19] H. Zeng, G. Duan, Y. Li, S. Yang, X. Xu, W. Cai, Blue Luminescence of ZnO Nanoparticles Based on Non-Equilibrium Processes: Defect Origins and Emission Controls, Advanced Functional Materials, 20 (2010) 561-572.
[20] L. Petti, N. Münzenrieder, C. Vogt, H. Faber, L. Büthe, G. Cantarella, F. Bottacchi, T.D. Anthopoulos, G. Tröster, Metal oxide semiconductor thin-film transistors for flexible electronics, Applied Physics Reviews, 3 (2016) 021303.
[21] V. Vasanthi, N. Sivanantham, L. Saathvika, N. Gopalakrishnan, Metal oxide charge transport materials for light emitting diodes - An overview, Materials Science in Semiconductor Processing, 165 (2023) 107679.
[22] A. Janotti, C.G. Van de Walle, Fundamentals of zinc oxide as a semiconductor, Reports on Progress in Physics, 72 (2009) 126501.
[23] Ü. Özgür, Y.I. Alivov, C. Liu, A. Teke, M.A. Reshchikov, S. Doğan, V. Avrutin, S.J. Cho, H. Morkoç, A comprehensive review of ZnO materials and devices, Journal of Applied Physics, 98 (2005) 041301.
[24] A.B. Djurišić, A.M.C. Ng, X.Y. Chen, ZnO nanostructures for optoelectronics: Material properties and device applications, Progress in Quantum Electronics, 34 (2010) 191-259.
[25] L. Vayssieres, Growth of Arrayed Nanorods and Nanowires of ZnO from Aqueous Solutions, Advanced Materials, 15 (2003) 464-466.
[26] X.D. Li, T.P. Chen, P. Liu, Y. Liu, Z. Liu, K.C. Leong, A study on the evolution of dielectric function of ZnO thin films with decreasing film thickness, Journal of Applied Physics, 115 (2014) 103512.
[27] D.R. Baer, M.H. Engelhard, G.E. Johnson, J. Laskin, J. Lai, K. Mueller, P. Munusamy, S. Thevuthasan, H. Wang, N. Washton, A. Elder, B.L. Baisch, A. Karakoti, S.V.N.T. Kuchibhatla, D. Moon, Surface characterization of nanomaterials and nanoparticles: Important needs and challenging opportunities, Journal of Vacuum Science & Technology A, 31 (2013) 050820.
[28] P. Rajpoot, A. Ghosh, A. Kaur, S. Arora, M. Henini, S. Dhar, S. Chattopadhyay, Epitaxial growth of excitonic single crystals and heterostructures: Oxides and nitrides, MRS Bulletin, 49 (2024) 885-898.
[29] D. Pal, J. Singhal, A. Mathur, A. Singh, S. Dutta, S. Zollner, S. Chattopadhyay, Effect of substrates and thickness on optical properties in atomic layer deposition grown ZnO thin films, Applied Surface Science, 421 (2017) 341-348.
[30] D. Pal, A. Mathur, A. Singh, J. Singhal, A. Sengupta, S. Dutta, S. Zollner, S. Chattopadhyay, Tunable optical properties in atomic layer deposition grown ZnO thin films, Journal of Vacuum Science & Technology A, 35 (2016) 01B108.
[31] A. Galdámez-Martinez, G. Santana, F. Güell, P.R. Martínez-Alanis, A. Dutt, Photoluminescence of ZnO Nanowires: A Review, in: Nanomaterials, 2020.
[32] J. Rodrigues, N. Ben Sedrine, M.R. Correia, T. Monteiro, Photoluminescence investigations of ZnO micro/nanostructures, Materials Today Chemistry, 16 (2020) 100243.
[33] R.C. Rai, Analysis of the Urbach tails in absorption spectra of undoped ZnO thin films, Journal of Applied Physics, 113 (2013) 153508.
[34] B.P. Zhang, C.Y. Liu, Y. Segawa, Y. Kashiwaba, K. Haga, Free excitonic transition of zinc oxide nanocrystallite films formed on amorphous substrates by metalorganic chemical vapor deposition, Thin Solid Films, 474 (2005) 165-168.
[35] C.W. Teng, J.F. Muth, Ü. Özgür, M.J. Bergmann, H.O. Everitt, A.K. Sharma, C. Jin, J. Narayan, Refractive indices and absorption coefficients of MgxZn1−xO alloys, Applied Physics Letters, 76 (2000) 979-981.

[36] V. Srikant, D.R. Clarke, On the optical band gap of zinc oxide, Journal of Applied Physics, 83 (1998) 5447-5451.
[37] J.F. Muth, R.M. Kolbas, A.K. Sharma, S. Oktyabrsky, J. Narayan, Excitonic structure and absorption coefficient measurements of ZnO single crystal epitaxial films deposited by pulsed laser deposition, Journal of Applied Physics, 85 (1999) 7884-7887.
[38] A. Anjum, R. Ahmed, Z.A. Umar, S. Azzam, T. Hussain, M.N. Sarwar, M.A. Baig, Structure and defects-related optical properties of highly (002)-oriented zinc oxide thin films, Physica B: Condensed Matter, 644 (2022) 414195.
[39] R. Varadhaseshan, S. Meenakshi Sundar, Existence of ferromagnetism and structural characterization of nickel doped ZnO nanocrystals, Applied Surface Science, 258 (2012) 7161-7165.
[40] P.P. Murmu, J. Kennedy, Structural and magnetic properties of heavily-doped Co into ZnO single crystals, Int. J. ChemTech Res., 7 (2015) 1651-1655.
[41] T.A. Dar, A. Agrawal, R.J. Choudhary, P. Sen, Electrical and magnetic transport properties of undoped and Ni doped ZnO thin films, Thin Solid Films, 589 (2015) 817-821.
[42] T.A. Dar, A. Agrawal, P. Misra, L.M. Kukreja, P.K. Sen, P. Sen, Valence and conduction band offset measurements in Ni0.07Zn0.93O/ZnO heterostructure, Current Applied Physics, 14 (2014) 171-175.
[43] T. Wakano, N. Fujimura, Y. Morinaga, N. Abe, A. Ashida, T. Ito, Magnetic and magneto-transport properties of ZnO:Ni films, Physica E: Low-dimensional Systems and Nanostructures, 10 (2001) 260-264.
[44] K. Raja, P.S. Ramesh, D. Geetha, Synthesis, structural and optical properties of ZnO and Ni-doped ZnO hexagonal nanorods by Co-precipitation method, Spectrochimica Acta Part A: Molecular and Biomolecular Spectroscopy, 120 (2014) 19-24.
[45] K.P. Shinde, R.C. Pawar, B.B. Sinha, H.S. Kim, S.S. Oh, K.C. Chung, Optical and magnetic properties of Ni doped ZnO planetary ball milled nanopowder synthesized by co-precipitation, Ceramics International, 40 (2014) 16799-16804.
[46] F. Cai, J. Wang, Z. Yuan, Y. Duan, Magnetic-field effect on dye-sensitized ZnO nanorods-based solar cells, Journal of Power Sources, 216 (2012) 269-272.
[47] R.W. Johnson, A. Hultqvist, S.F. Bent, A brief review of atomic layer deposition: from fundamentals to applications, Materials Today, 17 (2014) 236-246.
[48] S.M. George, Atomic Layer Deposition: An Overview, Chemical Reviews, 110 (2010) 111-131.
[49] Y.S. Jung, A.S. Cavanagh, A.C. Dillon, M.D. Groner, S.M. George, S.-H. Lee, Enhanced Stability of LiCoO2 Cathodes in Lithium-Ion Batteries Using Surface Modification by Atomic Layer Deposition, Journal of The Electrochemical Society, 157 (2010) A75.
[50] J. Zhao, Y. Wang, Ultrathin Surface Coatings for Improved Electrochemical Performance of Lithium Ion Battery Electrodes at Elevated Temperature, The Journal of Physical Chemistry C, 116 (2012) 11867-11876.
[51] T. Tynell, M. Karppinen, Atomic layer deposition of ZnO: a review, Semiconductor Science and Technology, 29 (2014) 043001.
[52] E.B. Yousfi, J. Fouache, D. Lincot, Study of atomic layer epitaxy of zinc oxide by in-situ quartz crystal microgravimetry, Applied Surface Science, 153 (2000) 223-234.
[53] M. Ritala, M. Leskela, Thin Solid Films, 409 (2002) 138.

[54] S. Jeon, S. Bang, S. Lee, S. Kwon, W. Jeong, H. Jeon, H.J. Chang, H.-H. Park, Structural and Electrical Properties of ZnO Thin Films Deposited by Atomic Layer Deposition at Low Temperatures, Journal of The Electrochemical Society, 155 (2008) H738.
[55] C.J. Brinker, G.W. Scherer, Sol-gel science: the physics and chemistry of sol-gel processing, Academic press, 2013.
[56] L.C. Klein, Sol-gel technology for thin films, fibers, preforms, electronics, and specialty shapes, (No Title), (1988).
[57] L.L. Hench, J.K. West, The sol-gel process, Chemical Reviews, 90 (1990) 33-72.
[58] D. Bokov, A. Turki Jalil, S. Chupradit, W. Suksatan, M. Javed Ansari, I.H. Shewael, G.H. Valiev, E. Kianfar, Nanomaterial by Sol-Gel Method: Synthesis and Application, Advances in Materials Science and Engineering, 2021 (2021) 5102014.
[59] M. Birkholz, Thin Film Analysis by X-Ray Scattering, Wiley-VCH Verlag GmbH & Co. KGaA, 2006.
[60] J. Als-Nielsen, D. McMorrow, Elements of modern X-ray physics, John Wiley & Sons, 2011.
[61] J.K. Basu, M.K. Sanyal, Ordering and growth of Langmuir–Blodgett films: X-ray scattering studies, Physics Reports, 363 (2002) 1-84.
[62] T.P. Russell, X-ray and neutron reflectivity for the investigation of polymers, Materials Science Reports, 5 (1990) 171-271.
[63] M.K. Sanyal, S.K. Sinha, K.G. Huang, B.M. Ocko, X-ray-scattering study of capillary-wave fluctuations at a liquid surface, Physical Review Letters, 66 (1991) 628-631.
[64] A. Gibaud, S. Hazra, X-ray reflectivity and diffuse scattering, Current Science, 78 (2000) 1467-1477.
[65] A. Uysal, M. Chu, B. Stripe, A. Timalsina, S. Chattopadhyay, C.M. Schlepütz, T.J. Marks, P. Dutta, What x rays can tell us about the interfacial profile of water near hydrophobic surfaces, Physical Review B, 88 (2013) 035431.
[66] S.K. Sinha, E.B. Sirota, S. Garoff, H.B. Stanley, X-ray and neutron scattering from rough surfaces, Physical Review B, 38 (1988) 2297-2311.
[67] L.G. Parratt, Surface Studies of Solids by Total Reflection of X-Rays, Physical Review, 95 (1954) 359-369.
[68] S. Chattopadhyay, A. Datta, Effect of Polymer Confinement: Tuning Self-Assembled Growth of Monodisperse Au Nanoparticles on Polystyrene Films, Macromolecules, 40 (2007) 3313-3319.
[69] S. Chattopadhyay, A. Datta, Localization of excitons by molecular layer formation in a polymer film, Physical Review B, 72 (2005) 155418.
[70] S. Chattopadhyay, A. Uysal, B. Stripe, G. Evmenenko, S. Ehrlich, E.A. Karapetrova, P. Dutta, Structural Signal of a Dynamic Glass Transition, Physical Review Letters, 103 (2009) 175701.
[71] S. Chattopadhyay, A. Uysal, B. Stripe, Y.-g. Ha, T.J. Marks, E.A. Karapetrova, P. Dutta, How Water Meets a Very Hydrophobic Surface, Physical Review Letters, 105 (2010) 037803.
[72] B.D. Cullity, Elements of x-ray diffraction, Second edition ed., Addison-Wesley Publishing Company, Inc., Reading, MA, 1978.
[73] M. Yasaka, X-ray thin-film measurement techniques, The Rigaku Journal, 26 (2010) 1-9.

[74] H.-H. Perkampus, Analytical Applications of UV-VIS Spectroscopy, in: H.-H. Perkampus (Ed.) UV-VIS Spectroscopy and Its Applications, Springer Berlin Heidelberg, Berlin, Heidelberg, 1992, pp. 26-80.
[75] B.J. Clark, T. Frost, M.A. Russell, UV Spectroscopy: Techniques, instrumentation and data handling, Springer Netherlands, 1993.
[76] N. Ghobadi, Band gap determination using absorption spectrum fitting procedure, International Nano Letters, 3 (2013) 2.
[77] J. Tauc, Optical Properties of Amorphous Semiconductors, in: J. Tauc (Ed.) Amorphous and Liquid Semiconductors, Springer US, Boston, MA, 1974, pp. 159-220.
[78] J. Tauc, A. Menth, States in the gap, Journal of Non-Crystalline Solids, 8-10 (1972) 569-585.
[79] E.A. Davis, N.F. Mott, Conduction in non-crystalline systems V. Conductivity, optical absorption and photoconductivity in amorphous semiconductors, The Philosophical Magazine: A Journal of Theoretical Experimental and Applied Physics, 22 (1970) 0903-0922.
[80] S.T. Tan, B.J. Chen, X.W. Sun, W.J. Fan, H.S. Kwok, X.H. Zhang, S.J. Chua, Blueshift of optical band gap in ZnO thin films grown by metal-organic chemical-vapor deposition, Journal of Applied Physics, 98 (2005).
[81] S.T. Tan, B.J. Chen, X.W. Sun, X. Hu, X.H. Zhang, S.J. Chua, Properties of polycrystalline ZnO thin films by metal organic chemical vapor deposition, Journal of Crystal Growth, 281 (2005) 571-576.
[82] R.C. Rai, M. Guminiak, S. Wilser, B. Cai, M.L. Nakarmi, Elevated temperature dependence of energy band gap of ZnO thin films grown by e-beam deposition, Journal of Applied Physics, 111 (2012) 073511.
[83] C.R. Ronda, Luminescence: From Theory to Applications, Wiley, 2007.
[84] S. Perkowitz, Optical Characterization of Semiconductors: Infrared, Raman, and Photoluminescence Spectroscopy, Elsevier Science, 1993.
[85] B. Streetman, S. Banerjee, Solid State Electronic Devices, Pearson Education, 2014.
[86] E. Guziewicz, I.A. Kowalik, M. Godlewski, K. Kopalko, V. Osinniy, A. Wójcik, S. Yatsunenko, E. Łusakowska, W. Paszkowicz, M. Guziewicz, Extremely low temperature growth of ZnO by atomic layer deposition, Journal of Applied Physics, 103 (2008) 033515.
[87] S. Vempati, J. Mitra, P. Dawson, One-step synthesis of ZnO nanosheets: a blue-white fluorophore, Nanoscale Research Letters, 7 (2012) 470.
[88] H. Szymanski, Raman Spectroscopy: Theory and Practice, Springer US, 2013.
[89] J.R. Ferraro, K. Nakamoto, Introductory Raman Spectroscopy, Academic Press, 2012.
[90] R. Cuscó, E. Alarcón-Lladó, J. Ibáñez, L. Artús, J. Jiménez, B. Wang, M.J. Callahan, Temperature dependence of Raman scattering in ZnO, Physical Review B, 75 (2007) 165202.
[91] J.M. Calleja, M. Cardona, Resonant Raman scattering in ZnO, Physical Review B, 16 (1977) 3753-3761.
[92] C.A. Arguello, D.L. Rousseau, S.P.S. Porto, First-Order Raman Effect in Wurtzite-Type Crystals, Physical Review, 181 (1969) 1351-1363.
[93] K.D. Vernon-Parry, Scanning electron microscopy: an introduction, III-Vs Review, 13 (2000) 40-44.
[94] J.I. Goldstein, D.E. Newbury, J.R. Michael, N.W.M. Ritchie, J.H.J. Scott, D.C. Joy, Electron Beam—Specimen Interactions: Interaction Volume, in: J.I. Goldstein, D.E. Newbury, J.R. Michael, N.W.M. Ritchie, J.H.J. Scott, D.C. Joy

(Eds.) Scanning Electron Microscopy and X-Ray Microanalysis, Springer New York, New York, NY, 2018, pp. 1-14.
[95] Z. Baji, Z. Lábadi, Z.E. Horváth, M. Fried, B. Szentpáli, I. Bársony, Temperature dependent in situ doping of ALD ZnO, Journal of Thermal Analysis and Calorimetry J Therm Anal Calorim, 105 (2011) 93-99.
[96] Z. Baji, Z. Lábadi, Z.E. Horváth, I. Bársony, Thin Solid Films, 520 (2012) 4703.
[97] J. Hämäläinen, M. Ritala, M. Leskelä, Atomic Layer Deposition of Noble Metals and Their Oxides, Chemistry of Materials, 26 (2014) 786-801.
[98] M. Mattinen, J. Hämäläinen, F. Gao, P. Jalkanen, K. Mizohata, J. Räisänen, R.L. Puurunen, M. Ritala, M. Leskelä, Nucleation and Conformality of Iridium and Iridium Oxide Thin Films Grown by Atomic Layer Deposition, Langmuir, 32 (2016) 10559-10569.
[99] A.F. Kohan, G. Ceder, D. Morgan, C.G. Van de Walle, First-principles study of native point defects in ZnO, Physical Review B, 61 (2000) 15019-15027.
[100] S.M. Wasim, G. Marín, C. Rincón, G. Sánchez Pérez, Urbach–Martienssen's tail in the absorption spectra of the ordered vacancy compound CuIn3Se5, Journal of Applied Physics, 84 (1998) 5823-5825.
[101] F. Urbach, The Long-Wavelength Edge of Photographic Sensitivity and of the Electronic Absorption of Solids, Physical Review, 92 (1953) 1324-1324.
[102] J.D. Dow, D. Redfield, Toward a Unified Theory of Urbach's Rule and Exponential Absorption Edges, Physical Review B, 5 (1972) 594-610.
[103] G.D. Cody, T. Tiedje, B. Abeles, B. Brooks, Y. Goldstein, Disorder and the Optical-Absorption Edge of Hydrogenated Amorphous Silicon, Physical Review Letters, 47 (1981) 1480-1483.
[104] Correlation between electrical conductivity—optical band gap energy and precursor molarities ultrasonic spray deposition of ZnO thin films, Journal of Semiconductors, 34 (2013) 113001.
[105] M. Yilmaz, Characteristic properties of spin coated ZnO thin films: the effect of Ni doping, Physica Scripta, 89 (2014) 095802.
[106] S. Yang, X. Tian, L. Wang, J. Wei, K. Qi, X. Li, Z. Xu, W. Wang, J. Zhao, X. Bai, E. Wang, In-situ optical transmission electron microscope study of exciton phonon replicas in ZnO nanowires by cathodoluminescence, Applied Physics Letters, 105 (2014) 071901.
[107] T. Singh, T. Lehnen, T. Leuning, D. Sahu, S. Mathur, Thickness dependence of optoelectronic properties in ALD grown ZnO thin films, Applied Surface Science, 289 (2014) 27-32.
[108] W. Shan, W. Walukiewicz, J.W. Ager, III, K.M. Yu, H.B. Yuan, H.P. Xin, G. Cantwell, J.J. Song, Nature of room-temperature photoluminescence in ZnO, Applied Physics Letters, 86 (2005) 191911.
[109] A. Mathur, D. Pal, A. Singh, A. Sengupta, R. Singh, S. Chattopadhyay, Violet Emission of ALD-Grown ZnO Nanostructures on Confined Polymer Films: Defect Origins and Emission Control via Interface Engineering Based on Confinement of the Bottom Polymer Template, Macromolecular Chemistry and Physics, 220 (2019) 1800435.
[110] D.A. Lucca, D.W. Hamby, M.J. Klopfstein, G. Cantwell, Chemomechanical Polishing Effects on the Room Temperature Photoluminescence of Bulk ZnO: Exciton–LO Phonon Interaction, physica status solidi (b), 229 (2002) 845-848.
[111] T. Voss, C. Bekeny, L. Wischmeier, H. Gafsi, S. Börner, W. Schade, A.C. Mofor, A. Bakin, A. Waag, Influence of exciton-phonon coupling on the energy position of the near-band-edge photoluminescence of ZnO nanowires, Applied Physics Letters, 89 (2006) 182107.

[112] A. Singh, A. Mathur, D. Pal, A. Sengupta, R. Singh, S. Chattopadhyay, Near room temperature atomic layer deposition of ZnO thin films on poly (methyl methacrylate) (PMMA) templates: A study of structure, morphology and photoluminescence of ZnO as an effect of template confinement, Vacuum, 161 (2019) 398-403.
[113] D. Pal, A. Mathur, A. Singh, S. Pakhira, R. Singh, S. Chattopadhyay, Binder-Free ZnO Cathode synthesized via ALD by Direct Growth of Hierarchical ZnO Nanostructure on Current Collector for High-Performance Rechargeable Aluminium-Ion Batteries, ChemistrySelect, 3 (2018) 12512-12523.
[114] F. Kayaci, S. Vempati, I. Donmez, N. Biyikli, T. Uyar, Role of zinc interstitials and oxygen vacancies of ZnO in photocatalysis: a bottom-up approach to control defect density, Nanoscale, 6 (2014) 10224-10234.
[115] J.C. Nie, J.Y. Yang, Y. Piao, H. Li, Y. Sun, Q.M. Xue, C.M. Xiong, R.F. Dou, Q.Y. Tu, Quantum confinement effect in ZnO thin films grown by pulsed laser deposition, Applied Physics Letters, 93 (2008) 173104.
[116] S.M. Wasim, C. Rincón, G. Marín, P. Bocaranda, E. Hernández, I. Bonalde, E. Medina, Effect of structural disorder on the Urbach energy in Cu ternaries, Physical Review B, 64 (2001) 195101.
[117] M. Kranjčec, I.P. Studenyak, G.S. Kovacs, I.D. Desnica Franković, V.V. Panko, P.P. Guranich, V.Y. Slivka, Electric conductivity and optical absorption edge of Cu6P(SexS1−x)5I fast-ion conductors in the selenium-rich region, Journal of Physics and Chemistry of Solids, 62 (2001) 665-672.
[118] E.Ş. Tüzemen, S. Eker, H. Kavak, R. Esen, Dependence of film thickness on the structural and optical properties of ZnO thin films, Applied Surface Science, 255 (2009) 6195-6200.
[119] J.F. Chang, H.H. Kuo, I.C. Leu, M.H. Hon, The effects of thickness and operation temperature on ZnO:Al thin film CO gas sensor, Sensors and Actuators B: Chemical, 84 (2002) 258-264.
[120] S. Maniv, W.D. Westwood, E. Colombini, Pressure and angle of incidence effects in reactive planar magnetron sputtered ZnO layers, Journal of Vacuum Science and Technology, 20 (1982) 162-170.
[121] H.P. He, F. Zhuge, Z.Z. Ye, L.P. Zhu, F.Z. Wang, B.H. Zhao, J.Y. Huang, Strain and its effect on optical properties of Al-N codoped ZnO films, Journal of Applied Physics, 99 (2006) 023503.
[122] G. Srinet, R. Kumar, V. Sajal, Structural, optical, vibrational, and magnetic properties of sol-gel derived Ni doped ZnO nanoparticles, Journal of Applied Physics, 114 (2013) 033912.
[123] A.B. Djurišić, X. Chen, Y.H. Leung, A.M.C. Ng, ZnO nanostructures: growth, properties and applications, Journal of Materials Chemistry, 22 (2012) 6526-6535.
[124] R. Elilarassi, G. Chandrasekaran, Synthesis, structural and optical characterization of Ni-doped ZnO nanoparticles, Journal of Materials Science: Materials in Electronics, 22 (2011) 751-756.
[125] M.R.A. Bhuiyan, M.K. Rahman, Synthesis and characterization of Ni doped ZnO nanoparticles, International Journal of Engineering and Manufacturing, 4 (2014) 10-17.
[126] G. Srinet, R. Kumar, V. Sajal, Effects of Ni doping on structural, optical and dielectric properties of ZnO, Ceramics International, 39 (2013) 7557-7561.
[127] G. Vijayaprasath, R. Murugan, T. Mahalingam, G. Ravi, Comparative study of structural and magnetic properties of transition metal (Co, Ni) doped

ZnO nanoparticles, Journal of Materials Science: Materials in Electronics, 26 (2015) 7205-7213.
[128] N. Goswami, A. Sahai, Structural transformation in nickel doped zinc oxide nanostructures, Materials Research Bulletin, 48 (2013) 346-351.
[129] B. Pal, D. Sarkar, P.K. Giri, Structural, optical, and magnetic properties of Ni doped ZnO nanoparticles: Correlation of magnetic moment with defect density, Applied Surface Science, 356 (2015) 804-811.
[130] Z.H. Alhashem, Ni-doped ZnO nanoparticles derived by the sol–gel method: structural, optical, and magnetic characteristics, Arabian Journal of Chemistry, 17 (2024) 105701.
[131] S. Fabbiyola, V. Sailaja, L.J. Kennedy, M. Bououdina, J. Judith Vijaya, Optical and magnetic properties of Ni-doped ZnO nanoparticles, Journal of Alloys and Compounds, 694 (2017) 522-531.
[132] J. Mohapatra, D.K. Mishra, S.K. Kamilla, V.R.R. Medicherla, D.M. Phase, V. Berma, S.K. Singh, Ni-doped ZnO: Studies on structural and magnetic properties, physica status solidi (b), 248 (2011) 1352-1359.
[133] H. Morkoç, Ü. Özgür, Zinc oxide: fundamentals, materials and device technology, John Wiley & Sons, 2008.
[134] S. Guo, Z. Du, S. Dai, Analysis of Raman modes in Mn-doped ZnO nanocrystals, physica status solidi (b), 246 (2009) 2329-2332.
[135] I. Ahmad, M. Aslam, U. Jabeen, M.N. Zafar, M.N.K. Malghani, N. Alwadai, F.H. Alshammari, A.S. Almuslem, Z. Ullah, ZnO and Ni-doped ZnO photocatalysts: Synthesis, characterization and improved visible light driven photocatalytic degradation of methylene blue, Inorganica Chimica Acta, 543 (2022) 121167.
[136] P. Pascariu, I.V. Tudose, M. Suchea, E. Koudoumas, N. Fifere, A. Airinei, Preparation and characterization of Ni, Co doped ZnO nanoparticles for photocatalytic applications, Applied Surface Science, 448 (2018) 481-488.
[137] U.I. Gaya, A.H. Abdullah, Heterogeneous photocatalytic degradation of organic contaminants over titanium dioxide: A review of fundamentals, progress and problems, Journal of Photochemistry and Photobiology C: Photochemistry Reviews, 9 (2008) 1-12.